UNIVERSITÀ
DEGLI STUDI
DI PADOVA

SEDE AMMINISTRATIVA: UNIVERSITÀ DEGLI STUDI DI PADOVA
DIPARTIMENTO DI SCIENZE CHIMICHE

CORSO DI DOTTORATO DI RICERCA IN SCIENCE MOLECOLARI
CURRICOLO: SCIENZE CHIMICHE
CICLO XXIX

Innovative Strategies in Coherent Multidimensional Electronic Spectroscopy

Tesi redatta con il contributo finanziario di ERC-StG QUENTRHEL.

Coordinatore: Ch.mo Prof. Antonino Polimeno

Supervisore: Ch.ma Prof. Elisabetta Collini

Dottorando: Andrea Volpato

Abstract

Recent experimental evidences of long-lived quantum electronic coherences in photosynthetic systems have focused the attention on the possible role of quantum phenomena in enhancing biologically relevant functions and the performance of man-made energy devices. Two-dimensional electronic spectroscopy (2DES) provided several compelling evidences that sparked the discussion, but we are far from achieving clear statements. The technique is little more than a decade old and active research is progressing on setup development and data-analysis procedures. A high-performance setup has been built and advanced calibration procedure and acquisition schemes have been designed, in order to tackle the challenges of current instrumental implementations. Time-frequency decomposition techniques, borrowed from the signal-processing field, have been adapted and applied to the analysis of 2DES coherent oscillating signals. Moreover, a global analysis method based on the variable projection algorithm has been developed for robust and quantitative analysis of coherence signatures. The dynamics of the relevant beating components is resolved with unmatched clarity, supplying a valuable help in their interpretation. An oligomeric porphyrin based model system has been investigated with the developed tools. Vibrational coherences with drastically different behaviors have been analyzed bringing out the role of the disorder in modulating the coherent dynamics.

Abstract (italiano)

La recente osservazione di coerenze quantistiche elettroniche con lunga durata in sistemi fotosintetici ha stimolato l'interesse sul possibile ruolo dei fenomeni quantistici nel migliorare alcune funzioni di rilevanza biologica e nell'aumentare le prestazioni di dispositivi artificiali. Tale interesse è stato supportato da numerose evidenze sperimentali fornite dalla spettroscopia bidimensionale elettronica (2DES) ma la ricerca in questo ambito è ancora lontana dal raggiungere conclusioni definitive. La tecnica 2DES è nata da poco più di un decennio ed è ancora molto attiva la ricerca per lo sviluppo di un apparato strumentale ottimale e di efficienti metodi di elaborazione dati. Nell'ambito del progetto di dottorato, è stato costruito un setup sperimentale ad alte prestazioni accoppiato con avanzate procedure di calibrazione e di acquisizione dati, affrontando le sfide principali delle attuali implementazioni strumentali. Attingendo dal campo ingegneristico dell'elaborazione dei segnali, le tecniche di decomposizione tempo-frequenza sono state applicate allo studio di segnali oscillanti 2DES. Inoltre, un metodo di analisi globale basato sul *variable projection algorithm* è stato sviluppato, allo scopo di avere uno strumento robusto e quantitativo per lo studio dei responsi coerenti. La definizione della dinamica delle componenti oscillanti si è dimostrata un valido strumento per l'interpretazione del dato sperimentale. I metodi sviluppati sono stati utilizzati per l'analisi dei dati sperimentali ottenuti con un sistema

modello costituito da un oligomero con catene laterali porfiriniche. Sono state analizzate coerenze vibrazionali con caratteristiche differenti evidenziando l'influenza del disordine nel modulare la risposta coerente.

Contents

CHAPTER 1

Introduction

The fine details of Nature are peculiar. Matter at its core follows the laws of quantum mechanics. A world in which a particle really can be in several places at once and moves from one place to another by exploring the entire Universe simultaneously. Quantum theory is perhaps a great example of the infinitely esoteric becoming the profoundly useful, indeed it is one of the great pillar supporting our understanding of the natural world. Quantum physics has come a long way since its theoretical beginnings in the early twentieth century. Techniques to manipulate light and matter have become increasingly sophisticated, facilitating fundamental studies of quantum effects in several fields and inspiring new technologies. From quantum computing to quantum photovoltaics, seemingly disparate areas of research are being driven by a shared goal — how to harness and exploit quantum coherence and entanglement [1].

Interaction with the environment and fluctuations are the biggest enemies of quantum dynamics. In order to play a role, quantum phenomena must

survive in time and space for long enough to perform a particular function. Indeed the typical quantum system is isolated and at low temperature, so that coherence properties can easily persist. For example, atomic ions can be confined and cooled near to absolute zero through the interaction with laser fields making decoherence negligible; this has proven to be one of the most successful ways of creating and manipulating quantum entangled stated [2] and one of the first implementation of quantum computing [3].

But how to preserve quantum properties in more common systems that are characterized by strong fluctuations and interaction with the environment? Some answers and design principles can be searched in Nature [4, 5]. Indeed recent experimental evidences in coherent spectroscopy show that quantum coherent effects can play a role in photosynthesis [6]. The biological machinery is the prototype of a chaotic system, it works at room temperature in a noisy and aqueous environment — one should therefore conclude that quantum phenomena are not relevant in typical biological functions because we can foresee that they cannot survive. There is however a growing consensus in thinking that, in the course of evolution, Nature could have learnt to make use of quantum phenomena since they could enable or make more efficient a useful biological function and therefore provide an evolutionary advantage. These quantum phenomena are not merely a byproduct of the underlying quantum nature of chemical bonds but are actually exploited by biological systems to enhance performances and achieve novel functionalities [7].

This discussion has been in the imagery of scientists for a long time. Already in the early 1940s Erwing Shrödinger pioneered this idea in his book *What is life?* forging the basis for the emerging field of Quantum Biology [8]. In the last decade, a great boost to the research of quantum phenomena and biology was given by the developing of sophisticated experimental techniques able to probe quantum processes. Two-dimensional electronic spectroscopy (2DES) has been the most preeminent member in this realm. This technique, which is

little more than a decade old [9], is able to follow in real time the free quantum evolution of a system after photo-excitation on the femtosecond time scale. It is the favourite technique for the investigation of multichromophoric systems because it is able to resolve in two dimensions couplings and relaxations between states of the system and it is able to capture the coherent response [10]. Most importantly, in the last years it gave new insight in the possible role of quantum electronic coherence in the processes of light-harvesting [11, 12, 13] and charge separation [14] in photosynthesis.

The observation of long-lived electronic quantum coherences in multichromophoric biological systems has polarized a lot of attention because the observed time scale should allow for a quantum coherent transport of energy or charge. It is well established from a quantum information perspective that pure quantum-coherent dynamics can provide qualitative performance improvements over classical systems when transport is concerned [15]. It is possible that similar mechanisms act also in light harvesting: the coherent mechanism requires that after absorption of light the excitation is instantaneously shared between interacting chromophores so that it can explore all the possible relaxation pathways simultaneously fulfilling the energy transfer without dissipation [16]. All the investigations on the biological systems have also triggered several research in the field of model artificial systems [17, 18, 19, 20]. There is the necessity of studying simplified systems with respect to the natural counterparts in order to identify recurring motifs and design principles that could sustain the quantum coherent mechanism. Materials for organic photovoltaics have also been investigated finding compelling evidences of wave-like motion of electrons and nuclei driving the photo-induced charge separation [21]. The significance of the experimental evidences are not completely understood, but the resulting design principles could have the potential to lead to the development of new applications at the bio-nano scale [5].

The young 2DES technique has demonstrated to be a remarkably powerful

tool able to lead the way of new research fields. The theoretical background for the interpretation of the optical responses is solid and well developed [10, 9, 22], and in chapter 2 a brief description of the perturbative approach describing the quantum evolution under light-matter interaction during the ultrafast experiments is resumed. Despite the great achievements obtained so far, further improvements of the technique are needed, and this Ph.D. dissertation is pursuing this aim. In order to acquire more reliable data, active research is working on the instrumental side, indeed several implementations were proposed in the last years [23]. In chapter 3 is described the setup I contribute implementing, reporting acquisition routines and innovative calibration procedures. A lot of information are encoded in 2DES spectra and sophisticated data-analysis procedures are needed in order to capture the complete picture with an increased level of clarity and reliability. Following this path, in chapter 4 several data analysis approaches are reported in order to unveil and characterize the coherent dynamics of 2DES data. Lastly in chapter 5 a porphyrin-based model system is investigated. The role of excitonic coupling, solvent, disorder and delocalization of the vibrational modes in modulating the coherent optical response is analyzed, providing stimulating scenarios for future investigations.

Have a nice trip in the tantalizing world of ultrafast optical spectroscopy, see you at the end of the beam.

CHAPTER 2

Theory

The theoretical background behind two-dimensional electronic spectroscopy is well developed. It is based on the semi-classical approximation of light-matter interaction and the time-dependent perturbation theory. Few books have been published in the last two decades [10, 22, 24], which describe in details how to derive the third order optical response from the quantum dynamics and propose an intuitive graphic description of the non-linear spectroscopic signals under the form of double-sided Feynman diagrams. The main objective of this chapter is to give a brief theoretical introduction dealing with the mathematical structure of the third order response function and how it can be exploited to rationalize the experimental signals.

2.1 Light-matter interaction

The interaction between light and matter is one of the most fascinating process in nature. Matter, at its core, is made up of a collection of interacting charged particles which can be perturbed by the oscillating electric field of the

electromagnetic radiation.

Spectroscopy describes the light and the matter as a single system. Fully quantum descriptions therefore start with the definition of an Hamiltonian that can be partitioned into the Hamiltonian of the material $\hat{H}_0$, the Hamiltonian of the light field $\hat{H}_L$, and the light-matter interaction Hamiltonian $\hat{H}_P$:

$$\hat{H} = \hat{H}_0 + \hat{H}_L + \hat{H}_P. \tag{2.1}$$

The solution of the full quantum problem would imply solving the coupled equations of motion of quantum electrodynamics for the light field and quantum dynamics for the molecular system. This is generally a difficult task even for simple systems. A simplified approach, which is able to satisfactorily describe most of the phenomena associated with the absorption of light, is the semi-classical description. The light is treated as a classical electromagnetic field described by Maxwell's equations, while the matter is described by quantum mechanics. An important consequence is that instead of having to simultaneously solve the coupled equations of motion for the light and matter variables, we can break up the light-matter interactions into one-way steps. The method developed primarily by Mukamel and coworkes is followed [10].

In a first step the light perturbs the quantum dynamics of the system such that the light-matter interaction is a perturbation to the material Hamiltonian

$$\hat{H} = \hat{H}_0 + \hat{H}_P. \tag{2.2}$$

At this point, only the material quantum equation of motion must be solved, the changes in the state of the light resulting from the interaction are neglected. The solution of the quantum dynamics of the material allows us to evaluate time-dependent expectation values of physical observables characterizing motion of charged particles in the material, i.e. the polarization of the material $P(t)$. In a second step we can calculate the electromagnetic field radiated as a

consequence of the motion of the charges in the material. The polarization $P(t)$ is used as a source term in the electromagnetic wave equation to calculate the generated field $E_{\text{sig}}(t)$ which represents to the spectroscopic signal. Assuming the perturbing electric field composed of light pulses in the semi-impulsive limit, the electric field generated by the polarization will be $\pi/2$ out-of-phase with the polarization of the sample, meaning

$$E_{\text{sig}}(t) \propto iP(t), \tag{2.3}$$

where only the positive-frequency parts of the field and polarization have been considered. The goal in describing the spectroscopic signal is then finding a feasible way to solve the quantum evolution of the system. The light-matter electric field will be considered as a small perturbation of the system and time-dependent perturbation theory will be employed.

2.2 Quantum evolution

When considering a quantum system that is evolving in time, we need to solve the time dependent Shrödinger equation

$$\frac{d\,|\psi(t)\rangle}{dt} = -\frac{i}{\hbar}\hat{H}(t)\,|\psi(t)\rangle\,, \tag{2.4}$$

where the state of the system is defined by the time-dependent wavefunction $|\psi(t)\rangle$. The matter Hamiltonian $\hat{H}_0$ is typically time-independent, whereas $\hat{H}_P$ is modulated over time by the oscillating electric field.

The trivial evolution of the system under the time-independent part of the Hamiltonian in given by the analytical solution

$$|\psi(t)\rangle = e^{-\frac{i}{\hbar}\hat{H}_0(t-t_0)}\,|\psi(t_0)\rangle\,, \tag{2.5}$$

where t_0 is the initial time and t is the final time. The exponential operator is defined as the time-evolution operator

$$\hat{U}(t,t_0) \equiv e^{-\frac{i}{\hbar}\hat{H}_0(t-t_0)}. \tag{2.6}$$

In order to shorten the derivation of the complete evolution of the system under light-matter interaction it is convenient to operate in the interaction picture. In other words, the trivial evolution of $\hat{H}_0$ can be embedded in a new set of wavefunctions and operators highlighting the evolution due to the difference between $\hat{H}$ and $\hat{H}_0$, i.e. the perturbation $\hat{H}_I$. The interaction picture can be seen as an intermediate case between the Shrödinger picture, where observable are time-independent and the wavefunction evolves in time, and the Heisemberg picture, where the observable evolves in time and the wavefunction is constant. Moreover, in absence of light-matter interaction the interaction picture coincides with the Heisemberg picture. The new interaction set, denoted with a subscript I, is defined as

$$|\psi_I(t)\rangle = \hat{U}^\dagger(t,t_0)\ |\psi(t)\rangle \tag{2.7}$$

$$\hat{O}_I = \hat{U}^\dagger(t,t_0)\ \hat{O}\ \hat{U}(t,t_0), \tag{2.8}$$

where $\hat{O}$ and $\hat{O}_I$ are the operators associated to a generic observable in the Shrödinger picture and in the interaction picture respectively.

The time dependent Shrödinger equation 2.4 can be rewritten in the interaction picture as

$$|\psi_I(t)\rangle = |\psi_I(t_0)\rangle - \frac{i}{\hbar}\int_{t_0}^{t} d\tau_1\ \hat{H}_P^I(\tau_1)\,|\psi_I(\tau_1)\rangle\,, \tag{2.9}$$

where $\hat{H}_P^I(t)$ is the light-matter perturbation Hamiltonian in the interaction

picture at time t. Equation 2.9 can be solved iteratively and the solution is

$$\begin{aligned}|\psi_I(t)\rangle = |\psi_I(t_0)\rangle &- \frac{i}{\hbar}\int_{t_0}^{t} d\tau_1\, \hat{H}_P^I(\tau_1)\,|\psi_I(t_0)\rangle \\ &+ \left(-\frac{i}{\hbar}\right)^2 \int_{t_0}^{t} d\tau_2 \int_{t_0}^{\tau_2} d\tau_1\, \hat{H}_P^I(\tau_2)\hat{H}_P^I(\tau_1)\,|\psi_I(t_0)\rangle \\ &+ \left(-\frac{i}{\hbar}\right)^3 \int_{t_0}^{t} d\tau_3 \int_{t_0}^{\tau_3} d\tau_2 \int_{t_0}^{\tau_2} d\tau_1 \\ &\quad \times \hat{H}_P^I(\tau_3)\hat{H}_P^I(\tau_2)\hat{H}_P^I(\tau_1)\,|\psi_I(t_0)\rangle \\ &+ \dots\,.\end{aligned} \tag{2.10}$$

This expression is also called the perturbative expansion of the wavefunction in presence of a perturbation $\hat{H}_P$. In the case of light-matter interaction, the n^{th}-order term corresponds to the wavefunction of a system that has interacted n times with the external electric field. For example the third-order term can be written as

$$|\psi_I^{(3)}(t)\rangle = \left(-\frac{i}{\hbar}\right)^3 \int_{t_0}^{t} d\tau_3 \int_{t_0}^{\tau_3} d\tau_2 \int_{t_0}^{\tau_2} d\tau_1\, \hat{H}_P^I(\tau_3)\hat{H}_P^I(\tau_2)\hat{H}_P^I(\tau_1)\,|\psi_I(t_0)\rangle\,. \tag{2.11}$$

The term can be transformed back to the usual Shrödinger picture by applying the reverse transformation of equation 2.7, obtaining

$$|\psi^{(3)}(t)\rangle = \hat{U}(t,t_0)\,|\psi_I^{(3)}(t)\rangle\,. \tag{2.12}$$

The results reported in equation 2.11 and 2.12 are the key ingredients to obtain the expression of the third-order polarization of a sample and thus interpret the experimental third-order signals.

2.3 Ensemble average

So far we have discussed the evolution of a pure state of the system described by the wavefunction $|\psi\rangle$. However, in condensed phase systems, we cannot access easily the initial quantum state of the system and we have to deal with statistical ensembles rather than pure states. The total macroscopic system is imagined as a number of replicas of a smaller system and the probability of each replica of being in a pure state $|\psi_k\rangle$ is P_k. In this situation the system can be conveniently represented by the density operator $\hat{\rho}$. The quantum dynamics of a pure state can still be followed using the density operator $\hat{\rho} = |\psi\rangle\langle\psi|$ without adding new physical properties to the description. The definition of the density operator for a statistical ensemble,

$$\hat{\rho} = \sum_k P_k |\psi_k\rangle\langle\psi_k|, \tag{2.13}$$

allows tracking the evolution of a mixture of pure states. Just as the Schrödinger equation 2.4 describes how pure states evolve in time, the Liouville-von Neumann equation

$$\frac{d\hat{\rho}(t)}{dt} = -\frac{i}{\hbar}\left[\hat{H}(t), \hat{\rho}(t)\right] \tag{2.14}$$

describes how the density operator evolves in time. The two equations are equivalent in the sense that one can be derived from the other. The expression for the density operator and the Liouville-von Neumann equation hold also in the interaction picture where $\hat{\rho}_I$ is obtained from equation 2.8.

Following the same mathematical procedure to get equation 2.10 from 2.9, we can obtain the perturbative expansion of the density operator solving

equation 2.14 in an iterative manner

$$\begin{aligned}\hat{\rho}_I(t) = \hat{\rho}_I(t_0) &- \frac{i}{\hbar}\int_{t_0}^{t} d\tau_1 \ \left[\hat{H}_P^I(\tau_1), \hat{\rho}_I(t_0)\right] \\ &+ \left(-\frac{i}{\hbar}\right)^2 \int_{t_0}^{t} d\tau_2 \int_{t_0}^{\tau_2} d\tau_1 \ \left[\hat{H}_P^I(\tau_2), \left[\hat{H}_P^I(\tau_1), \hat{\rho}_I(t_0)\right]\right] \\ &+ \left(-\frac{i}{\hbar}\right)^3 \int_{t_0}^{t} d\tau_3 \int_{t_0}^{\tau_3} d\tau_2 \int_{t_0}^{\tau_2} d\tau_1 \\ &\quad \times \left[\hat{H}_P^I(\tau_3)\left[\hat{H}_P^I(\tau_2)\left[\hat{H}_P^I(\tau_1), \hat{\rho}_I(t_0)\right]\right]\right] \\ &+ \dots .\end{aligned} \tag{2.15}$$

Finally we can highlight the third-order term of the density operator perturbative expansion in the form

$$\begin{aligned}\hat{\rho}_I^{(3)}(t) = &\left(-\frac{i}{\hbar}\right)^3 \int_{t_0}^{t} d\tau_3 \int_{t_0}^{\tau_3} d\tau_2 \int_{t_0}^{\tau_2} d\tau_1 \\ &\times \left[\hat{H}_P^I(\tau_3)\left[\hat{H}_P^I(\tau_2)\left[\hat{H}_P^I(\tau_1), \hat{\rho}_I(t_0)\right]\right]\right].\end{aligned} \tag{2.16}$$

The corresponding term in the Shrödinger picture is obtained applying the inverse transformation of equation 2.8 as

$$\hat{\rho}^{(3)}(t) = \hat{U}(t, t_0)\ \hat{\rho}_I^{(3)}(t)\ \hat{U}^{\dagger}(t, t_0). \tag{2.17}$$

This results allows describing how the quantum evolution of a macroscopic system is affected by three interactions with an external electric field and it will allow, in the following section, to define the response function for a three pulses experiment.

2.4 Response function

Sectroscopists are interested in optical observables and in particular in the polarization. Its oscillation are the source of the electric field that can be

measured as light emitted from the sample. The macroscopic polarization can be expressed as an expansion over the perturbing electric field

$$\begin{aligned} P =& P^{(1)} + P^{(2)} + P^{(3)} + \dots \\ =& \epsilon_0 \left(\chi^{(1)} E + \chi^{(2)} EE + \chi^{(3)} EEE + \dots \right) \end{aligned} \tag{2.18}$$

where $P^{(n)}$ and $\chi^{(n)}$ are the n^{th}-order electric polarization and susceptibilities, ϵ_0 is the dielectric constant of the vacuum and E is the external electric field. In centrosymmetric systems, such as isotropic media, even-order susceptibilities vanish due to the symmetry [25]. Therefore, for most media the lowest order nonlinear susceptibility is the third-order one. The macroscopic polarization can be calculated as the expectation value of the dipole moment operator $\hat{\mu}$ as

$$P(t) = \mathrm{Tr}\left[\mu\rho(t)\right] \equiv \left\langle \hat{\mu}\hat{\rho}(t) \right\rangle, \tag{2.19}$$

where μ and $\rho(t)$ are the matrix representation of the respective operator. As discussed before, the use of the interaction picture eases the formalism. Then we can write the n^{th}-order macroscopic polarization as

$$P^{(n)}(t) = \mathrm{Tr}\left[\mu_I(t)\rho_I^{(n)}(t)\right], \tag{2.20}$$

where $\hat{\mu}_I(t)$ is the dipole moment operator in the interaction picture.

Under the dipole approximation, the light-matter interaction Hamiltonian can be expressed as $\hat{H}_P^I(t) = -\hat{\mu}_I(t)E_T(t)$, where $E_T(t)$ is the total perturbing electric field describing all the incoming laser pulses. For simplicity we disregard the mutual orientation of the field polarization vectors and the transition dipoles, retaining only the their relative amplitudes. We can combine this expression for the perturbation Hamiltonian with equations 2.16 and 2.20 and

get the third-order polarization

$$P^{(3)}(t) = \left(\frac{i}{\hbar}\right)^3 \int_{t_0}^{t} d\tau_3 \int_{t_0}^{\tau_3} d\tau_2 \int_{t_0}^{\tau_2} d\tau_1 \; E_T(\tau_3) E_T(\tau_2) E_T(\tau_1) \\ \times \mathrm{Tr}\left[\mu_I(t)\left[\mu_I(\tau_3),\left[\mu_I(\tau_2),\left[\mu_I(\tau_2),\rho_I(t_0)\right]\right]\right]\right], \tag{2.21}$$

In the remaining steps to obtain the response function, we perform some mathematical acrobatics to write the polarization in terms of delays between light interactions. We assume that $\hat{\rho}_I(t_0) = \hat{\rho}_0$ is the equilibrium density operator which does not evolve in time under the system Hamiltonian $\hat{H}_0$ and thus we can set $t_0 \to -\infty$. Moreover a change of variables is applied as follow

$$\begin{aligned} t_1 &= \tau_2 - \tau_1 \\ t_2 &= \tau_3 - \tau_2 \\ t_3 &= t - \tau_3. \end{aligned} \tag{2.22}$$

The change of variable is represented schematically in figure 2.1. The resulting third-order polarization is

$$P^{(3)}(t) = \left(\frac{i}{\hbar}\right)^3 \int_0^{\infty} dt_3 \int_0^{\infty} dt_2 \int_0^{\infty} dt_1 \\ \times E_T(t-t_3) E_T(t-t_3-t_2) E_T(t-t_3-t_2-t_1) \\ \times \mathrm{Tr}\left[\mu_I(t_1+t_2+t_3)\left[\mu_I(t_1+t_2),\left[\mu_I(t_1),\left[\mu_I(0),\rho_0\right]\right]\right]\right]. \tag{2.23}$$

We can interpret the third-order polarization as a convolution of three electric fields with the third order response function $S^{(3)}(t_1,t_2,t_3)$. Equation 2.23 is rewritten as

$$P^{(3)}(t) = \int_0^{\infty} dt_3 \int_0^{\infty} dt_2 \int_0^{\infty} dt_1 \\ \times E_T(t-t_3) E_T(t-t_3-t_2) E_T(t-t_3-t_2-t_1) S^{(3)}(t_1,t_2,t_3), \tag{2.24}$$

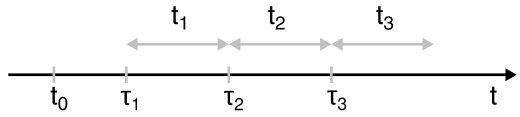

Figure 2.1: Schematic illustration of labels associated with time variables. Variables τ_1, τ_2 and τ_3 represent times at which a light interaction happens, variable t_1, t_2 and t_3 represent time delays between interactions.

with the response function defined as

$$S^{(3)}(t_1,t_2,t_3) = \left(-\frac{i}{\hbar}\right)^3 \mathrm{Tr}\left[\mu_4\left[\mu_3,\left[\mu_2,\left[\mu_1,\rho_0\right]\right]\right]\right], \tag{2.25}$$

where the dipole moments matrix representations have been renamed for simplicity following the order of action on the density matrix

$$\begin{aligned}\mu_1 &= \mu_I(0)\\ \mu_2 &= \mu_I(t_1)\\ \mu_3 &= \mu_I(t_1+t_2)\\ \mu_4 &= \mu_I(t_1+t_2+t_3).\end{aligned} \tag{2.26}$$

The response function is only defined for positive times t_1, t_2 and t_3. Note that μ_4 is not nested in the commutators structure and it has a different role than μ_1, μ_2 and μ_3. The non equilibrium density matrix $\rho^{(3)}$ is generated only by the first three interactions with the electric field, the last dipole moment coming from equation 2.20 represents the emission of an electric field from the sample.

The computation of the convolution of the fields in equation 2.24 can be greatly simplified introducing the semi-impulsive limit. This assumption is valid when the light pulses are short enough that the overlap between couples

of pulses can be neglected. In a multi pulse experiment with three different incoming laser beams the total electric field is expressed as

$$E_T(t) = \sum_{n=1}^{3} E_n(t), \tag{2.27}$$

where E_n is the electric field associated with the n^{th}-laser pulse. Assuming the semi-impulsive limit means using a δ-function time profile for each electric field, maintaining unchanged the central frequency ω_n and the propagation direction $\mathbf{k}_n$ of the pulses, such that

$$\begin{aligned} E_n(t) =& E_n^+(t) + E_n^-(t) \\ =& \mathscr{E}_n \delta(t-\tau_n)\left(e^{i(\omega_n t - \mathbf{k}_n\cdot\mathbf{r})} + e^{-i(\omega_n t - \mathbf{k}_n\cdot\mathbf{r})}\right), \end{aligned} \tag{2.28}$$

where E_n^+ and E_n^- are the positive and negative frequency component of the electric field and $\mathscr{E}_n$ is the scalar amplitude. Note as the real electric field has been expressed as a some of positive and negative frequency exponential functions. Taking care of the change of variable in equation 2.22, the final expression for the polarization in the semi-impulsive limit is recovered

$$\begin{aligned} P^{(3)}(t) = & \int_0^\infty dt_3 \int_0^\infty dt_2 \int_0^\infty dt_1 \\ & \times E_3(t-t_3)E_2(t-t_3-t_2)E_1(t-t_3-t_2-t_1)S^{(3)}(t_1,t_2,t_3). \end{aligned} \tag{2.29}$$

The strict time ordering is assumed. From now on we can directly assign each interaction with the electric field to a specific time-ordered laser pulse. Using the semi-impulsive limit has a second major advantage, in this approximation the response function is also proportional to the third order polarization and the experimental signal, without any complication due to pulse convolution. In the next sections we will discuss the structure of the response function but all the properties will apply directly to the resulting third order signal.

2.5 Feynman diagrams

The mathematical structure of the response function underlies the presence of a series of different contributions to the total emitted signal, each characterized by a specific sequence of light-matter interactions. The effects of such contributions on the density matrix specify different Liouville pathways that the system can follow, i.e. specific time evolution of the density matrix. Since the third order response function contains three dipole interaction factors, it is expected to contain 2^3 terms, corresponding to all the possible choices of acting from the left or from the right of the density operator. The response function can be rewritten making explicit the commutators, giving

$$S^{(3)}(t_1,t_2,t_3) = \left(\frac{i}{\hbar}\right)^3 \sum_{m=1}^{4} \left(R_m - R_m^*\right), \tag{2.30}$$

where

$$\begin{aligned} R_1 &= \mathrm{Tr}\left[\mu_4\mu_1\rho_0\mu_2\mu_3\right] & R_1^* &= \mathrm{Tr}\left[\mu_4\mu_3\mu_2\rho_0\mu_1\right] \\ R_2 &= \mathrm{Tr}\left[\mu_4\mu_2\rho_0\mu_1\mu_3\right] & R_2^* &= \mathrm{Tr}\left[\mu_4\mu_3\mu_1\rho_0\mu_2\right] \\ R_3 &= \mathrm{Tr}\left[\mu_4\mu_3\rho_0\mu_1\mu_2\right] & R_3^* &= \mathrm{Tr}\left[\mu_4\mu_2\mu_1\rho_0\mu_3\right] \\ R_4 &= \mathrm{Tr}\left[\mu_4\mu_3\mu_2\mu_1\rho_0\right] & R_4^* &= \mathrm{Tr}\left[\mu_4\rho_0\mu_1\mu_2\mu_3\right]. \end{aligned} \tag{2.31}$$

By convention the contribution are written with the last interaction emitting from the ket, i.e. μ_4 is on the left side of the expression. While the mathematical notation can get complicated, there is a simple set of rules for graphically representing the various Liouville pathways, obtaining what are called the double-sided Feynman diagrams. This diagrammatic form allows specifying the time ordering using an oriented time axis and it allows explicitly reporting the evolution of the density matrix after each interaction with the electromagnetic field. The diagrams are constructed using the following rules:

(i) vertical lines represent the time evolution of the ket, drawn on the left, and of the bra, drawn on the righ. The time axis is running from the bottom to the top;

(ii) interactions with the electric field are represented by arrows. The last interaction, related to the emission of a signal from the sample is indicated with a wavy arrow and is drawn on the left of the diagram;

(iii) an arrow pointing to the left represents an interaction with a positive electric field $E_n^+(t)$ while an arrow pointing to the right represents an interaction with a negative electric field $E_n^-(t)$;

(iv) an arrow pointing towards (away) the density matrix represents an absorption (emission) interaction;

(v) before the first interaction the density matrix should be in the equilibrium state, usually the ground state, and after the last interaction the system should reach again a pure state, ground or excited.

The design principles at the basis of the double-sided Feynman diagrams and their rigorous derivation can be found in the Mukamel's book [10].

The significance of this schematic representation can be better understood looking at a specific example. A possible realization of Feynman diagram connected to an R_2 interaction scheme is reported in figure 2.2. For simplicity, we are considering three electromagnetic fields with the same frequency. Before time zero the system is in the ground state. After the first interaction with the electromagnetic field acting on the right side of the diagram, the system is in a coherence $|g\rangle\langle e|$ between the ground state $|g\rangle$ and an excited state $|e\rangle$. The second interaction, after the time delay t_1, brings the system into a pure excited state $|e\rangle\langle e|$. At time $t_1 + t_2$, the third interaction generates a coherence $|e\rangle\langle g|$ which induces the emission of the signal at time $t_1 + t_2 + t_3$ that brings back the system in the ground state.

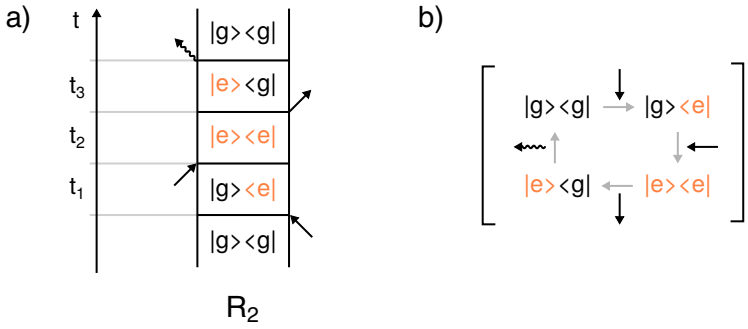

Figure 2.2: Example of realization for a double-sided Feynman diagram connected to a R_2 contribution. (a) Double-sided diagram and (b) schematic representation of the Liouville pathway for a two level system density matrix.

When considering all the possible Feynman diagrams contributing to a specific signal, all the combinations of positive and negative electromagnetic field components must be taken into account. Indeed the final signal is composed by a great number of contributions arising from all the possible Liouville pathways. In figure 2.3 all the generic Feynman diagrams are represented, omitting for now the direction of the arrows representing the electromagnetic fields.

2.6 Feynman diagram selection

Experimentally it is possible not only to separate the third order response from all other orders of interaction, but also specifically select subsets of Feynman diagrams contributing to the experimental signal by controlling the laser central frequencies, the direction of propagation and the pulse sequence of the laser beams.

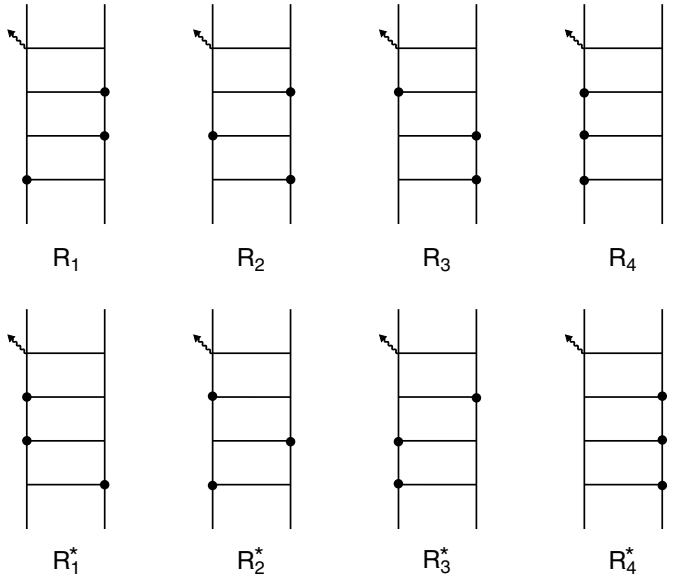

Figure 2.3: Generic double-sided Feynman diagrams summarising all the possible contributions to the response function. Black dots are positioned where an interaction with a electromagnetic field takes place.

When the wave-vectors of the applied laser beams are different, phase-matching conditions can be used to isolate separate contributions to the total signal. This is possible because signals originating from different Liouville pathways are emitted in different directions. The wave-vector of the emitted signal $\mathbf{k}_S$ is given by a combination of the wave-vectors of the incident beams

$$\mathbf{k}_S = \sum_{n=1}^{3} \pm \mathbf{k}_n \tag{2.32}$$

where the sign depends upon the positive or negative electromagnetic field component of the interacting field. The central frequency of the emitted signal

is likewise given by

$$\omega_S = \sum_{n=1}^{3} \pm\omega_n \tag{2.33}$$

where the sign of each frequency is the same of the wave-vectors. In general, the contributions where all the frequency components have the same sign are highly oscillatory and they can be typically neglected, in agreement with the rotating wave approximation (RWA). The dominant signals of interest in 2DES are usually referred to as the 'photon echo', or 'rephasing' signal, generated in the $\mathbf{k}_S^{\mathrm{R}}$ direction and the 'non-rephasing' signal, generated along the $\mathbf{k}_S^{\mathrm{NR}}$ direction, where

$$\begin{aligned} \mathbf{k}_S^{\mathrm{R}} &= -\mathbf{k}_1 + \mathbf{k}_2 + \mathbf{k}_3 \\ \mathbf{k}_S^{\mathrm{NR}} &= +\mathbf{k}_1 - \mathbf{k}_2 + \mathbf{k}_3. \end{aligned} \tag{2.34}$$

The terminology comes from the fact that the phase of the signal evolves at conjugate frequencies during t_1 and t_3 periods in the rephasing signal but not in the non-rephasing one. Thus the former is able to reform into an echo, while phase evolution in the latter can only continue in the same direction. This properties of rephasing and non-rephasing signals resulted in naming the delay times t_1 and t_3 as coherence time and rephasing time, respectively. On the contrary, t_2 is conventionally called population time because in this delay time the system is usually evolving in a pure state (a population) or in a slow frequency coherence. A third relevant signal is the double-quantum coherence signal in which the first two pulses generate a double excitation in the system. The phase-matching conditions for this signal are

$$\mathbf{k}_S^{\mathrm{2Q}} = +\mathbf{k}_1 + \mathbf{k}_2 - \mathbf{k}_3. \tag{2.35}$$

Contributions to the signal in directions that do not match the phase-matching condition vanish due to a randomness in the phase.

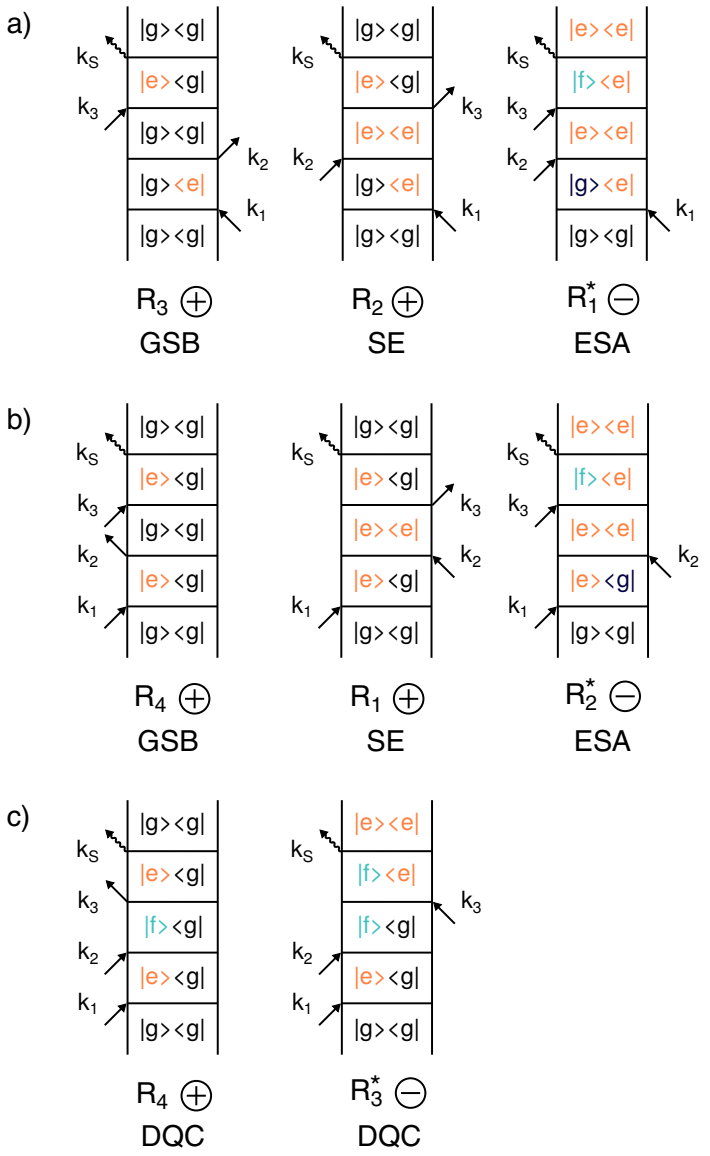

Figure 2.4: Feynman diagrams contributing to (a) rephasing, (b) non-rephasing and (c) double-quantum signals. Orange is used to label single excited states and green is used to label double excited states.

Figure 2.4 reports all the Feynman diagrams contributing to rephasing, non-rephasing and double-quantum signals. Only few of the eight R_m contributions can survive given a specific phase-matching condition. The rephasing signal is composed by R_1^*, R_2 and R_3 Liouville pathways, the non rephasing signal is composed by R_1, R_2^* and R_4 whereas the double-quantum signal is composed by R_3^* and R_4. Usually these diagrams can also be grouped and labeled on a phenomenological basis recalling the terminology used in pump-probe spectroscopy. Four kind of similar contributions are distinguished: (i) ground state bleaching signals (GSB) which refer to depletion of ground state population, for these contributions the system is evolving during the population time in the ground state; (ii) stimulated emission signals (SE) where the system evolves in an excited state during the population time and reaches the ground state at the end of the experiment; (iii) excited state absorption signals (ESA) represented by Feynman diagrams similar to SE signals but where the system evolves as coherence between a double-excited state and a single-excited state during the rephasing time; (iv) double-quantum coherence signals (DCQ) where the system during the population time is evolving in a coherence between the ground state and a double-excited state.

2.7 Fluctuations and lineshape

In an isolated system, once the electromagnetic field generates a coherence between two states, the system will evolve in time oscillating indefinitely at the characteristic frequency corresponding to the energy difference between the two states. Contrary to this, spectroscopy usually deals with macroscopic samples in which a great number of replicas of the investigated system are interacting with an environment. Each system is affected differently by the environment introducing disorder and fluctuations. As a result, in a real macroscopic system the coherence generated by an electromagnetic field interaction

is eventually damped.

The effect of the environment and its impact on 2DES spectra can be treated using the lineshape function formalism [10, 22]. All information connected to the fluctuation of the energy difference between two states is encoded in the lineshape function $g(t)$. Let's consider a two level system with ground and excited states $|g\rangle$ and $|e\rangle$. The interaction between the system and an external bath causes a stochastic force on the molecules giving rise to a time-dependent energy difference between the states, which in turns leads to a fluctuating resonant frequency. The first step is to define the electronic ground-excited state energy gap correlation function as

$$C(t) = \frac{1}{\hbar^2}\mathrm{Tr}\left[Q(t)Q(0)\rho_0\right] \tag{2.36}$$

where $Q(t)$ is the energy gap operator which describes the deviations from the thermally averaged ground-exited state energy gap [26]. The interaction of the system with the bath can be calculated by performing a cumulant expansion on the system-bath interaction; assuming an harmonic model for the bath the expansion to second order is exact [10]. The lineshape function results as an integrated form of the correlation function in equation 2.36 over two different time periods,

$$g(t) = \int_0^t dt'' \int_0^{t''} dt'\, C\left(t'\right). \tag{2.37}$$

The lineshape function is usually modeled using a series of Brownian oscillators which can account for bath fluctuations on multiple timescales and also molecular vibration [27].

Using the lineshape function formalism it is possible to explicit all the possible contributions to the third order signal in the presence of dephasing, and in particular specify the expression for the R_m contributions in equation 2.31. Only R_1, R_2, R_3 and R_4 are possible Liouville pathways in a two level system because all other contributions require the presence of a third higher

energy level. It can be demonstrated that the contributions to the response function of a two level system can be written as

$$\begin{aligned} R_1(t_1,t_2,t_3) &= \mu_{eg}^4 e^{-i\omega_{eg}t_1 - i\omega_{eg}t_3} e^{-g(t_1)-g^*(t_3)-f_+(t_1,t_2,t_3)} \\ R_2(t_1,t_2,t_3) &= \mu_{eg}^4 e^{+i\omega_{eg}t_1 - i\omega_{eg}t_3} e^{-g^*(t_1)-g^*(t_3)+f_+^*(t_1,t_2,t_3)} \\ R_3(t_1,t_2,t_3) &= \mu_{eg}^4 e^{+i\omega_{eg}t_1 - i\omega_{eg}t_3} e^{-g^*(t_1)-g(t_3)+f_-^*(t_1,t_2,t_3)} \\ R_4(t_1,t_2,t_3) &= \mu_{eg}^4 e^{-i\omega_{eg}t_1 - i\omega_{eg}t_3} e^{-g(t_1)-g(t_3)-f_-(t_1,t_2,t_3)} \end{aligned} \tag{2.38}$$

where the two auxiliary functions are defined as

$$\begin{aligned} f_+(t_1,t_2,t_3) &= g^*(t_2) - g^*(t_2+t_3) - g(t_1+t_2) + g(t_1+t_2+t_3) \\ f_-(t_1,t_2,t_3) &= g(t_2) - g(t_2+t_3) - g(t_1+t_2) + g(t_1+t_2+t_3). \end{aligned} \tag{2.39}$$

A careful analysis of equation 2.38 confirms that each contribution can be factorized into three parts: (i) the average transition dipole moment μ_{eg} to the fourth power, which represents the amplitude of the specific nonlinear optical transition; (ii) the second term is a complex exponential function, describing the oscillations of the coherences evolving during the time periods t_1 and t_3. This term can be easily obtained from the corresponding double-sided Feynman diagrams (figure 2.4): coherences $|g\rangle\langle e|$ and $|e\rangle\langle g|$ during the time t_n will introduce a factor $e^{+i\omega_{eg}t_n}$ and $e^{-i\omega_{eg}t_n}$, respectively; (iii) the third term is a complex combination of lineshape functions at different times, accounting for the broadening due to environment fluctuations.

When the investigated system has more than two energy levels, a number of additional Liouville pathways with the corresponding double-sided Feynman diagrams will become possible. Nevertheless the general mathematical structure of the response function does not change and the new contributions will be similar to equation 2.38, but with different resonant frequencies and lineshape functions.

2.8 2D spectra

Two dimensional electronic spectroscopy is a particularly convenient third order nonlinear experiment since it gathers the maximum amount of information from the third order polarization induced in the sample. All the information is encoded in the response $S^{(3)}(t_1, t_2, t_3)$ which is a three dimensional oscillating function difficult to visualize and interpret. In order to obtain the response in a more intuitive form, usually the time domains t_1 and t_3 are Fourier transformed, obtaining the signal

$$S^{(3)}(\omega_1, t_2, \omega_3) = \int_{-\infty}^{+\infty} \int_{-\infty}^{+\infty} dt_1 dt_2 \; S^{(3)}(t_1, t_2, t_3) e^{-i\omega_1 t_1} e^{-i\omega_3 t_3} \tag{2.40}$$

which can be visualized as two dimensional frequency-frequency maps evolving along the population time. From this representation comes also the term 'two dimensional' electronic spectroscopy. The axis ω_1 contains information about the first excited coherence and can be considered as a label of the initial excitation frequency, whereas the axis ω_3 contains information about the second optical coherence which probes the state of the sample following the dynamics during the t_2 period. Therefore, the 2D spectrum acts as a correlation map, wherein ω_1 and ω_3 can be interpreted as the excitation axis and the emission or detection axis, respectively.

The fluctuations affects the shape of the 2D spectra inducing broadening of the features. One of the great advantages of the 2DES technique is the ability to resolve homogeneous and inhomogeneous broadening: at early population times, in a rephasing 2D spectrum, the broadening along the diagonal is a measure of the inhomogeneous broadening, whereas the broadening along the anti-diagonal is a measure of the homogeneous broadening. Moreover, 2DES allows studying the dynamics of fluctuation recording the lineshape of the signals as a function of the population time. At early times, the system is excited at a certain frequency during t_1 and it is emitting the signal immediately at the

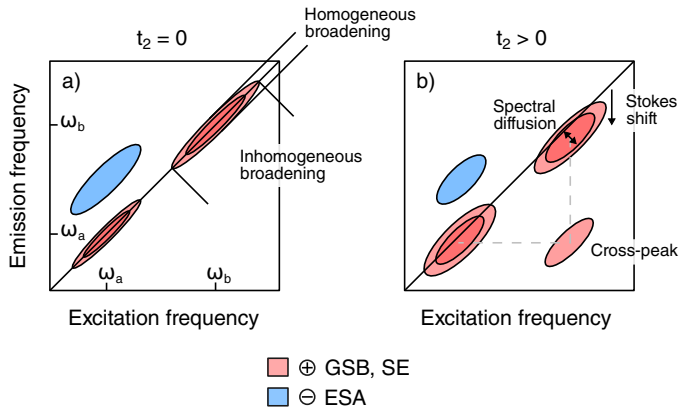

Figure 2.5: Schematic representation of a real rephasing 2D spectrum for a multilevel system. (a) At early population times, the GSB and SE features of two levels with frequency ω_a and ω_b appear as signals elongated on the diagonal. (b) As the population time evolves, the spectral diffusion produces a broadening of the features, the Stokes shift produces a red shift of the signals along the emission axis end a cross-peak may appear in the lower part of the map as a consequence of the relaxation from the high energy level to the low energy one. Negative ESA signals can also appear, typically far from the diagonal.

same frequency during t_3, giving rise to a signal compressed on the diagonal. If enough population time is waited, the system can evolve under the effect of the fluctuations of the external bath and the feature on the 2D spectrum will become gradually rounder. Indeed, the loss of correlation can be followed by looking at the broadening of the peak in the anti-diagonal direction. A simple sketch of a rephasing map for a multilevel system is shown in figure 2.5.

Relaxation during the population time appears in the 2D spectra as shifting of the signals at lower emission frequency. Ultrafast Stokes shift due to solvent or structural reorganization of the system appears as a drift of the features

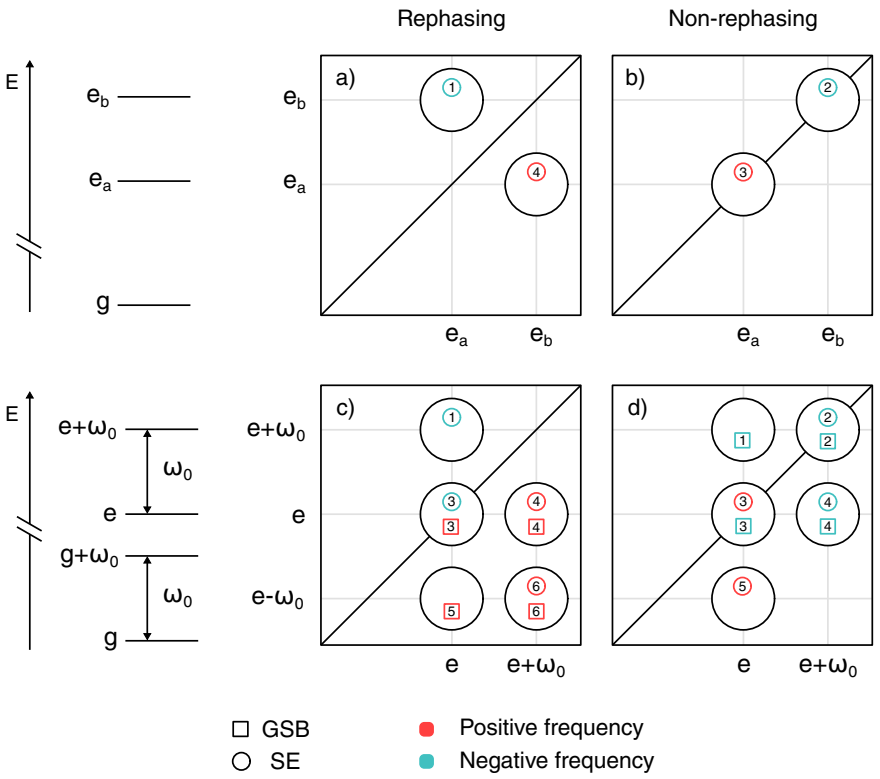

Figure 2.6: Diagrammatic scheme representing the amplitude pattern for (top) an electronic coherence and (bottom) a vibrational coherence. The energy levels are labeled with g and e for ground and electronic states respectively, whereas the vibrational quantum is ω_0. Each oscillatory pattern is marked with a geometric figure, GSB with squares and SE with circles; the numbers serve as references for figure 2.7 and figure 2.8. Positive and negative frequency contributions are marked with red and green color respectively. Panels (a,c) represent the expected pattern for rephasing signals, whereas panels (b,d) refer to non-rephasing signals.

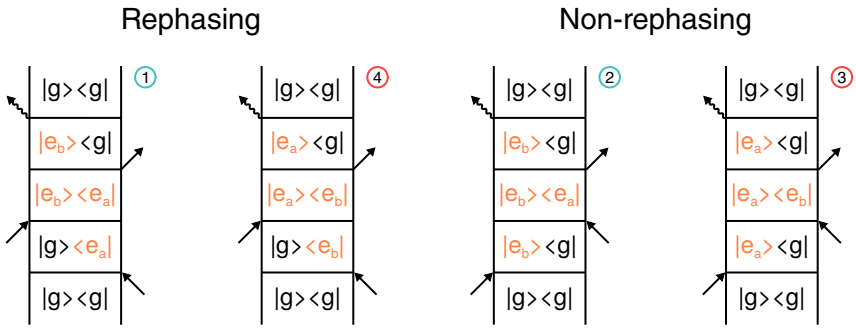

Figure 2.7: Feynman diagrams for electronic coherences. All of them are SE contributions. The numbers indicate specific coordinates of the maps in figure 2.6 panels (a,b).

below the diagonal. Relaxation between energy levels, or also energy transfer between different molecules, produces rising cross peaks below the diagonal with simultaneous decay of the diagonal signals associated with the initial states. Excitation and emission coordinates of the cross peaks tell directly the energy of the involved states.

Finally in rephasing and non rephasing signals, several oscillating contributions are expected along the population time. These are signatures of coherences evolving along t_2 as a result of simultaneous excitation of a superposition of two states by the first two field interactions. The maximum frequency of the observed coherences are limited by laser bandwidth which can be of the order of thousands of cm^{-1}. Depending on the character of the involved states, vibrational or electronic coherences can be distinguished. The amplitude patterns of the oscillations on the 2D spectra are different in the two cases and they can be used to identify the nature of the observed coherence [28, 29, 30, 31]. Figure 2.6 shows the different pattern for rephasing and non-rephasing signals.

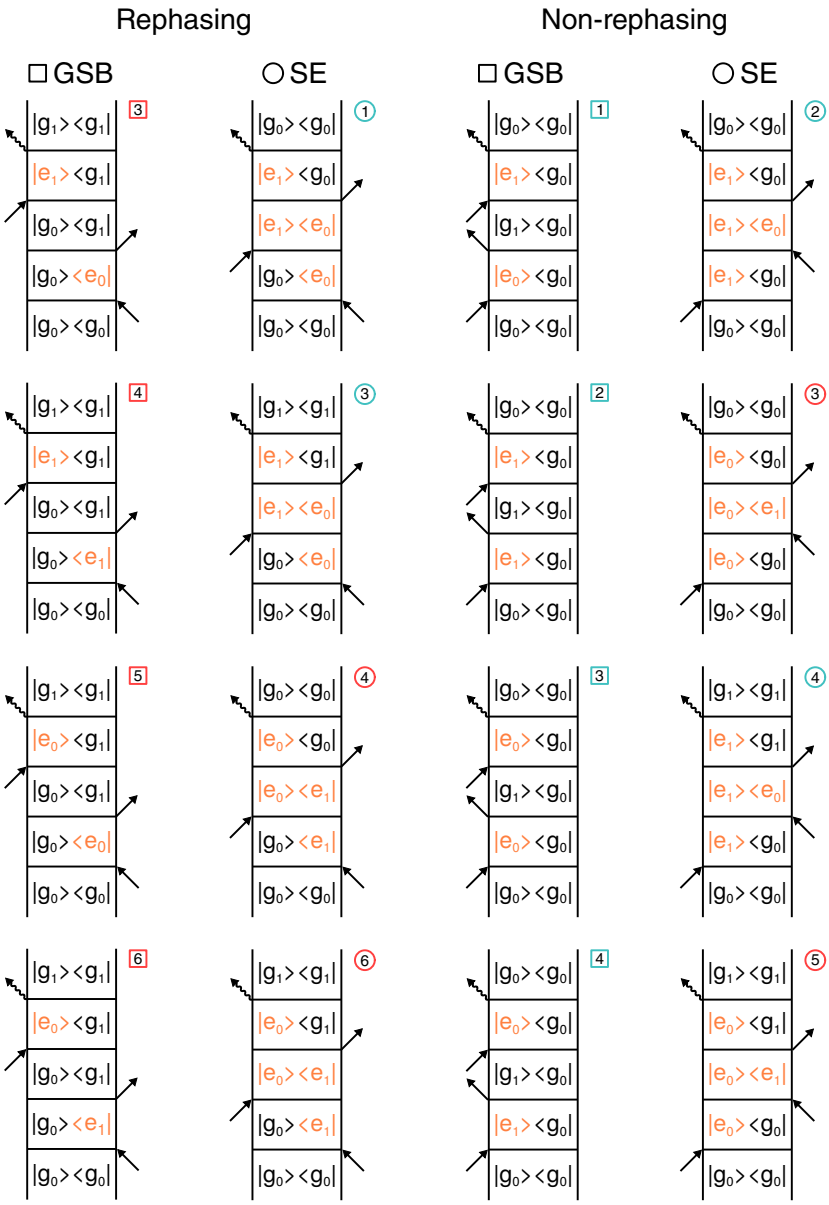

Figure 2.8: Feynman diagrams for vibrational coherences. The numbers indicate specific coordinates of the maps in figure 2.6 panels (c,d).

In rephasing signals, electronic coherences appear as oscillations of the response at the two cross-peaks with conjugate frequencies. Homologous contribution are located on the diagonal in non-rephasing spectra. All the electronic coherence contributions are stimulated emission pathways. Under the assumption that vibrational manifolds on ground and excited states are similar, it is possible to foresee a number of additional oscillating pathways for vibrational coherences which leads to strong differences with respect to electronic ones. Both rephasing and non-rephasing spectra show new vibrational oscillating pathways as illustrated in figure 2.6. The vibrational coherence magnitude distribution is often referred as 'chair pattern' because of the resemblance of the rephasing signal distribution with the profile of a chair. Despite the significant differences of electronic and vibrational coherence signatures, due to the broadening of the observed features and laser spectrum distortions it is not always easy to make a specific assignment [32]. Furthermore, when electronic coupling between chromophores in the system generates mixed states the distinction becomes less rigorous and a range of intermediate cases is possible [33, 34, 35].

CHAPTER 3

Setup

Two dimensional electronic spectroscopy is a third order nonlinear technique which is successfully spreading in the latest years thanks to its capability of unraveling electronic and vibrational couplings and ultrafast dynamics of the systems under investigation. 2DES is based on the interaction of three ultrafast laser pulses with an optical sample and the experiment consists in probing the resulting third order optical polarization as a function of the time delays between the three different interactions. Unlike other third order techniques, the possibility in 2DES to scan independently the three time delays allows disentangling overlapping signals and unravelling correlations between different transitions. This technique has the powerful capability to follow the temporal evolution of both coherent and non-coherent processes. The price to pay for this enhanced quantity of information is the complexity of the optical setup that raises several challenges: isolating and detecting the third order signal despite its weak intensity, gaining phase stability, accurately calibrating femtosecond-time-scale delays, phasing the absorptive

spectra. In this chapter the fully non collinear 2DES setup implemented in our lab will be discussed and the solutions adopted to tackle all the technical challenges will be described.

3.1 Adding a dimension

From many points of view, 2DES could be interpreted as an extension of pump-probe spectroscopy. Both techniques probe the third order polarization of a sample after three interactions with external electric fields and thus they offer similar information. In a frequency-resolved pump-probe experiment the investigated system is excited with a pump pulse (first two interactions), and after a waiting-time the system is probed with a second attenuated pulse (third interaction). The evolution of the recorded spectrum as a function of the waiting-time embeds the system dynamics, i.e. transient peaks at different resonant energies are recorded. Usually several signals can overlap and the dynamical information must be untangled with global analysis procedures. It is also common to use a white light continuum probe in order to get spectral information over a broad range of detected frequency, which can help resolve the dynamics by looking at distant and related peaks along the detection frequency dimension.

Two-dimensional spectroscopy solves much of the problems connected with overlapping signals because it is able to resolve also the excitation frequency. It explicitly provides the information related to multiple peaks contributing at the same detection frequency, thus giving an immediate picture of relaxation pathways and couplings. But how can we add this second dimension to the experiment? One could imagine to resolve the excitation axis by repeating a pump-probe experiment scanning a single narrowband pump pulse in frequency. The use of a narrow spectrum imply to cut down the time resolution of the experiment because, according to the time-bandwidth product, a pulse

with a narrow spectrum is characterized by a long time-duration. This would induce a trade-off between the excitation axis resolution and the time resolution necessary to study ultrafast relaxation dynamics. The problem is completely bypassed acquiring the excitation axis in the time domain by scanning the delay t_1 between a pair of broadband pulses. The generated signal oscillates as a function of the delay time t_1 allowing the excitation frequency axis to be recovered by Fourier transform. In this case, the wider the pulse spectrum and the larger the excitation frequency window probed by the experiment. The result has both high temporal and spectral resolution, limited only by the signal-to-noise ratio.

In its most common form, 2DES spectroscopy employs three identical pulses, effectively splitting the pump pulse of a pump-probe experiment into two time-delayed interactions with the sample. The signal is then recorded as a function of all three time delays, the definition of the delays is schematically reported in figure 3.1 panel (a). The final 2DES spectrum is obtained after Fourier transforming along t_1 and t_3. As we will se in chapter 4, it is also possible to Fourier transform the signal with respect to t_2, producing a 3D frequency solid which is often called 3DES spectrum [36]. Other collection modalities exist. For example, it is possible to tune the spectra of each pulse conducting selective experiments which probes specific subsets of the possible Liouville pathways. Specifically, when the two pump pulses have a different spectrum the experiment is called two-color 2DES [37]. As in pump-probe spectroscopy, the probe pulse can be replaced with a white light super-continuum in order to expand the emission frequency window [38]. Moreover it is possible to detect the 2DES response using the fluorescence signal in what is called fluorescence-detected 2D electronic spectroscopy (FD2D). In this case, at the end of the pulse sequence, a fourth pulse is necessary to let the system reach an excited state population which is able to spontaneously emit florescence [39].

The main technical challenge in implementing a multidimensional Fourier

transform experiment is creating and delivering the appropriate pulse sequence with variable, yet phase-stable time delays between them [23]. With phase stability we refer to the fluctuation of the phase of a laser pulse with respect to the others. This is as a consequence of experimental factors which must be carefully controlled: for example spatial fluctuations of the optics must be reduced to an amplitude much smaller than the wavelength of the electromagnetic radiation. Generally, the shorter the wavelength becomes, the more phase stability is required from the instrumental apparatus. Nevertheless, phase stability and precise timing are required only over the time delays that will be Fourier transformed: typically, in rephasing and non-rephasing signals, the t_1 and t_3 delay. During these time delays the signal is oscillating at an optical frequency because the system is in a coherence between the ground and an electronically excited state.

3.2 Setup geometry

Depending on the experimental geometry of the incident pulses, the phase-matching condition determines the direction of the signal emission. A range of geometries has been employed for 2DES measurements, including (i) fully non-collinear geometry in which every pulse has a different wave-vector, (ii) partially non-collinear pump-probe geometry in which the first two pulses are collinear and are followed by a probe pulse at a small angle and (iii) fully collinear geometry in which every pulse has the same direction. All implementations have their advantages and disadvantages [40].

The fully non-collinear BOXCARS setup is probably the most frequently employed. In this implementation the signal is generated in a background free direction, and thus a pivotal advantage is an high signal-to-noise ratio. A fourth pulse called local oscillator (LO) is mixed with the signal in order to record the phase information recording the interference pattern of the two pulses [41, 42].

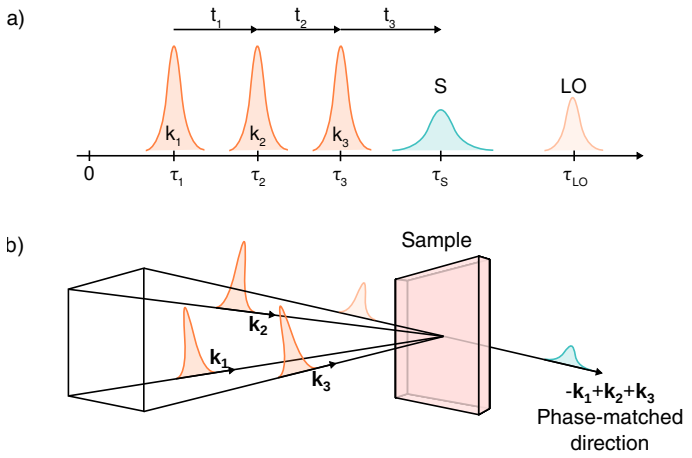

Figure 3.1: Pulse sequence used to obtain a 2DES spectrum. (a) Representation of the arrival time of each pulse with respect to an experimental time zero and definition of the time delay t_1, t_2 and t_3. (b) BOXCARS phase-matching geometry.

The main disadvantages of this implementation are the complexity of the setup, which must include in the design a passive phase stabilizer, and the fact that the final signal is accompanied by an arbitrary constant phase that must be determined. The pump-probe projection theorem is usually invoked for the phasing of the signal. See section 3.8 for more details.

Setups based on the pump-probe geometry are intrinsically phase stable. In these schemes a pulse shaper is usually used to generate collinear pump pulses, with a known and adjustable relative phase. The probe beam can be either an attenuated replica of the pump or a spectrally broader white light continuum [38]. The advantage of this scheme is that the signal is generated collinearly with the probe beam so that it is heterodyned with the probe itself and, therefore, automatically phased. Some disadvantages are: a strong background contribution, lowering its sensitivity; no easy independent manipula-

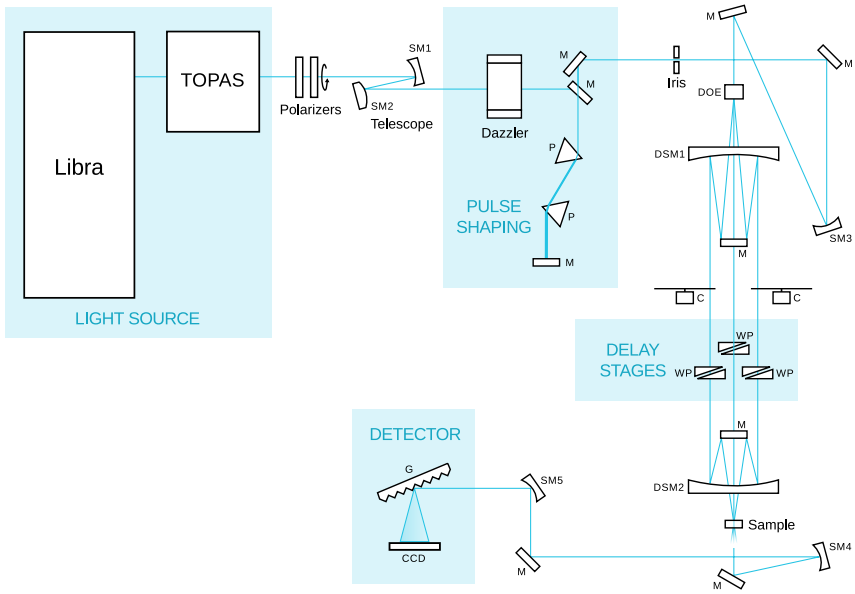

Figure 3.2: Schematic representation of the BOXCAR geometry setup for 2DES implemented in our lab. Abbreviations: (M) mirror, (SM) spherical mirror, (P) prism, (DOE) diffractive optical element, (DSM) donut spherical mirror, (C) optical chopper, (WP) wedge pair, (G) grating, (CCD) charge-coupled device.

tion of beam polarization; contributions of collinearly propagating nonlinear signals; the lack of access to rephasing and non-rephasing signals separately in a straightforward manner.

The implemented experimental setup is schematically illustrated in figure 3.2. The scheme is inspired to the BOXCARS geometry setup proposed by Hauer *et al.* [43]. The choice of this particular implementation is due to a number of advantages: (i) it uses one diffractive optics element to generate all the beam replicas used in the pulse sequence, allowing for an high passive phase stability; (ii) it is based on a background free heterodyne detection which

has high signal-to-noise ratio; (iii) the setup is quite compact and easy to align; (iv) all the beam delays are independently controlled allowing for a great flexibility in experiment design, as a consequence rephasing, non-rephasing and double quantum signal contributions can be easily acquired; (v) pulse compression is easily verified at sample position and it can be accurately optimized. Some known disadvantages are: (i) the time window of the experiment is quite limited, for implementations present in literature it is ~1 ps; (ii) it requires a signal phasing procedure; (iii) the independently controlled beams require an accurate and collectively tuned calibration of the delays. All considered, the advantages have been evaluated more relevant than the disadvantages. This is particularly true in the context of studying coherent dynamics, typically exhausted in the first picosecond after excitation, hence the maximum time window of the experiment in not so critical.

In figure 3.2, a Coherent® Libra laser system generates a continuous pulse train centered at 800 nm with a repetition rate of 3 KHz. The outcoming pulses have a bandwidth of about 12 nm and time duration of about 100 fs. The central wavelength of the laser pulses is converted in the visible range using a commercial NOPA (Light Conversion® TOPAS White). The outcoming pulse spectrum is tunable in the visible range, and the maximum achievable bandwidth depends on the selected central wavelength, i.e. the efficiency of the system is not constant in the full visible spectrum. The best performance is obtained in the spectral range of 650-700 nm, where ~2500 cm^{-1} of bandwidth is achieved.

Before entering the optical setup, the pulses from the NOPA pass through a stage of pulse shaping and prisms compression to maximize the time resolution and guarantee full control over the phase of the different frequency components in the broadband pulse. A detailed description of the pulse shaping stage is reported in section 3.3.

Four identical beams in BOXCARS geometry are obtained focusing the

incoming beam into a 2D diffractive optic element (DOE) with the spherical mirror SM3, having a focal length of 500 mm. The outgoing divergent beams are collimated and parallelized by a donut-shaped spherical mirror (DSM1), with the same focal length of the focusing mirror SM3.

Three 4° CaF_2 wedge pairs (WP), mounted on linear stages (Aerotech® Ant 95), introduce variable delays in the excitation pulses. The position of these devices has to be accurately controlled to guarantee reproducibility and precision of time delay between pulses. Instead of fused silica, the choice of CaF_2 is more suitable since it induces less phase distortions in broadband pulses because of the higher Abbe number [44]. After several tests, the 4° wedges resulted able to guarantee an accurate control of time delay in a range of more than 2 ps. The fourth pulse is used as a local oscillator (LO) and its intensity is conveniently attenuated with a graduated neutral filter in order to maximize the heterodyne signal. The four beams are focused onto the sample by DSM2 with a focal length of 200 mm. The third order signal propagates in the LO direction and their interference is delivered to the spectrograph (Andor® Shamrock 303i) equipped with a CCD (charge-coupled Device) camera (Andor® Newton). Figure 3.1 panel (b) shows a scheme of the approaching geometry of the pulses to the sample.

During the 2DES experiment, the CCD camera collects other spurious contributions besides the signals. A suitable acquisition method and a post-processing procedure are thus necessary to remove the unwanted contributions and gain a high signal-to-noise ratio. The acquisition methodology is based on the double modulation lock-in method proposed by Augulis *et al.* [45] and will be discussed in detail in section 3.7.

3.3 Compression and pulse shaping

The time resolution of a 2DES experiment is directly related to the pulse duration: the shorter the pulse, the better the resolution [23]. The pulse duration is determined mainly by two factors: the bandwidth and shape of the laser spectrum and the phases of its spectral components. The shortest pulse for a given laser spectrum is called transform-limited (TL) pulse, and it can be obtained tuning the phase of the radiation as a function of the frequency $\phi(\omega)$, assuring that at the sample position all the spectral components of the laser spectrum are in phase, i.e. the function $\phi(\omega)$ is a linear function. In the implemented setup the pulse shaping stage consists of an acousto-optic programmable dispersive filter (AOPDF, Fastlite® Dazzler) and a prism compressor. The deviations of the phase as function of the frequency have to be compensated to achieve a TL pulse at the sample position. Essentially the AOPDF corrects the phase distortions induced by the pulses traversing transmissive optics in the setup.

This procedure can be easily explained considering the frequency dependence of the phase of the electric field as follows

$$E(t,\omega) = S(\omega) \cdot e^{i\left(\omega_0 t + \phi(\omega)\right)}, \tag{3.1}$$

where $\omega = 2\pi\nu$ is the angular frequency, $S(\omega)$ is the envelope of the electric field, ω_0 is the central frequency. Usually $\phi(\omega)$ is conveniently expanded using

a Taylor series defined around the value ω_0 and truncated at the forth order

$$\begin{aligned}\phi(\omega) &= \phi(\omega_0) + \left(\frac{d\phi}{d\omega}\right)_{\omega_0} (\omega-\omega_0) + \\ &+ \frac{1}{2}\left(\frac{d^2\phi}{d\omega^2}\right)_{\omega_0} (\omega-\omega_0)^2 + \\ &+ \frac{1}{6}\left(\frac{d^3\phi}{d\omega^3}\right)_{\omega_0} (\omega-\omega_0)^3 + \\ &+ \frac{1}{24}\left(\frac{d^4\phi}{d\omega^4}\right)_{\omega_0} (\omega-\omega_0)^4. \end{aligned} \tag{3.2}$$

The terms at different orders describe different properties of the temporal profile of the pulse. The linear term is related to the arrival time of the pulse, while the second order describes the linear chirp. Higher even (odd) terms correspond to phase distortions with point (axial) symmetry with respect to ω_0 [46] .

In a TL pulse the phase shows only a linear frequency dependence, and thus terms with higher order should not be present. The TL pulse can be recovered by estimating the coefficients of the terms of the series and consequently cancelling them *via* the AOPDF. In principle, the AOPDF can impose the chosen phase at each frequency component with a resolution of about 1.5 nm for a broad spectrum. However, the device is based on the acousto-optic interaction within a crystal, which generates itself a huge positive chirp. Thus, the AOPDF is capable to compensate the self-induced chirp only at the cost of managing a narrower bandwidth. This inconvenience is mitigated introducing a second chirp-compensation stage. The performances of the AOPDF are helped by a standard prism compressor [47, 48] that consists of a couple of prisms. The prism compressor stage relieves the AOPDF from the self compensation leaving the latter able to express its full potential.

The measurement of the pulse profile is performed with the frequency-resolved optical gating technique (FROG) at the sample position [49, 50] that

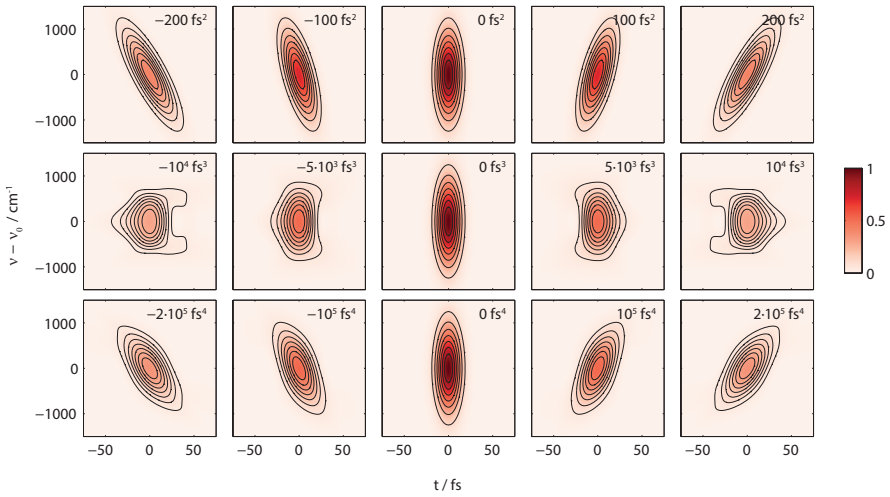

Figure 3.3: Simulated FROG signals presenting distortions of the phase at different orders. The time in the horizontal axis is to the delay of the third pulse with respect to the the first two pulses. Top, middle and bottom rows show distortions at the second, third and fourth order, respectively.

reveals the frequency-resolved auto-correlation of the pulse. In our setup, we can take advantage of the BOXCARS geometry to perform FROG by replacing the sample with a non-zero third order material, typically a solvent. The use of the same cuvette in the same position for sample and solvent guarantees identical operating conditions in FROG and 2DES measurements, keeping the same pulse properties in the two experiments. The FROG experiment consists in acquiring the transient-grating non-resonant signal generated with the same phase-matching of the 2DES signal. Two of the pulses are kept fixed at time zero and the third pulse is scanned from negative to positive delays. For a transform limited pulse the maximum signal appears when the three pulses are superimposed in time; when the third pulse is moved from the superposition

condition the signal decays uniformly for all the spectral components. Different kind of distortions can be identified by changing one at a time the phase orders in equation 3.2 and monitoring the FROG pattern. The effects on the shape of the FROG measurement induced by the alteration the coefficients of the second, third and forth order terms of the Taylor series of equation 3.2 are illustrated in Figure 3.3.

The procedure to recover a TL pulse consists in iteratively modifying the coefficients of the different terms of equation 3.2 *via* the AOPDF and checking the FROG result until the best conditions are found. Since the effects induced by tuning the coefficients of the different terms is known, as in figure 3.3, an easy and quick retrieval of their optimal values for a TL pulse is possible.

3.4 Phase-matching conservation

Phase matching conditions are crucial for a non-collinear 2DES experiment. The beams need to be carefully aligned in order to keep correct relative angles between the pulses as they interact with the sample. Propagation of pulses on the vertices of the square (BOXCARS) is the ideal condition to generate the third order signal along the LO direction. Deviations of even small angles from the ideal square geometry can produce artifacts in the collected signal [22]. The sturdy geometry proposed above helps an easy alignment of the setup inducing naturally the square configuration.

A critical factor for phase matching conservation is the alignment of the optical WP used to time delaying the pulses because, even with best grade wedges, small deviations of the beams are detected. The procedure adopted to correct this deviation consists in checking the pulses geometry with a CCD camera at sample position. Firstly, the setup is perfectly aligned without wedges and the four beams position is recorded on camera. As shown in figure 3.4 panel (a), the pulses are well arranged on the vertices of a square. The WPs

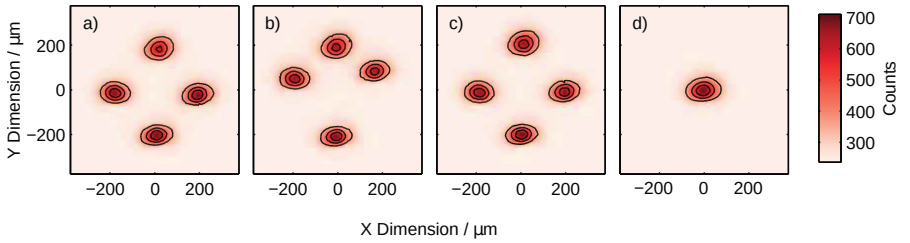

Figure 3.4: Contour plots of the four beam profiles recorded by the CCD camera at the sample position. (a) The setup is carefully aligned to achieve a perfect square arrangement of the four pulses: no delaying material is present. (b) WPs are placed on the beam paths of the exciting pulses. (c) The ideal square arrangement is recovered after slight rotation of the wedges. (d) At the sample position the four beams are perfectly spatially overlapped.

are subsequently placed on the beam paths and the deviations from the ideal position are compensated by slightly rotating the wedges around both the beam propagation axes and the normal to the laser table. The square geometry of the four beams is eventually restored, see Figure 3.4 panels (b,c).

Finally, the optical wedges are moved by the translation stage and the conservation of the beams position is verified *via* the CCD camera to ensure that the phase-matching condition will be preserved during the whole 2DES experiment.

3.5 Wedges calibration

A crucial step in setting a 2DES experiment is the calibration of translation stages that regulate the wedges positions and the amount of CaF_2 that the pulse passes through. In a non-collinear 2DES measurement the phase of the signal is a linear combination of the phase of all pulses. When the time delay is

controlled by a translation stage, its accuracy should be adequate to conserve the phase difference between pulses. This task is far from being trivial because the scanned time range is grater than 2 ps and even an error of a fraction of the wave cycle of the radiation induces a relevant phase shift. For example, at 600 nm an error of 0.5 fs induces a $\pi/2$ phase shift.

The methodology for time delay calibration here proposed is inspired by the procedure described in ref. [29] for the determination of the sub-cycle time from the local oscillator. The definition of the time variables has been already reported in figure 3.1 panel (a). A linear relation is used to convert the position x_i (in mm) of the i^{th} linear stage, and thus the position of the optical wedge, into a time delay τ_i (in fs) of the i^{th} pulse:

$$\tau_i(x_i) = c_i\,(x_i - z_i)\,, \tag{3.3}$$

where c_i is the linear calibration coefficient (in fs/mm) that has to be determined. The choice of a linear relationship means that the effect of the CaF_2 medium on the pulse phase can be reasonably truncated at the first order. The delay τ_i is calculated from the time zero of the experiment, where the linear stages are in the positions z_i that guarantee equal time delay τ_{LO} of all the exciting pulses from the local oscillator. The LO is taken as a reference because is the only pulse whose timing τ_{LO} is fixed since it is not controlled by an optical WP. The time delay calibration consists in three main tasks: (i) determining the time zero of the experiment and therefore the positions z_i of the three linear stages that satisfies the equation: $\tau_i(z_i) = 0$ fs; (ii) finding the linear coefficients c_i to convert a displacement of the stage in a time delay from the zero of the experiment; (iii) finding the precise value of τ_{LO} .

Within the proposed setup, the calibration procedure is based on recording the spectral interference (SI) produced by each exciting pulse and the LO. To this purpose, a 25 μm pinhole is placed where the four beams are focused at the sample position and the SI is recorded by the spectrometer. The Fourier

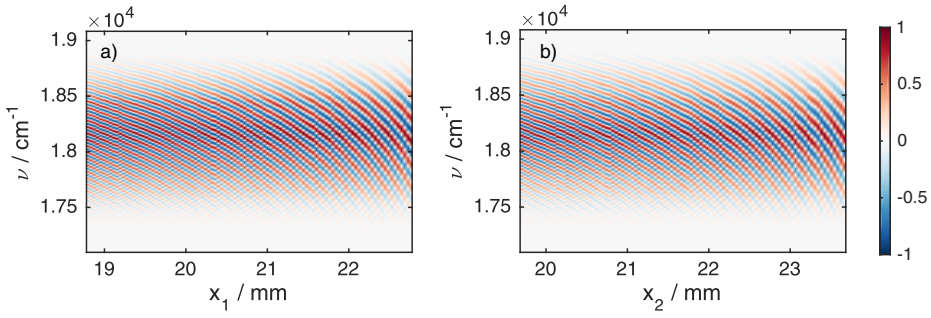

Figure 3.5: Example of spectral interference patterns used in the dealy calibration procedure: (a) matrix $\mathbf{F}^{(1)}$; (b) matrix $\mathbf{F}^{(2)}$.

transform of the SI is the simplest method to correlate the position of the stages with the time delay between LO and the selected pulse: when a spectral interference between two pulses is Fourier transformed, a peak in the time domain is obtained, centered at the delay time between the interfering pulses. As the delay increases, the number of fringes in the spectral interference increases, shifting the peak in the time domain. However, the evaluation of the center of the Fourier transform peaks lacks the precision needed to ensure phase-locking during the experiments. A more sophisticated time delay calibration routine is thus necessary.

First, a set of positions of the three stages that roughly induce the same delay with LO is estimated. This evaluation can be performed by adjusting the stages in such a way as to produce similar interference patterns. We subsequently scan each stage x_i in a short range, about 20% of the length of the wedges, and obtain three matrices $\mathbf{F}^{(i)}$ of spectral interferograms recorded for different positions x_i and resolved in frequency by the spectrograph. See figure 3.5 for two examples of interference patterns. Every column of the matrix $\mathbf{F}^{(i)}$ represents an interference spectrum which evolves as the delay between the interfering beams changes due to the motion of the linear stage. At this point

we have three matrices $\mathbf{F}^{(1)}$, $\mathbf{F}^{(2)}$ and $\mathbf{F}^{(3)}$ that contain all the information about the evolution of the pulse delays with respect to the fixed LO as the stages move.

Evaluation of zero positions

One of the exciting beams is selected as the reference pulse, for example we can choose the first beam with $i = 1$. One at the time, the remaining two beams are compared with the reference. Here the procedure is illustrated for beam with $i = 2$, but the same will be applied for beam with $i = 3$. The main objective of this procedure is to produce, from the interference patterns $\mathbf{F}^{(1)}$ and $\mathbf{F}^{(2)}$, a delay correlation plot called $\mathbf{H}^{(2)}$. This plot allows correlating the position of the two stages, generating a clear signature when the two pulses are synchronous. The elements of the matrix $\mathbf{H}^{(2)}$ are defined as

$$H^{(2)}_{kl} = \text{envelope}\left(\sum_j \left| F^{(2)}_{jk} - F^{(1)}_{jl} \right|\right) \tag{3.4}$$

where the index j runs over the frequency axis and the indexes k and l runs over the positions of the stages. For a specific l value, the data matrix with elements $F^{(2)}_{jk} - F^{(1)}_{jl}$ is retrieved. Its graphical representation presents a typical checkerboard pattern, see figure 3.7 panel (a) for an example. The absolute value of this matrix is spectrally integrated obtaining an oscillating function of x_2. This oscillatory trace has its biggest amplitude in the correspondence of the position of the stage x_2 that assures an equal delay for the two pulses. The envelope of this oscillating curve is computed subtracting the constant part and taking the absolute value of the Hilbert transform [51], obtaining the solid black line in figure 3.7 panel (b). Matrix $\mathbf{H}^{(2)}$ is constructed collecting all the envelopes derived from all the possible l indexes, see figure 3.7 panel (c).

A linear function can be used to fit the trend observed in matrix $\mathbf{H}^{(2)}$. The function is defined as

$$z_2(x_1) = mx_1 + q, \tag{3.5}$$

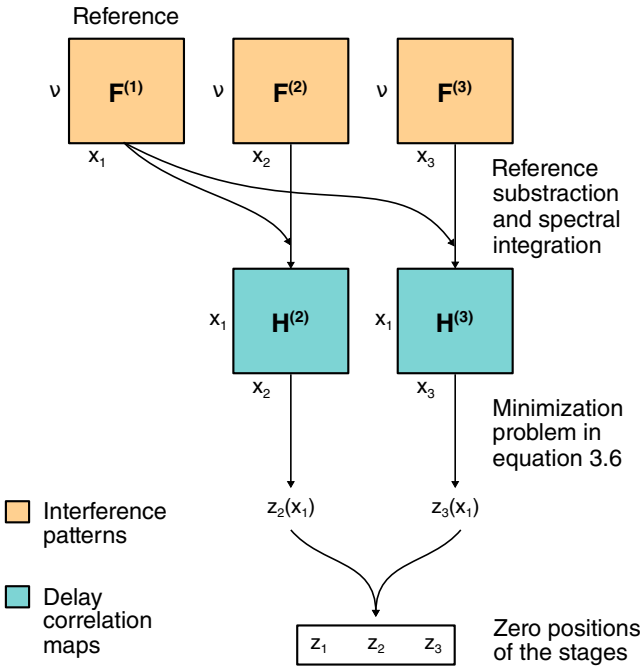

Figure 3.6: Scheme of the data analysis procedure for the determination of the zero positions of the stages.

where m and q are slope and intercept of the linear function. Each point on this line can be used as actual zero position of the wedge calibration. In other words, with this linear function we can choose an arbitrary position as zero of the reference stage and automatically get the zero position for the other stages. In order to practically and reliably obtain the parameters m and q of the linear function we can fit matrix $\mathbf{H}^{(2)}$ with a Gaussian surface $\mathbf{G}$. The center of the Gaussian function is modeled with the linear function in equation 3.5

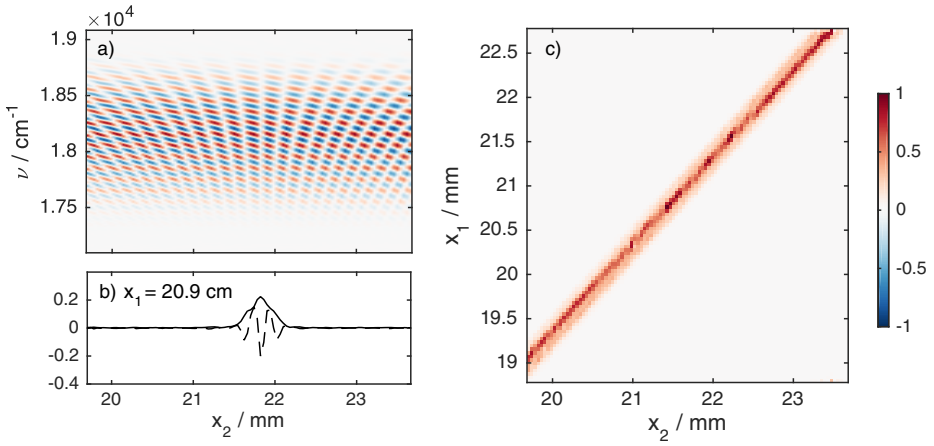

Figure 3.7: Intermediate steps for the evaluation of the zero positions of the stages: (a) matrix resulting from the subtraction of a reference interference spectrum taken from matrix $\mathbf{F}^{(1)}$ at x_1 = 20.9 cm from matrix $\mathbf{F}^{(2)}$; (b) the dashed line is the spectrally integrated absolute value of the matrix in panel (a) and the solid line is the envelope obtained from the Hilbert transform; (c) matrix $\mathbf{H}^{(2)}$ showing a clear signature only at the (x_1, x_2) coordinates where the pulses are synchronous.

obtaining a Gaussian tunnel shape. The matrix element of $\mathbf{G}$ are defined as

$$\begin{aligned} G_{jk}(a,b,m,q) &= ae^{-\left(\frac{x_{2,k}-z_2(x_{1,j})}{b}\right)^2} \\ &= ae^{-\left(\frac{x_{2,k}-(mx_{1,j}+q)}{b}\right)^2}, \end{aligned} \tag{3.6}$$

where a is a scaling factor, b is the width of the Gaussian function and the indexes j and k are associated to the j-th and k-th positions $x_{1,j}$ and $x_{2,k}$, respectively. Then the following unconstrained least square minimization

problem is solved

$$\min_{(a,b,m,q) \in \mathbb{R}^4} \quad \left|\left|\mathbf{H}^{(2)} - \mathbf{G}(a,b,m,q)\right|\right|^2, \tag{3.7}$$

Given a good set of starting parameters, the Gaussian surface is rapidly fitted. We then repeat the same procedure for the third pulse, and choose an arbitrary x_1 value, obtaining a tern of zero stage positions z_1, z_2 and z_3 in which the three exciting pulses are overlapped in time. This condition is used as the time-zero of the experiment. The procedure is schematically described in figure 3.6.

Evaluation of linear calibration coefficients

The second part of the calibration procedure consists in determining the linear coefficients c_1, c_2 and c_3 that allow accurately moving the pulses from the zero positions. The easiest method would be using a two points calibration for each beam: given two SI at two different positions, the Fourier transform can be used to get the two corresponding values of delay. The slope of the line connecting the two points in a time-space plot is the searched parameter c_i. As already mentioned, this procedure is not accurate enough because of the relatively high error in determining the delay from Fourier transform peaks. All the information about the evolution of pulses timing are contained in the $\mathbf{F}^{(i)}$ matrices. We must use a procedure which gives conversion coefficients able to guarantee, at the maximum excursion of the linear stages, an error in timing much smaller than the optical cycle of the electromagnetic radiation. This accuracy will assure that the final signal recorded during experiments is phase-locked. The idea at the basis of the proposed procedure is to mathematically compensate for the evolution of the spectral interference coupled to the movement of the wedge. In other words, we want to determine which is the exact delay to be mathematically subtracted in order to achieve a interference pattern perfectly constant along the whole wedge scan. We will describe the

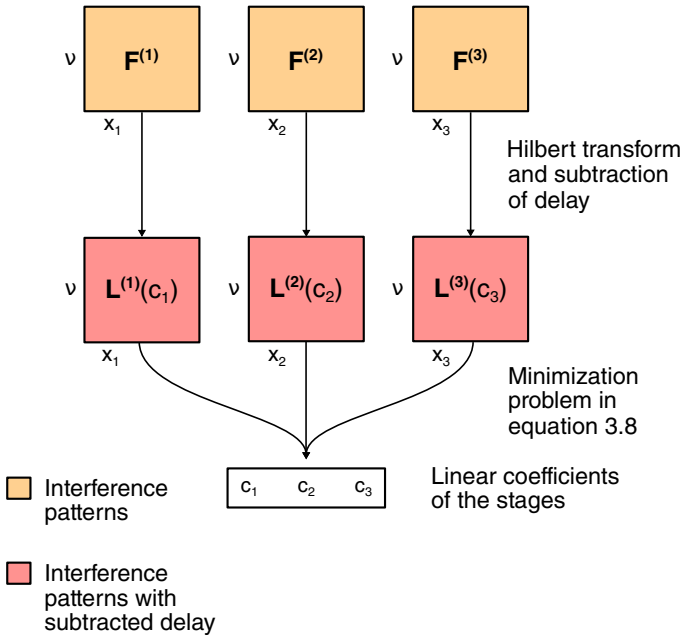

Figure 3.8: Scheme of the data analysis procedure for the determination of the linear calibration coefficients of the stages.

procedure for the pulse with $i = 1$, the same will apply for the other pulses. The procedure is outlined in figure 3.8.

Firstly, matrix $\mathbf{F}^{(1)}$ is Hilbert transformed along the frequency axis in order to operate on complex numbers. This allows subtracting the delay $\tau_1(x_1) = c_1(x_1 - z_1)$ from the spectral interference by multiplying for an oscillating exponential function as

$$L^{(1)}_{jk}(c_1) = F^{(1)}_{jk} e^{-\mathrm{i}2\pi\nu_j c_1 (x_{1,k} - z_1)}, \tag{3.8}$$

where for the correct c_1 value, the matrix $\mathbf{L}^{(1)}$ is a collection of constant interference spectra. This operation cancels out the time delay τ_1 induced by moving

the WP from the zero position z_1. In order to retrieve the exact parameter c_1, we can solve a maximization problem for an objective scalar function which exploits the condition of constant interference pattern that we want achieve. The problem is defined as

$$\max_{c_1 \in \mathbb{R}} \quad \sum_j \left| \sum_k L^{(1)}_{jk}(c_1) \right|, \tag{3.9}$$

where the first summation over the index k, which runs over the stage positions, is going to output non-null values only if no oscillation is present along that direction. The second summation has the purpose of obtaining the final scalar function to be maximized. Repeating the procedure for the tree stages, all the parameters c_i are recovered.

In order to be sure that the relative phase difference between pairs of pulses is locked for the full movement of the WPs, a further control measurement is performed. The interference spectra in matrices $\mathbf{F}^{(i)}$ used for the previous calculation are sampled only on a limited portion of the stage movement range, because at large delay values the spectrometer is not able to resolve efficiently all the fringes of the interference spectra. This is not detrimental for the accurate evaluation of the zero positions of the stages but it can weaken the accuracy of the calibration at the extreme positions of the stages. In order to guarantee the accuracy of the linear calibration coefficients along the whole wedge range, we can directly check that the relative phase difference between pair of pulses is conserved also at the extreme positions. The possible presence of small errors of fractions of optical cycle can then be corrected. As we will see in section 3.6 the relevant couple of pulses to check is (1,2) since they are the only ones that are effectively moved during experiments along the whole length of the optical wedges. The third pulse and LO are fixed during rephasing and non-rephasing measurements, and are not delayed relevantly in double-quantum experiments.

In practice, using the calibration obtained above, τ_1 is scanned keeping $\tau_2 - \tau_1$ constant, obtaining the matrix $\mathbf{F}^{(1,2)}$. If the spectral interference is constant for the full WP movement range, then the calibration is accurate and ready for the experiment. If a small linear drift of the phase of the interference is observed, it must be corrected to avoid phase drift also of the third order signal. It is possible to define a corrected interference pattern as

$$L_{jk}^{(1,2)}(p) = F_{jk}^{(1,2)}\ e^{-\mathrm{i}2\pi\nu_j(p\tau_{1,k})} \tag{3.10}$$

where $p\tau_{1,k}$ is the small delay correction to be applied, and p is an adimensional scaling parameter. Analogously to problem 3.9 we can maximize a scalar function solving the following problem

$$\max_{p\,\in\,\mathbb{R}} \quad \sum_j \left| \sum_k L_{jk}^{(1,2)}(p) \right|. \tag{3.11}$$

Since we are making a small correction, we can assume that c_1 of the reference beam is exact. It can be demonstrated that the corrected coefficient $c_{2,\mathrm{corr}}$ for the other beam can be expressed by

$$c_{2,\mathrm{corr}} = c_2\left(p+1\right). \tag{3.12}$$

This correction is very small (usually smaller than the 0.05%), but is fundamental for removing any phase trend of the third order signal induced by calibration uncertainty.

Evaluation of the delay from LO

The last step is retrieving the precise value of τ_{LO}. It cannot be easily determined by the SI generated by the 25 μm pinhole because this configuration does not reproduce the exact working conditions of the 2DES experiments.

We therefore exploit the heterodyne non-resonant FROG of a solvent in a cell. This procedure consists indeed in collecting the interference pattern produced by the LO and the non-resonant third order signal of the solvent. During this experiment τ_1 is scanned while the three exciting pulses are kept simultaneous, that is $\tau_1 = \tau_2 = \tau_3$. The function $\tau_{\mathrm{LO}}(\tau_1)$ is estimated with a linear fit so that the exact value of $\tau_{\mathrm{LO}}(\tau_1 = 0)$ is determined.

The overall calibration method resolves some of the most important issues of non-collinear 2DES setups [23], and a proper execution of this procedure is crucial to obtain high quality 2DES data.

3.6 Pulse sequence definition and scan order

In 2DES experiments, the phase of the heterodyne detected signal is function of the individual phases of each pulse and depends upon phase matching conditions [10]. For rephasing (R), non-rephasing (NR) and double quantum (2Q) experiments, the signal phase ϕ_S is given as

$$\begin{aligned} \phi_S^{\mathrm{R}} &= -\phi_1 + \phi_2 + \phi_3 - \phi_{\mathrm{LO}} \\ \phi_S^{\mathrm{NR}} &= +\phi_1 - \phi_2 + \phi_3 - \phi_{\mathrm{LO}} \\ \phi_S^{\mathrm{2Q}} &= +\phi_1 + \phi_2 - \phi_3 - \phi_{\mathrm{LO}}, \end{aligned} \tag{3.13}$$

where ϕ_1, ϕ_2 and ϕ_3 are the phases of the three exciting pulses and ϕ_{LO} is the phase of the local oscillator.

The implemented setup allows for a completely independent control of the delay of each pulse with respect to the others, so it is necessary to decide which is the most convenient way to perform a 2DES experiment. We found that the most suitable configuration consists in fixing the delay of the pulse generating the third interaction with the system, which is k_3 for rephasing and non-rephasing signals and k_1 for double-quantum signal. The remaining two pulses are scanned accordingly to construct the full 2DES spectra. The choice

of fixing the last pulse interacting with the sample has two major benefits: (i) the signal is generated at about the same delay with respect to LO and its spectral interference does not change much during the experiments. Fixing one of the other two pulses will have the consequence to move considerably the signal in time, pushing the recorded spectral interference near the limit of the resolution of the spectrograph and possibly generating false decays of the signals; (ii) since two of the four pulses defining the phase of the signal are fixed (equation 3.13), a greater phase stability is achieved.

To obtain a 2DES dataset, it is not necessary to scan the delay time t_3 because its Fourier transform is readily available from the spectral interference with LO. The two remaining delay times must be scanned using combinations of wedges movements. The most critical scan is t_1 because during this delay period the system is evolving in a quantum coherence between ground and excited electronic states, which oscillates in the optical frequency range. In principle an high sampling is requested in order to fulfill the Nyquist conditions, for example at 600 nm a time step of at least 1 fs is required for t_1. The sampling rate of the t_2 scan can be much slower because during the population time only quantum coherences between states with energy within the laser bandwidth can be excited, that is the recorded oscillations have typical frequency in the order of only few thousands of cm^{-1}. For example, for a laser spectrum with a bandwidth of 2000 cm^{-1} a minimum time step of 8.3 fs is required for the population time. The same time step can be used also for the scan of t_1 if a rotating frame is introduced in the data processing step, see section 3.8.

3.7 Signal acquisition

A the double lock-in modulation acquisition [40, 45] was implemented in order to suppress the spurious contributions in the recorded spectra, i.e. removing the scattering of the exciting pulses. In this acquisition procedure, the signal

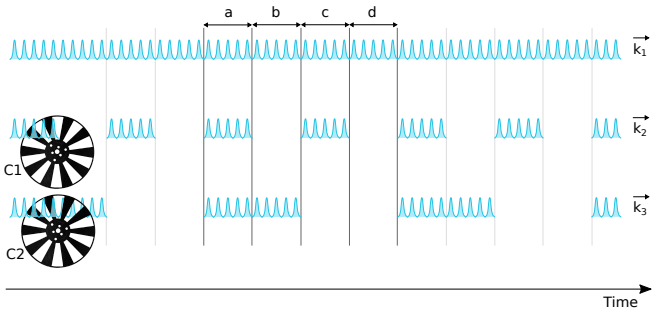

Figure 3.9: Schematic representation of the double modulation lock-in detection. During a complete cycle of the optical chopper with the lower frequency four different situations can be realized: (a) all the beams reach the sample and the third order signal is generated; (b) beam k_2 is blocked, no signal is generated, and only the scattering of k_1 and k_3 is recorded; (c) beam k_3 is blocked, no signal is generated, and only the scattering of k_1 and k_2 is recorded; (d) both pulses k_2 and k_3 are blocked and only the scattering of k_1 is recorded.

is modulated at a specific frequency by mean of two optical choppers and therefore it can be isolated from all the other contributions using the Fourier transform. In our setup, the CCD camera collects series of spectra with a repetition rate of ν_{CCD} = 500 Hz. Pulse by pulse acquisition is not possible because the CCD is not fast enough to follow the 3 KHz repetition rate of the laser source. Two exciting pulses, k_2 and k_3, are modulated respectively at ν_{f_1} = 200 Hz and ν_{f_2} = 40 Hz with optical choppers. As a result the signal is extracted at $\nu_s = \nu_{f_1} - \nu_{f_2}$ = 160 Hz, which is the difference of the two modulating frequencies. See figure 3.9 for a schematic representation of the acquisition scheme.

The laser pulse train, the CCD camera and the optical choppers are reciprocally triggered and phase-locked. Each modulation frequency must be chosen accurately. Indeed, it is necessary to extract the signal at a frequency

×	E_1^*	E_2^*	E_3^*	E_{LO}^*	E_S^*
E_1	$\|E_1\|^2$	$E_1E_2^*$	$E_1E_3^*$	$E_1E_{LO}^*$	$E_1E_S^*$
E_2	$E_2E_1^*$	$\|E_2\|^2$	$E_2E_3^*$	$E_2E_{LO}^*$	$E_2E_S^*$
E_3	$E_3E_1^*$	$E_3E_2^*$	$\|E_3\|^2$	$E_3E_{LO}^*$	$E_3E_S^*$
E_{LO}	$E_{LO}E_1^*$	$E_{LO}E_2^*$	$E_{LO}E_3^*$	$\|E_{LO}\|^2$	$E_{LO}E_S^*$
E_S	$E_SE_1^*$	$E_SE_2^*$	$E_SE_3^*$	$E_SE_{LO}^*$	$\|E_S\|^2$

Table 3.1: All the possible contributions to the signal recorded by the detector, which is sensitive to field intensity. Only the real part of those contributions are effectively registered. Thanks to the double lock-in method most of the spurious contributions are removed (in black), and only the ones highlighted in red survive.

lower than the Nyquist limit imposed by the CCD camera, that is $\nu_{CCD}/2 = 250$ Hz. Moreover, to achieve a phase-locked signal, it is necessary that the higher frequency modulation is a multiple of the slower one. Given all the necessary constraints, the two frequencies are taken one as odd multiple of the other, i.e. $\nu_{f_2} = \nu_{f_1}/(2n+1)$, with n positive integer. This guarantees that ν_s is always an even multiple of the slower modulation and it is not contaminated by odd higher harmonics originated from the square waves of the modulated scattering of single beams.

With this method, most of the scattering contributions are removed, since they reach the CCD camera with the frequency of modulation of a single chopper or they are not modulated at all. However, the acquired signal still contains the unwanted homodyne third order signal, the spurious contribution arising from the interference between the signal and the scattering of the non-modulated beam and the interference between the scattering of the two modulated beams; table 3.1 specifies all the possible contributions.

3.8 Data processing

The raw signal acquired by the CCD with double lock-in detection is expressed as

$$S_a = |E_S|^2 + 2\Re\{E_S E_{LO}^*\} + \tag{3.14}$$

$$2\Re\{E_S E_1^*\} + 2\Re\{E_3 E_2^*\}. \tag{3.15}$$

An example of rephasing data collected at a fixed population time is reported in figure 3.10 panel (a). The emission wavelength axis is immediately interpolated [52] in order to achieve an evenly spaced frequency axis. This assures a correct output of the fast Fourier transform algorithm when acting on this axis. Our aim is to isolate the pure signal E_S from the contribution $E_S E_{LO}^*$. To this purpose, we need to operate on the complex data. We must recognize that E_S is generated after the interaction of the pulse k_3 with the sample. To impose this causality condition, the inverse Fourier transform is performed along ν_3 and only the peak at negative time delays is retained. The resulting data are then Fourier transformed back. The interference between LO and the third order signal is now associated with a negative delay. This operation, coupled with the subsequent addition of the delay between k_3 and LO in equation 3.18, will assure a positive value of t_3 for the final signal, see also figure 3.11. After this set of operations the signal S_a become complex valued S'_a: the real part is equal to the data recorded from the CCD and the imaginary part is a copy of the original data with a phase shift of $-\pi/2$.

In order to reduce the number of data point acquired along t_1, a rotating frame approach (RF) is applied [53]. The optical frequency of the signal during t_1 is detuned subtracting a reference frequency ν_{ref}, which is usually taken as

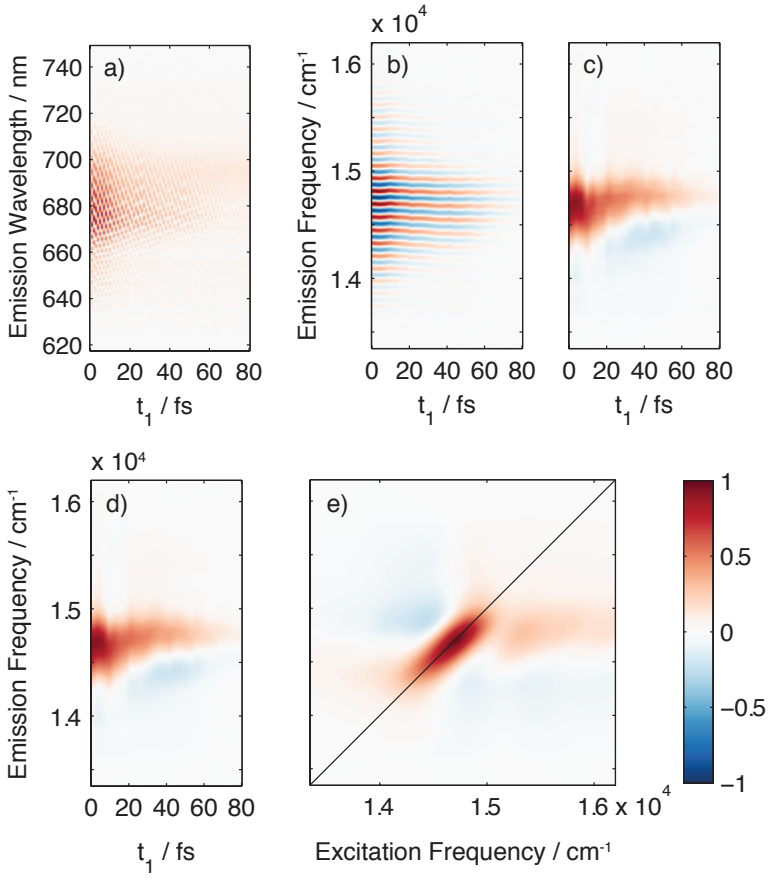

Figure 3.10: Snapshots of the data along a data processing session. (a) Raw signal acquired for a rephasing experiment at a fixed value of t_2; (b) signal after the application of the rotating frame approach; (c) the correction for the delay with respect to LO is applied removing the horizontal fringes; (d) a window filter is applied in the t_3 domain producing a smoothing and removal of the residual spurious contribution; (e) final 2DES map obtained after Fourier transform along t_1, shift from the reference frequency and phase correction.

the central frequency of the laser bandwidth

$$S_{b,\mathrm{R}} = S'_{a,\mathrm{R}}\, e^{i2\pi\nu_{\mathrm{ref}}t_1}, \tag{3.16}$$

$$S_{b,\mathrm{NR}} = S'_{a,\mathrm{NR}}\, e^{-i2\pi\nu_{\mathrm{ref}}t_1}, \tag{3.17}$$

With this operation, the resulting signals $S_{b,\mathrm{R}}$ and $S_{b,\mathrm{NR}}$ have only slow modulations during the coherence time t_1 and it is thus possible to greatly reduce the sampling frequency of the signal along the t_1 axis. The maximum frequency observed in the RF signal corresponds to half of the bandwidth of the laser spectrum, which is in the order of few thousands of cm^{-1}. In other words, thanks to the RF, it is possible to collect interferograms along t_1 with a sampling rate lower than the optical Nyquist limit. We are limited only by the frequency difference between ν_{ref} and the border frequencies of the laser spectrum.

Once retrieved the S_b signals (figure 3.10 panel (b)), the delay between LO and the zero of the experiment must be added to the data in order to get rid of the horizontal fringes,

$$S_c = S_b\, e^{i2\pi\nu_3\tau_{\mathrm{LO}}}. \tag{3.18}$$

As described in section 3.5, the delay between the zero of the experiment and LO is measured exploiting the heterodyne detection of the non-resonant FROG signal of a pure solvent. The distance of LO from the zero of the experiment (τ_{LO}) controls how dense are the fringes of the interference pattern in the collected spectra. This parameter must be chosen carefully because it affects the subsequent windowing step of the signal. Figure 3.11 summarizes schematically all the delay computations.

In order to remove the final spurious contributions from the signal, a time-filtering in the t_3 dimension is applied. The filter is tuned to keep only the portion of the t_3 axis between zero and about 80-100 fs, where the signal appears. This operation allows removing most of the the remaining spurious contributions in equation 3.14. The initial transient of the signal can be slightly

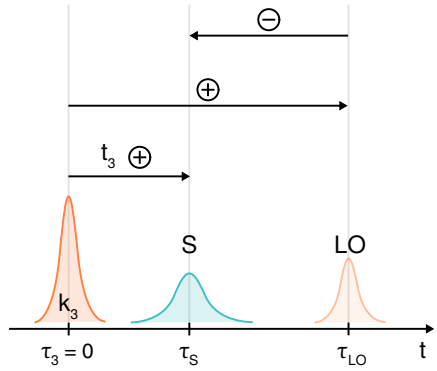

Figure 3.11: Schematic representation of the delay computations necessary for imposing the causality condition to the signal. In our time scan, k_3 is kept fixed during the measurement (3.6). Also the delay between LO and k_3 is taken positive. The delay between LO and the signal is the experimentally accessible one, it has to be imposed negative whit a Fourier filtering in order to obtain a positive t_3, in agreement with causality condition.

affected by $E_S E_1^*$ and $E_3 E_2^*$ when the delay between signal and k_1 pulse and the delay between k_3 pulse and k_2 pulse are inside the filter window, respectively. This condition is verified only at early values of population time and does not arise any concern for the rest of the data. The final step in order to obtain the final maps is the Fourier transform along t_1, or t_2 in the case of double quantum maps. The resulting excitation frequency ν_1 of rephasing and non-rephasing maps must be then shifted by ν_{ref} frequency to account for the rotating frame. Finally we must get rid of the arbitrary phase of the signal. Pump-probe spectra are collected using the same setup using k_3 as pump pulse and the local oscillator as probe. The phase correction that guarantees the best match between the real absolute total signal projection and the pump probe spectrum is employed.

CHAPTER 4

Data Analysis

Two dimensional electronic spectroscopy is gaining higher recognition worldwide as optical spectroscopic technique. From the experimental point of view, setups and signal acquisition procedures are becoming solid and reliable. On the other hand, fully established and standardized data analysis methods are still missing and this leads to a difficult extraction of complete information. It is thus necessary to develop global and robust data analysis procedures able to capture the complete picture with an increased level of clarity and reliability. In this chapter two innovative approaches to the data analysis of 2DES data will be discussed. In section 4.1 the state-of-the-art of 2DES data analysis is reviewed. In section 4.2 the use of time-frequency analysis for the study of the coherent dynamics along the population time is discussed and an optimized method is then developed. Finally, in section 4.3 a global analysis method for the simultaneous investigation of population and coherence dynamics is reported.

4.1 State-of-the-art

In 2DES, the third order signal is displayed as frequency-frequency 2D maps evolving during the population time, t_2. The evolution of the signal as a function of t_2 carries information about the dynamics of the excited states, including the possible presence of coherent mechanisms, particularly investigated in the latest years [24, 16, 6]. As outlined in chapter 2, within the response function formalism, the third order signal can be expressed as a sum of contributions represented graphically by double-sided Feynman diagrams [10, 22, 54]. These contributions can be classified in two groups depending on the evolution of the signal during t_2 as shown in figure 4.1. The first group includes non-oscillating pathways, represented by Feynman diagrams where the system reaches a pure state after the first two interactions. The second group consists of oscillating contributions described by Feynman diagrams where, after the first two interactions, the system is in a coherent superposition of states.

In the first case, the signal evolves in t_2 following the relaxation dynamics of the excited states that can be quantified through the solutions of suitable kinetic differential equations. For example, in the simplest case of parallel relaxation processes, the solutions of the rate equations are real exponential functions [55]. In the second case, the signal oscillates during t_2 with a frequency proportional to the energy gap of the states that generate the coherence. These oscillations dampen over time according to their dephasing rates, depending on the nature of states themselves, on the temperature, on the environment etc., and are well described by complex exponential functions.

The analysis of the oscillations bringing the information on coherent dynamics can be quite puzzling, since typically they are the results of the superposition of several beating components, each of which is characterized by different frequencies and time-dependent amplitudes. This is what is generally defined as multi-component non-stationary oscillatory behavior. In order to

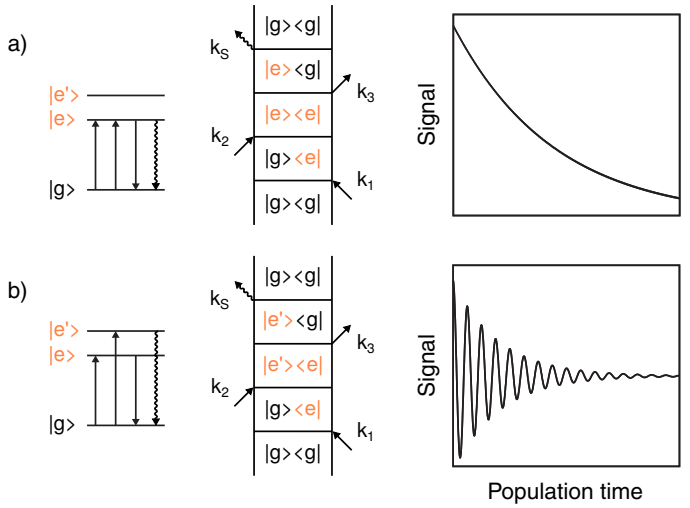

Figure 4.1: Examples of energy level schemes and Feynman diagrams representing (a) non-oscillating and (b) oscillating contributions to the signal. Right panels sketch the dynamics of the corresponding signals as a function of population time.

assess the nature of the different components, one must extract from the overall signal not only the frequency of the different components, associated with the energy of the states involved in the coherent superposition, but also their time behavior, whose knowledge may represent a valuable help in the assessment of their nature.

Several methods have been proposed to analyze 2DES signals as function of t_2. Global analysis of population dynamics alone is an established procedure, and real multi-exponential models are the most used to fit the data because they do not require any additional assumption[56, 57]. The coherent dynamics is left in the residuals of the non-oscillatory model, requiring a second step of analysis, see figure 4.2. Different methods have been proposed to this aim, such as Fourier transform (FT) to achieve FT-maps [58, 59, 60], linear prediction

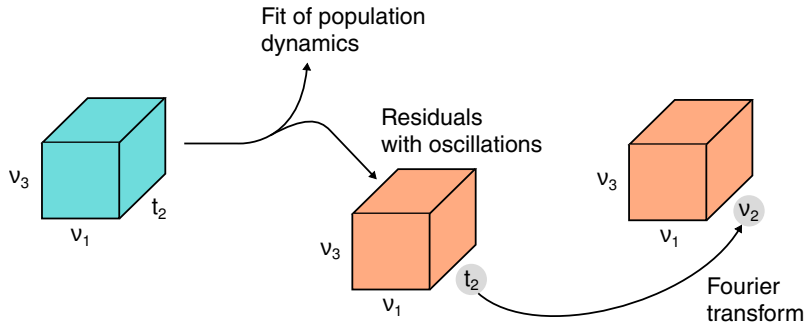

Figure 4.2: Schematic representation of the state-of-the-art analysis of 2DES data. The population dynamics is fitted with a suitable kinetic model in a preliminary step. The coherent dynamics is left in the residuals and the Fourier transform is applied.

Z-transforms [61, 62, 63] and time-frequency decomposition techniques. The latter method was proposed for the analysis of ultrafast optical responses by Prior *et al.* using continuous wavelet transforms [64], but it is not fully exploited and its application to experimental data is still not developed. Continuous wavelet transform and other linear and bilinear approaches will be analyzed and compared in section 4.2, following the content of the published paper [65].

All the methods mentioned above have the principal scope to retrieve spectral information in the population time. The strength of this kind of analysis is its model independence, i.e. it does not requires *a priori* information on the system. But there is also some intrinsic limitation that can hardly be overcome, the most important one is their non-global character. The global method developed in section 4.3 relies on a multi-exponential model. The application of this method requires some additional effort to understand which is the most suitable model for the investigated system, but surely represents a more robust approach.

4.2 Time-frequency analysis [65]

Time-frequency signal analysis deals with the analysis and processing of signals with time-varying frequency content. Such signals are best represented by a time-frequency transform (TFT), which is intended to show how the energy of the signal is distributed over the two-dimensional time-frequency space. These techniques, borrowed from the signal processing field, have been adapted and applied to the analysis of 2D oscillating signals. The processing of the signal may then exploit the features produced by the visualization of signal energy in two dimensions (time and frequency) instead of only one (time or frequency). Despite the recognized importance of extracting also dynamical information, the current analysis techniques of 2DES data are based mainly on Fourier transform analysis which is able to interpret the information content of an oscillating signal only in terms of its frequency components. The idea of explicitly considering also the time dimension naturally leads to the time-frequency concept and its representations.

The time-frequency transforms here investigated, providing simultaneously frequency and time resolution, unveil the dynamics of the relevant beating components and supply a valuable help in their interpretation. In order to fully exploit the potentiality of this method, several TFTs have been tested in the analysis of sample 2D data. Possible artifacts and sources of misinterpretation have been identified and discussed.

The two classical representations of a signal are the time-domain representation $s(t)$ and the frequency-domain representation $S(\nu)$. In both forms, the variables t and f are treated as mutually exclusive: to a obtain a representation in terms of one variable, the other variable is "integrated out". Consequently, each classical representation of the signal is non-localized with respect to the excluded variable; that is, the frequency representation is essentially the average of the values of the time representations at all times, and the time

representation is essentially the average of the values of the frequency representations at all frequencies. In the time-frequency representation, denoted by TFT(t,ν), the variables t and f are not mutually exclusive, but present together. Indeed, the TFT is localized in t and f.

It is important to stress that the possibility of retaining information both in time and in frequency domain cannot be achieved at any cost. Indeed, transforms are subject to the time-frequency uncertainty principle and thus it is not possible to reach simultaneously ideal resolution along both dimensions. Moreover, the possibility of maintaining the joint information across the time-frequency plane often leads to artifacts or aberrations whose importance depends on the nature of the signal and on the particular TFT employed. It is thus of pivotal importance to know the characteristics of the different available TFTs to select from time to time the approach and the parameters most suitable for the specific input signal to be analyzed and for the specific expected output.

Given their generality, time-frequency transforms have found applications in several fields, from the interpretation of geophysics phenomena [66], to physiological responses [67], to radio- and tele-communications [68] and their use has been intensified in particular in the last two decades. If the intensification of their use had the beneficial effect of providing the user with new and increasingly sophisticated tools, their development in fields often very different gave rise to an anthology of different developments that sometime makes quite difficult their actual use for specific applications. The main objective of this section is to present the main time-frequency methods available today and apply them specifically to oscillating signals obtained through multidimensional coherent spectroscopy. The application of time-frequency techniques, well established in other fields, is instead still poorly developed in spectroscopy. Indeed, apart from the pioneering works of T. Kobayashi and A. Stolow, who have demonstrated TFTs in analyzing wavepacket dynamics in ultrafast pump-probe signals, few are the examples of TFT analysis applied to spectroscopic

signals. In particular the sliding-window Fourier Transform (or short-time Fourier transform) was successfully applied, for example, toward analysis of complex wavepacket dynamics in the gas-phase [69], dynamical mode coupling and mode-mixing [70, 71], and real-time reaction dynamics in the condensed phase [72, 73].

4.2.1 The need for a time-frequency representation

We will begin the discussion of the time-frequency methods with a brief review of the Fourier transform. Any non-stationary signal can be naturally described as a function of the time, i.e using the time representation $s(t)$. This leads immediately to the definition of the instantaneous power, $|s(t)|^2$, which shows how the energy of the signal is distributed over time. The total energy of the signal is recovered after time integration of the instantaneous power,

$$E = \int_{-\infty}^{+\infty} dt\, |s(t)|^2. \tag{4.1}$$

As already mentioned, the time domain representation tends to obscure information about frequency. The Fourier transform (FT) can be employed to recover the representation in the frequency domain $S(\nu)$, it is defined as

$$S(\nu) = \mathrm{FT}\,[s(t)] = \int_{-\infty}^{+\infty} dt\, s(t) e^{-i2\pi\nu t}. \tag{4.2}$$

The Fourier transform is in general complex and its magnitude and phase are respectively called the magnitude and phase spectrum. The square of the magnitude spectrum is also called the power spectrum, $|S(\nu)|^2$, and it shows how the energy of the signal is distributed over the frequency domain. The total energy can be obtained again integrating the power spectrum

$$E = \int_{-\infty}^{\infty} d\nu\, |S(\nu)|^2. \tag{4.3}$$

Although the frequency representation $S(\nu)$ is a function of frequency only, the FT is a complete representation of the signal because the time domain signal can be recovered by taking the inverse Fourier transform (IFT)

$$s(t) = \mathrm{IFT}\left[S(\nu)\right] = \int_{-\infty}^{+\infty} d\nu \; S(\nu) e^{i2\pi\nu t}. \tag{4.4}$$

Hence, the Fourier transform does not delete any detail of the signal but it hides the information about timing, encoding it in a non trivial way in the magnitude and the phase spectrum.

A well known property of the two Fourier transform representations, $s(t)$ and $S(\nu)$, is the uncertainty principle which states that the time duration Δ_t of $s(t)$ and the frequency bandwidth Δ_ν of $S(\nu)$ are related by

$$\Delta_t \Delta_\nu \geq \frac{1}{4\pi}, \tag{4.5}$$

where

$$\begin{aligned} \Delta_t &= \left[\frac{\int_{-\infty}^{\infty} dt \; (t-\mu_t)^2 s(t)^2}{\int_{-\infty}^{\infty} dt \; s(t)^2} \right]^{1/2} \\ \Delta_\nu &= \left[\frac{\int_{-\infty}^{\infty} d\nu \; (\nu-\mu_\nu)^2 S(\nu)^2}{\int_{-\infty}^{\infty} d\nu \; s(\nu)^2} \right]^{1/2}. \end{aligned} \tag{4.6}$$

The mean time μ_t and the mean frequency μ_ν are defined as weighted averages of time and frequency over the instantaneous power and the power spectrum, respectively, giving

$$\begin{aligned} \mu_t &= \frac{\int_{-\infty}^{\infty} dt \; t s(t)^2}{\int_{-\infty}^{\infty} dt \; s(t)^2} \\ \mu_\nu &= \frac{\int_{-\infty}^{\infty} d\nu \; \nu(\nu)^2}{\int_{-\infty}^{\infty} d\nu \; s(\nu)^2}. \end{aligned} \tag{4.7}$$

Therefore, the larger the time duration of $s(t)$, the smaller the frequency band-

width of $S(\nu)$, and *vice versa*.

In spite of the completeness of the Fourier transform and the uniqueness of the representation, in many applications it does not adequately reflect the actual characteristics of the signal. The standard Fourier analysis plays an important role in signal processing, because it allows an easy and efficient decomposition of a signal into individual frequency components and establishes the relative intensity of each component. Nevertheless, FT is not the best tool for characterizing signals that only last for a short portion of the investigated time window or whose frequency contents change over time, situations that often happen in ultrafast spectroscopy signals.

The solution is to seek a representation of the signal as a two-variable function whose domain is the two-dimensional (t, ν) space. Its constant-t cross section should show the frequency or frequencies present at time t, giving an instantaneous power spectra, whereas its constant-ν cross section should show the the time or times at which the frequency ν is present, expliciting the time evolution of each frequency component.

Figure 4.3 shows two examples of time-frequency representation for two different signals. In panel (a) the presence of three different components can be guessed from the study of the temporal representation of the signal. The first component affects the initial portion of the signal, the second component affects the central portion and the third component affects the final portion. A definite answer on the number of components and the quantitative determination of the frequencies is obtained from the frequency representation of the signal, three peaks with identical intensity are recovered. The most complete picture of the signal is given by the time-frequency representation which is represented as a two-dimensional plot. The features of the representation are located at the crossing region between the time portion of the signal affected by the specific component and its peak in the frequency representation. Panel (b) illustrates a case in which using a TFT is of fundamental importance, that is for

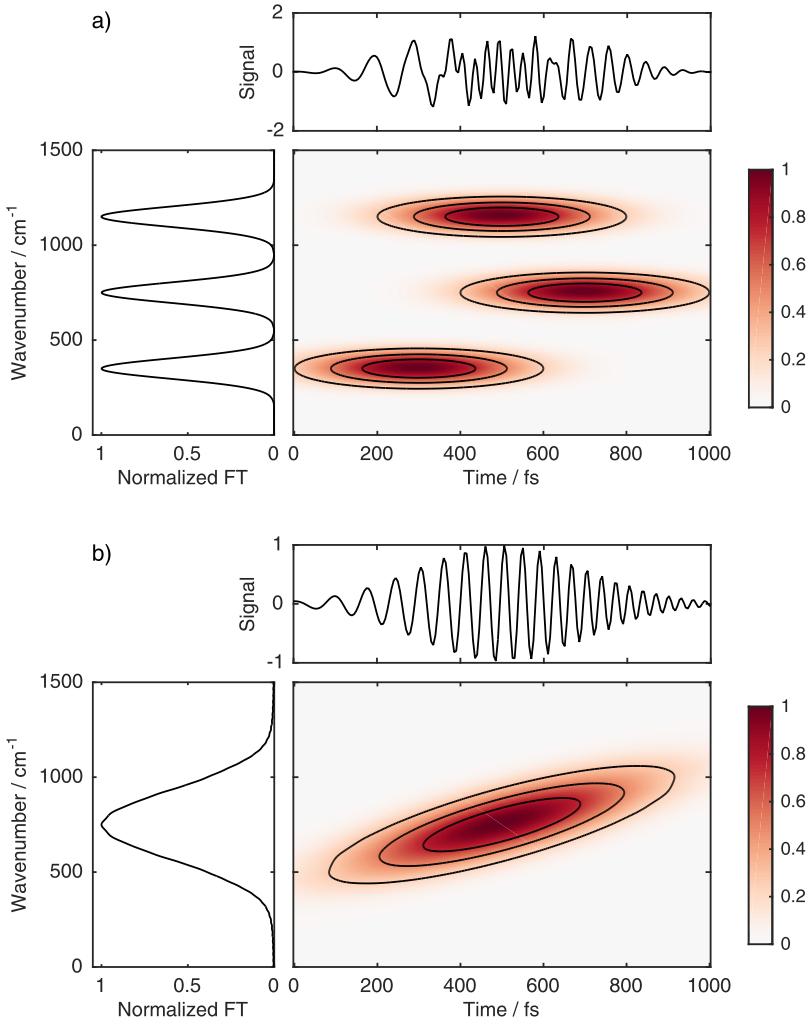

Figure 4.3: Example of simulated signals in which a time-frequency representation can give a better understanding of the signal properties. In the three-components signal (a) the Fourier transform shows three identical peaks that correspond to signal components at different time delays. In the chirped signal (b) the Fourier transform shows a single symmetrical peak whereas the signal is characterized by an instantaneous frequency changing over time.

unraveling the properties of a chirped signal, i.e. a signal gradually changing frequency over time. From the time representation of the signal it is evident that the instantaneous frequency is increasing over time. The frequency representation is characterized by a single broad peak which provides only the average frequency of the signal. The time frequency representation naturally reveals the properties of the chirped signal showing a single feature that diagonally crosses the time-frequency plane. Moreover it is possible to identify the order of the chirp, which in this example is linear.

Several approaches have been followed historically for the formulation of time-frequency transforms. The most known and diffused are those inspired by Fourier analysis. Other methods are based on a signal-dependent approach, for example using models assuming *a priori* the knowledge of the possible structure of the analyzed signals. Only TFTs belonging to the former group will be considered in this work.

Among them, a fundamental property is the dependence of the representation on powers of the signal $s(t)$. Here, only linear and bilinear TFTs, depending linearly and quadratically on the signal, respectively, will be analyzed. Higher order TFTs are also known but in general they are more difficult to apply and understand. The most known TFTs belong to the so-called Cohen's class [74]. Among them, the attention has been focused in particular on the short-time Fourier transform (STFT), the Margenau-Hill-Spectrogram distribution (MH), the Wigner-Ville distribution (WV), the Choi-Williams (CW) distribution, which present the most suitable properties for the application to spectroscopic signals. A complete overview of the most used Cohen's class functions can be found in refs. [75, 76, 77, 78].

4.2.2 Linear transforms

A crude approach to analyze a signal with time-varying frequency content is to split the time domain signal into many segments, and then take the Fourier

transform of each segment. The generalization of this simple idea dates back to Gabor [79] and it is known as short-time Fourier transform (STFT). It examines the frequency content of the signal as a window function $h(t)$ is moved in time, providing the Fourier transform only of the portion of the signal contained in the window. Due to its simplicity it is the most common linear time-frequency representation. The definition is straightforward:

$$\mathrm{STFT}(t,\nu) = \int_{-\infty}^{+\infty} dt'\; s\left(t'\right) h\left(t'-t\right) e^{-i2\pi\nu t'}. \tag{4.8}$$

This operation differs from the FT in equation 4.2 only by the presence of the window $h(t)$ centered at the time t, which localizes the time information. As the name implies, the STFT is generated computing several Fourier transforms of windowed signals with a shorter duration with respect to the original data. The STFT is in general a complex function which retains the phase information of the signal. Usually it is displayed as the square magnitude, $|\mathrm{STFT}|^2$, called spectrogram, which shows how the power spectrum, i.e. a vertical column of the spectrogram, varies as a function of the time.

The STFT can be defined also in the frequency domain by manipulating equation 4.8 [79] obtaining

$$\mathrm{STFT}(t,\nu) = e^{-i2\pi\nu t} \int_{-\infty}^{+\infty} d\nu'\; S\left(\nu'\right) H\left(\nu-\nu'\right) e^{i2\pi\nu' t}, \tag{4.9}$$

where $H(\nu)$ is the frequency window function obtained as the Fourier transform of $h(t)$. Equations 4.8 and 4.9 are closely related [79]. We can imagine to perform the STFT either in the time domain employing a moving time window function or in the frequency domain employing a moving frequency window function.

Three main observations can be done: (i) signal components with a time duration smaller than the window function tend to get smeared out, therefore the time resolution of the STFT is limited by the width of the time window

$h(t)$, the same applies for the frequency resolution which is limited by the window $H(\nu)$; (ii) the window width in time and the window width in frequency are inversely proportional and constrained by the time-frequency uncertainty principle; (iii) since the width of the window h is constant, the time-frequency resolution is fixed, and thus this method does not suite well the analysis of multiscale signals with spread frequency content.

In order to completely specify the outcome of the STFT, the shape of the window function must be chosen. Several examples of window functions exist, these include rectangular, Barlett, Gaussian, Blackmann and Hanning windows. In general, in order to reduce the ringing artifacts that appear when there is a sharp transition of the signal, the window function should taper to zero smoothly. The Gaussian function window, defined as

$$h(t) = \frac{1}{\sqrt{2\pi}\sigma_h} e^{-\left(\frac{t}{2\sigma_h}\right)^2}, \tag{4.10}$$

is the most commonly used window shape because it achieves the best time-frequency product among all the possible window functions [80]. The balance about time and frequency resolution is controlled by the parameter σ_h: the bigger the value of σ_h, the narrower the frequency bandwidth, and *vice versa*. The effect of the window function shape on the time-frequency transform will be better discussed in section 4.2.4.

In figure 4.4 a synthetic signal is analyzed using the STFT; three Gaussian windows with different widths are employed. The signal includes four oscillating components each with comparable maximum amplitude. In panel (a) the STFT with the shorter window is able to give a good representation of the two components with the sharpest time behaviors, i.e. is able to well resolve the top portion of the time-frequency plane. At the same time the two components with similar frequencies in the bottom part of the time-frequency plane are not resolved completely and some interference artifacts arise in the form of

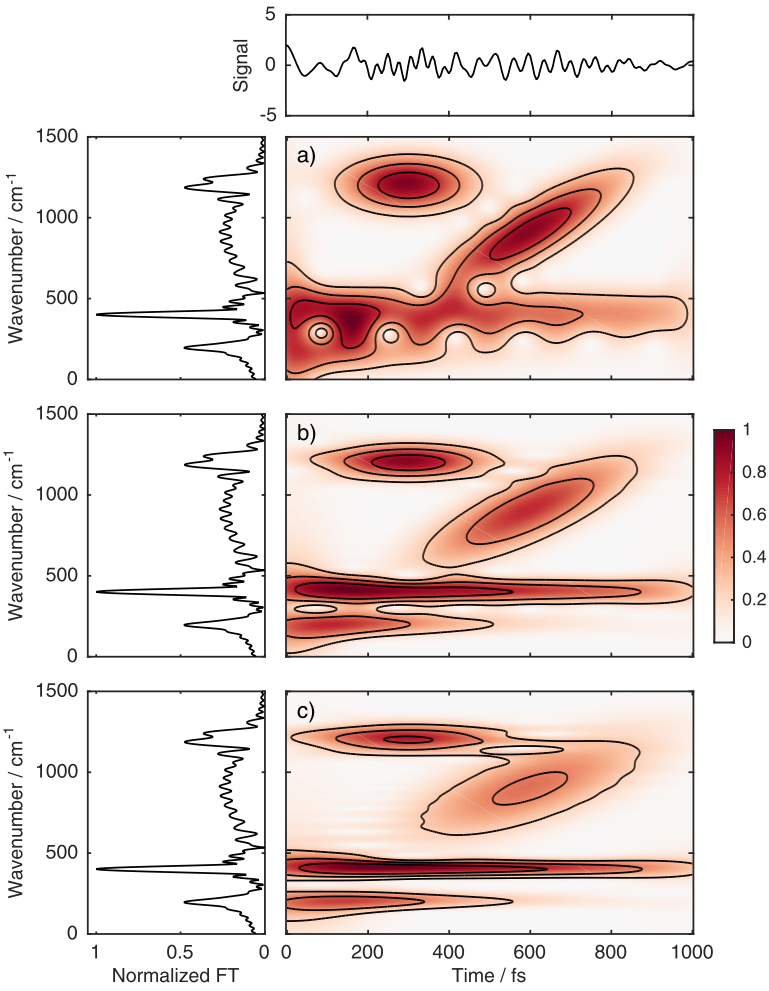

Figure 4.4: Normalized magnitude of STFT of a sample signal using Gaussian windows with σ_h = (a) 50 fs, (b) 100 fs and (c) 150 fs. The analyzed signal contains four oscillating components. Two of the components are characterized by an exponentially decaying amplitude with decay constant 1000 and 300 fs and frequencies of 400 and 200 cm^{-1} respectively. The other two components have a Gaussian time modulation; one component has a frequency of 1200 cm^{-1} and the remaining has a linearly chirped frequency.

beatings. The lower portion of the time-frequency plane is better characterized by the STFT with the widest window in panel (c), indeed a high frequency resolution is necessary to untangle two components very close in frequency. The drawback of using a wider window is a visible smearing of the features with sharp time behaviors. The intermediate representation in panel (b) is a compromise and it is able to give a good overall picture minimizing the amount of interference artifacts. It is clear from this example that the choice of the width of the window function is highly subjective and can be tuned to polarize the time-frequency resolution in order to achieve specific goals.

An approach that can overcome the fixed time-frequency resolution of the STFT is the continuous wavelet transform (CWT). It is a time-frequency representation capable of achieving variable resolution over the time-frequency plane. The CWT transform is defined as

$$\mathrm{CWT}(t,\nu) = \sqrt{\frac{\nu}{\nu_0}} \int_{-\infty}^{+\infty} dt'\, s\left(t'\right) \phi^* \left(\frac{\nu}{\nu_0}(t'-t) \right) \tag{4.11}$$

where $\phi(\cdot)$ is called the mother wavelet and it is a short time oscillating function which is stretched in time using the scale parameter $a = \nu_0/\nu$, and where ν_0 is the central frequency of the wavelet. The parameter a acts as a pseudo frequency since it controls the degree of streching. One of the most used wavelet is the Morlet wavelet, which is based on a Gaussian shape,

$$\phi(t) = \frac{1}{\sqrt{2\pi}\sigma_h} e^{-\left(\frac{t}{2\sigma_h}\right)^2} e^{i2\pi\nu_0 t}, \tag{4.12}$$

where σ_h is the standard deviation of the Gaussian. The wavelet basis function $\phi\left((\nu/\nu_0)(t'-t)\right)$ has variable width according to ν, it is wide for small ν and narrow for higher ν. The resulting magnitude of the CWT at each time t will be higher if the typical frequencies of the signal match the frequency scale a of the wavelet. A distribution is then reconstructed, in which the signals show which wavelet scale contributes more to the wavelet decomposition at a given time.

More details about the applications of wavelet transforms to spectroscopic signals can be found in [64]. This approach is certainly more versatile to probe multiscale frequencies with respect to STFT, indeed dilating $\phi(\cdot)$ at a fixed t, all the multiscale events of the signal at time t can be analyzed according to the scale parameter. Nevertheless, a known drawback of wavelet decomposition is that, being the resolution frequency-dependent, higher frequencies components are typically well resolved in time but less characterized in frequency; and the opposite for the lower frequencies.

4.2.3 Bilinear transforms

The linear representations STFT and CWT perform a sort of 'localized' Fourier transform since they rely on the analysis of the oscillations in a limited time window (h or ϕ) that is translated along the whole time axis. In both cases this implies limitations in the time-frequency resolution. Some of the bilinear TFTs overcome this limitation since they are able to distribute in a more sophisticated way the energy of the signal over the time-frequency plane. The simplest bilinear TFTs are obtained taking the square modulus of the linear STFT and CWT, indicated with $|\mathrm{CWT}|^2$ and $|\mathrm{STFT}|^2$, and referred often as scalogram and spectrogram, respectively. Here the quadratic dependence on the signal is trivial and does not add any peculiar characteristic to the already defined linear counterparts.

The strength of a bilinear approach in the time frequency analysis can be appreciated considering the Margenau-Hill spectrogram distribution [81], a modified version of the original Margenau-Hill distribution [82]. This simple transform can be expressed as the real part of the product between two different STFT having different time window functions $h(t)$ and $g(t)$:

$$\mathrm{MHS}(t,\nu) = \Re\{(\mathrm{STFT}_h(t,\nu)\mathrm{STFT}_g(t,\nu)\}). \tag{4.13}$$

For practical purposes, the use of two different windows can improve the resolution with respect to the squared magnitude of the STFT, since the two windows can be independently chosen to adequately guarantee frequency and time resolution. The main drawback is however the possible generation of artifacts and distortions, arising when the window lengths are very different and when the signal contains components close in the time-frequency plane.

The prototype of quadratic time-frequency representation is the Wigner-Ville distribution (WV). It was first developed in the field of quantum mechanics by Wigner [83] and only later applied to signal analysis by Ville [84]. It is one of the most diffuse and powerful bilinear time-frequency representations. The starting point is a time dependent autocorrelation function chosen as

$$R(t,t') = s\left(t+\frac{t'}{2}\right)s^*\left(t-\frac{t'}{2}\right), \tag{4.14}$$

then the Wigner-Ville distribution is defined as the Fourier transform of this function, obtaining

$$\mathrm{WV}(t,\nu) = \int_{-\infty}^{+\infty} dt'\; s\left(t+\frac{t'}{2}\right)s^*\left(t-\frac{t'}{2}\right)e^{-i2\pi\nu t'}. \tag{4.15}$$

In equation 4.15 the complex conjugate of the signal is computed. If the signal is real, it is used in the form of analytic associate, i.e. imaginary component of the complex signal is obtained from the Hilbert transform of the real component s. The Wigner–Ville distribution can be thought of as a short-time Fourier transform where the windowing function is a time-scaled, time-reversed copy of the original signal.

The WV has a number of desirable properties for our purposes. First of all, the WV of any signal is always real and it satisfies the time and frequency

marginal conditions [77]

$$\begin{aligned} |s(t)|^2 &= \int_{-\infty}^{+\infty} d\nu \, \mathrm{WV}(t,\nu) \\ |S(\nu)|^2 &= \int_{-\infty}^{+\infty} dt \, \mathrm{WV}(t,\nu), \end{aligned} \tag{4.16}$$

where the integration of the distribution over the frequency gives the square modulus of the signal, and the integration over the time gives the energy spectrum. In general the WV is characterized by sharp time-frequency features that makes it one of the most exploited TFT in signal processing. However, a known drawback inherent in the formulation of the transform is the appearance of strong cross-term interference in the analysis of multicomponent signals [85]. The cross-term interference is manifested as oscillating features arising in the time-frequency plane halfway between each pairs of components, as an example see panel (a) of figure 4.5. Notice that to evaluate the Wigner-Ville distribution at a particular time it is necessary to add contributions built by the product of the signal at different times. The operation equals to theoretically fold the left part of the signal over the right part to check for the presence of any overlap. The WV weights far away times equally to near times, hence distribution is highly non local.

One of the possible approaches to overcome part of the cross-term interference signatures is to localize in time the transform by multiplying the integrand in equation 4.15 by a time window function $h(t)$. The pseudo-Wigner-Ville distribution (PWD) is obtained, defined as

$$\mathrm{PWV}(t,\nu) = \int_{-\infty}^{+\infty} dt' \, h(t') s\left(t + \frac{t'}{2}\right) s^*\left(t - \frac{t'}{2}\right) e^{-i2\pi\nu t'}. \tag{4.17}$$

As shown in figure 4.5 panel (b), asynchronous cross-term interference are greatly reduced at the cost of some time-frequency resolution in PWV. A second window function $g(t)$ is finally introduced in order to perform a smoothing in

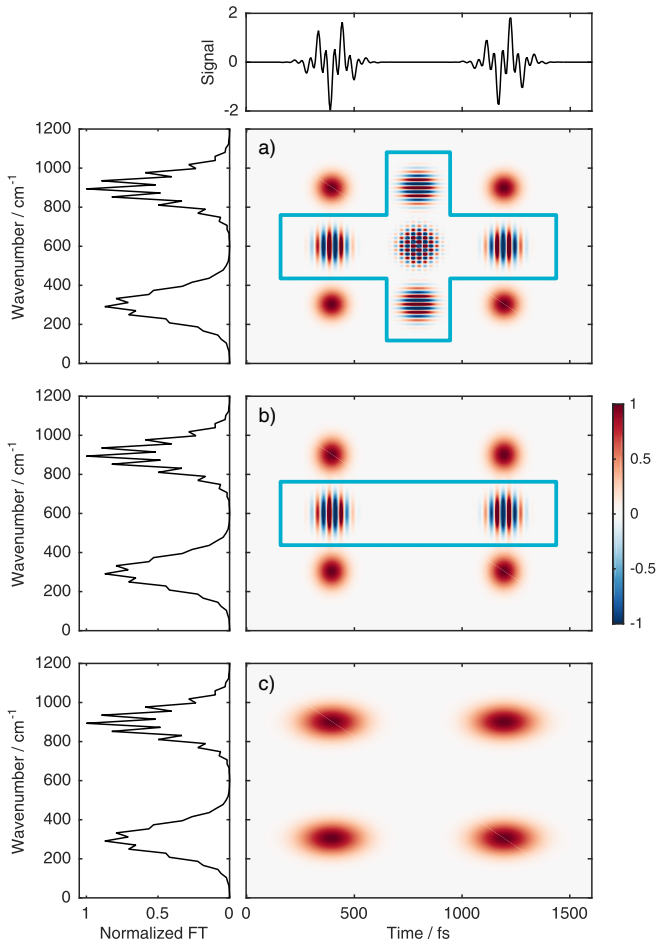

Figure 4.5: Comparison between (a) Wigner-Ville, (b) pseudo-Wigner-Ville and (c) smoothed-pseudo-Wigner-Ville distributions. The original signal in the frequency and time domain is shown for comparison on the left and on top of the panels, respectively. Cross-term interference artifacts appearing between relevant signals along time and frequency axes are highlighted by turquoise lines.

time, removing the residual interference between synchronous features, see figure 4.5 panel (c). The final transform is called smoothed pseudo-Wigner-Ville distribution (SPWV) [86] and it is defined as

$$\begin{aligned} \mathrm{SPWV}(t,\nu) = \int_{-\infty}^{+\infty} dt' \int_{-\infty}^{+\infty} dt''\, h(t')g(t''-t) \\ \times s\left(t''+\frac{t'}{2}\right) s^*\left(t''-\frac{t'}{2}\right) e^{-i2\pi\nu t'}. \end{aligned} \tag{4.18}$$

From the practical point of view, SPWV provides good results even in the presence of many components and when the time window are well tuned it contains little to none cross-term artifacts However, because of the two time windows, the resolution is even lower with respect to the original WV and PWV, moreover the fulfilment of the marginal conditions becomes less rigorous.

In addition to the Margeneau-Hill spectrogram and the Wigner-Ville distribution and its derivatives, the Choi-Williams (CW) distribution [87] represents one of the best-known transforms of the Cohen's class. The CW distribution is defined as:

$$\begin{aligned} \mathrm{CW}(t,\nu) = \int_{-\infty}^{+\infty} dt' \int_{-\infty}^{+\infty} dt'' \, \frac{\sqrt{\alpha}}{\sqrt{4\pi}|t''|} e^{-\frac{t'^2\alpha}{(4t''^2)}} \\ \times s\left(t+t'+\frac{t''}{2}\right) s^*\left(t+t'-\frac{t''}{2}\right) e^{-i2\pi\nu t'}, \end{aligned} \tag{4.19}$$

and it critically depends on the α parameter, introduced to solve the cross-term interference problem. When $\alpha \to \infty$ the WV distribution 4.15 is retrieved. The smaller the α parameter, the more effective is the reduction of the interference. Values of α too small may anyway lead to an overall degradation of the TFT map's content. A disadvantage of the CW distribution is that, although a good frequency resolution is obtained, it preserves strong interferences for synchronized components in time, manifested as deformations along the vertical axis. To overcome this limit, the same strategy used to obtain the SPVW from the WV

can be adopted and the integrand in equation 4.19 can be multiplied by two time windows g and h, obtaining the smoothed Choi-Williams (SCW):

$$\begin{aligned} \mathrm{SCW}(t,\nu) = \int_{-\infty}^{+\infty} dt' \int_{-\infty}^{+\infty} dt''\, h(t'')g(t') \frac{\sqrt{\alpha}}{\sqrt{4\pi}|t''|} e^{-\frac{t'^2\alpha}{(4t''^2)}} \\ \times s\left(t+t'+\frac{t''}{2}\right) s^*\left(t+t'-\frac{t''}{2}\right) e^{-i2\pi\nu t'}. \end{aligned} \tag{4.20}$$

4.2.4 Qualitative comparison

For better understanding the performances of the discussed TFTs when applied to spectroscopic signals, they have been applied to the analysis of a synthetic signal $y(t)$ constructed summing damped oscillations with different frequencies and amplitudes

$$\begin{aligned} y(t) &= \sum_{n=1}^{N} y_n(t) \\ &= \sum_{n=1}^{N} A_n e^{-\frac{t}{\tau_n}} e^{i2\pi\nu_n t}, \end{aligned} \tag{4.21}$$

where the n^{th}-component $y_n(t)$ is characterized by the scalar amplitude A_n, the damping time τ_n and the oscillation frequency ν_n. The signal is assumed to exist only for positive times. Moreover, the Fourier transform of the synthetic signal will be denoted with the capital letter, i.e. $Y(\nu)$ and $Y_n(\nu)$. The choice of focusing the attention on exponentially damped oscillatory signals is justified from the typically experimentally observed dephasing dynamics of the coherent state excited during the 2DES experiments [88, 16].

The benefit of using a synthetic signal with known properties is that it is possible to judge the performances of the different TFTs simply comparing their results with the original frequencies and amplitudes. This is of course not trivial with real experimental data. For now the discussion is limited to one-dimensional signals as described in equation 4.21, but the generalization

to complete 2DES signals is straightforward. The signals analyzed here can indeed be interpreted as single decay traces extracted at specific coordinates of the 2D maps.

There are several factors that may contribute to the final overall performances of a TFT analysis. (i) The nature of the input signal. Different TFTs may be more or less suitable towards the analysis of signals characterized by different frequencies and dynamics and may be more or less robust against noise. (ii) The choice of the function used to describe the g and h windows and (iii) the parameters on which these functions depend. The attempt to fully explore all the possible scenarios is not an easy task and goes beyond the scope of this analysis. We first limit the discussion to a single example, shown in figure 4.6, used to illustrate the different circumstances and artifacts that may typically appear during the analysis with the considered TFTs. In this example the values of the frequency and time parameters adopted to generate the signal have been chosen in order to mimic the values typically encountered in experiments. To obtain a meaningful comparison, a Gaussian function was chosen to represent g and h windows for all the analyzed TFTs. For each transform, the windows parameters have been chosen to provide a good overall match of the time-frequency representation with the originating signal.

Figure 4.6 clearly highlights the major advantages and drawbacks of the different approaches. For example, the frequency dependent resolution of CWT commented in section 4.2.2 is clearly recognizable in panel (b), where the higher frequency components of the signal are very poorly resolved. The scalogram ($|\mathrm{CWT}|^2$, panel b), the spectrogram, $|\mathrm{STFT}|^2$, panel (c) and the Margenau-Hill spectrogram MHS, panel (d) show similar deformations of the signals along the time dimension, manifested as aberrations close to the boundaries of the investigated time window, at $t \sim 0$ and $t \sim 1000$fs. The three frequency components seem indeed to reach a maximum amplitude at $t > 0$, instead that showing the expected exponentially decreasing behavior. This deviation may

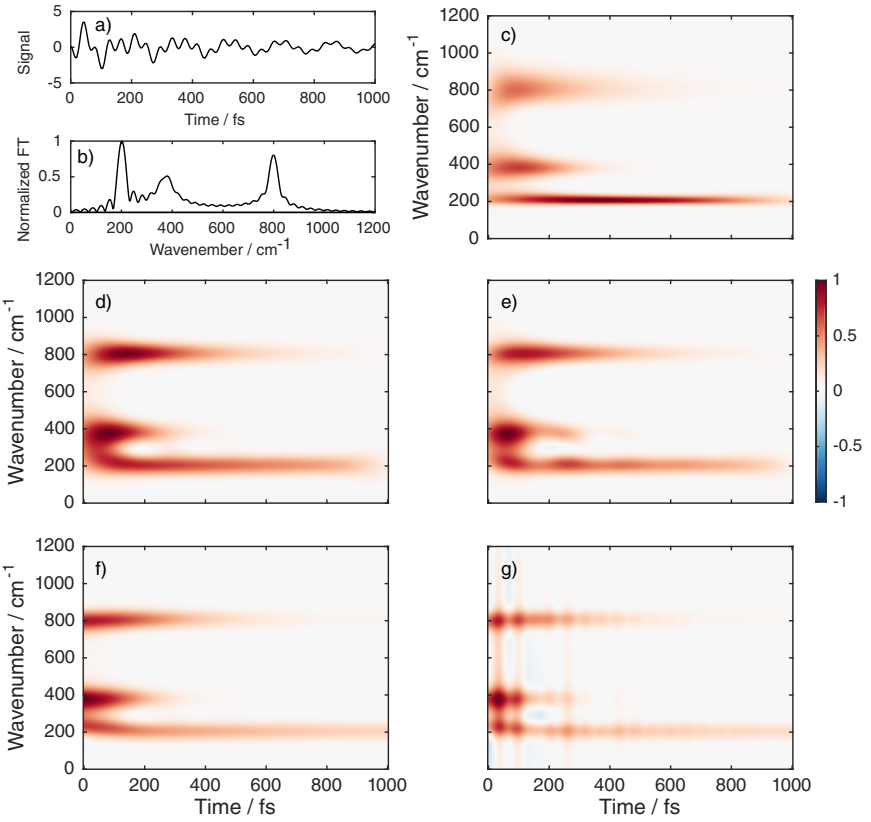

Figure 4.6: Comparison of the results obtained applying different TFTs to a multicomponent signal mimicking experimental data. Analyzed signal in the (a) time and (b) frequency domain, with parameters ν_1 = 200 cm^{-1}, ν_2 = 375 cm^{-1}, ν_3 = 800 cm^{-1}; τ_1 = 2 ps, τ_2 = 200 fs, τ_3 = 500 fs; $A_1 = 1$, $A_2 = 2$, $A_3 = 1.5$; (b) Scalogram ($|\mathrm{CWT}|^2$, ν_0 = 500 cm^{-1}, σ_h = 100 fs); (c) Spectrogram ($|\mathrm{STFT}|^2$, σ_h = 100 fs); (d) Margenau-Hill spectrogram (MHS, σ_h = 55 fs, σ_g = 150 fs); (e) Smoothed-pseudo-Wigner-Ville distribution (SPWV, $\sigma_h = \sigma_g$ = 75 fs); and (f) Smoothed Choi-Williams distribution (SCW, $\sigma_h = \sigma_g$ = 80 fs).

complicate the interpretation of the dynamics of real signals. The smoothed-pseudo-Wigner-Ville SPWV, panel (e), and the smoothed-Choi-Williams SCW, panel (f), are instead characterized by a good resolution and accuracy both along the time and the frequency axes. The SCW, despite the good resolution achieved, shows vertical artifacts typical of such approach.

The performances of the considered TFTs have been tested also for a wider range of signals. We have analyzed signals characterized by frequencies ν_n spanning the typical range of experimental oscillations recorded in ultrafast broadband 2D electronic spectroscopy (100-1500 cm^{-1}) and characterized by dephasing times τ_n much shorter and/or much longer than the maximum delay time of the recorded signals, in order to explore all the possible scenarios with respect to the FT frequency resolution. Except for the scalogram ($|CWT|^2$), which presents by definition a frequency-dependent resolution, the other transforms did not reveal particular differences in the performances when applied to different signals. A general behavior, common to all transforms, is the difficulty in analysing signals characterized by low frequencies and short dephasing times, with respect to the overall time range considered. In this situation only few periods of the oscillation are available and thus the uncertainty in the analysis may be high. Parametric methods can be adopted in this case, as shown in section 4.3.

Since experimental measures may be affected by large amount of noise, it is important to test how the transforms behave in the presence of various noise levels. The performances of the TFTs have been calculated for a series of signals defined as $y_{\text{noise}}(t) = y(t) + kn(t)$ where $n(t)$ is a source of gaussian noise and k is a scaling factor. The calculations have been done for $k = 0$, 1, 0.2, 0.5 and 1. Figure 4.7 shows the results obtained starting from the same signal $y(t)$ used in figure 4.7 with $k = 0.5$. The noise degrades the results of all transforms with about the same efficiency; as the level of noise increases, the number of artifacts along the frequency dimension increases giving rise to

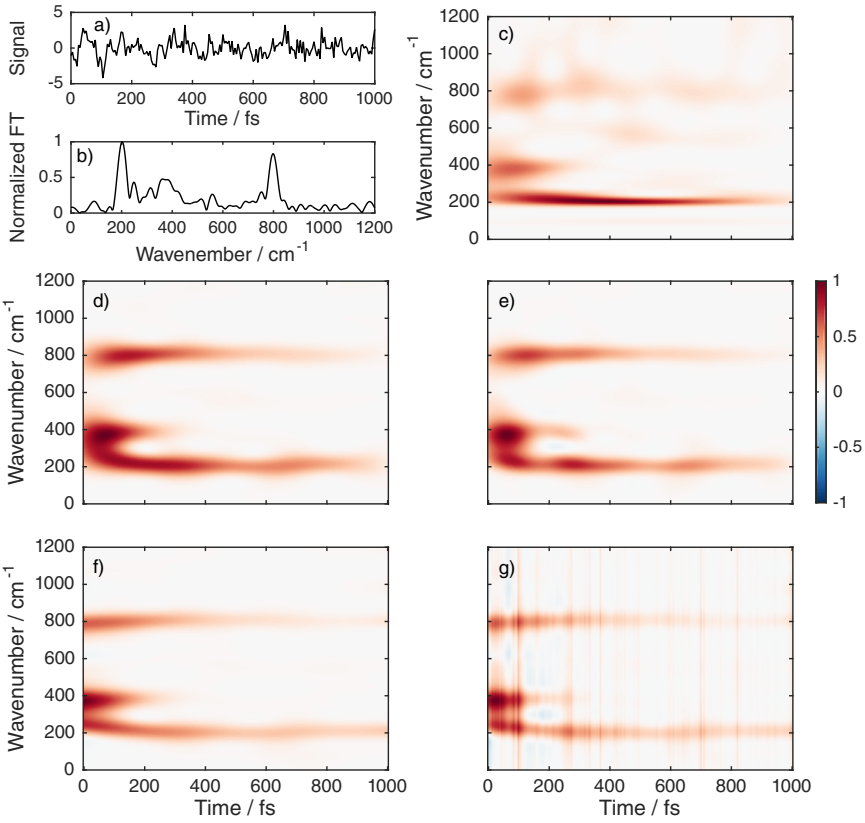

Figure 4.7: Effect of the noise on TFT performances. (a) Analyzed signal in the time and frequency domain. In this specific case: $\nu_1 = 200\text{cm}^{-1}$; $\nu_2 = 375\text{cm}^{-1}$; $\nu_3 = 800\text{cm}^{-1}$; $t_1 = 2$ ps; $t_2 = 200$ fs; $t_3 = 500$ fs; noise level $k = 0.5$. (b) Scalogram ($|\text{CWT}|^2$); (c) Spectrogram ($|\text{STFT}|^2$); (d) Margenau-Hill spectrogram (MHS); (e) Smoothed-pseudo-Wigner-Ville (SPWV); and (f) Smoothed Choi-Williams (SCW). Window parameters as in figure 4.6.

spurious signals especially at early times. In general the MHS (panel d) and the CW (panel f) seem to be less robust against noise, especially if compared with SPWV (panel e), which performs quite well even in the presence of relatively high levels of noise.

To illustrate how the choice of the window function may affect the results of the TFT analysis, we repeated the calculations using several window shapes commonly used in time-frequency analysis. The results obtained for the STFT are reported in figure 4.8. Apart for the rectangular function generating the expected ringing artifacts, in panel (b), all the considered functions lead to similar results. Given this weak dependence on the window functions, Gaussians are often chosen for simplicity [89].

While the shape of the window function has little effects on the performances of the TFTs, the choice of the window parameters is instead crucial to satisfactorily retrieve both time and frequency information. For example, for a Gaussian window $h(t)$ in a STFT, the parameter σ_h is crucial to select the right balance between time and frequency resolution. Each transform responds in a different way to the variation of the windows parameters, as expected considering their different mathematical definitions. General trends are difficult to identify, being the final result also dependent on the analyzed signal. In general it is observed that windows characterized by smaller width in time guarantee better time resolution but frequency information is degraded. The parameters must thus be carefully chosen to obtain a good compromise between frequency and time resolution. The choice is necessarily application-dependent and depends on the information one wants to retrieve.

4.2.5 Optimization and selection

A good signal processing procedure based on time-frequency methods requires the choice of the best TFT and the optimization of its parameters, based on the properties of the experimental signal to analyze. Given the differences in

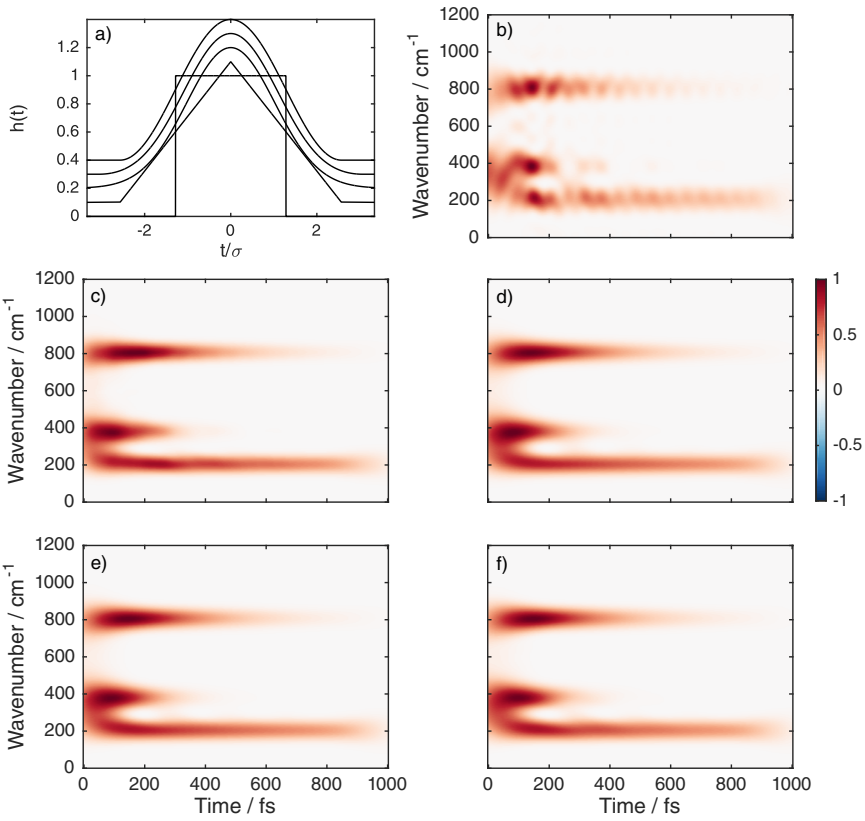

Figure 4.8: (a) Window functions tested in the TFT analysis. From the bottom to the top: top-hat, Bartlett, Gaussian, Blackman, and Hanning function. The windows width have been chosen in order to normalize the area. (b-f) Results obtained applying the Short Time Fourier Transform (STFT) for the analysis of the signal of figure 4.6 using (b) the rectangular window function; (c) the Bartlett window function; (d) the Gaussian window function; (e) the Blackman window function, and (f) the Hanning window function.

the definitions and in the parameters on which they depend, a meaningful quantitative comparison of different TFTs requires a preliminary step of optimization of the associated window parameters. A different choice of windows (or wavelets) leads indeed to significantly different results. To select the best TFT in a non-arbitrary way the following procedure has been set up:

(i) generation of a synthetic signal with known frequency and time properties. Working with a signal with known information content will help in the evaluation of the performances of different transforms as well as in the identification of possible artifacts arising during the analysis. This is of course not possible with complex experimental signals where the information is in general unknown and need to be extracted;

(ii) definition of a fitness parameter describing how well the results of the transforms match the original signal;

(iii) optimization of the windows and wavelets parameters based on the minimization of the previously defined fitness parameter;

(iv) application of the TFTs with optimized windows parameters and comparison of their results.

For simplicity, following the common procedure in the literature, Gaussian windows are considered in all the transforms and their widths are the parameters to be optimized. Similarly, for $|\mathrm{CWT}|^2$ a complex Morlet wavelet is used. The choice of a Gaussian shape is not accidental: it represents indeed the optimal joint time-frequency resolution from the uncertainty point of view and the balance between time and frequency resolution can be controlled by the width parameter. The main reason to introduce an optimization procedure is the necessity of comparing the TFTs with the parameters that guarantee the best performance on a specific signal. If arbitrary windows and wavelet parameters

are chosen, a quantitative comparison of the performances of the TFTs would not be meaningful.

First of all, in order to emulate the typical oscillating features appearing in 2DES data a four component signal described by equation 4.21 has been considered. The values of the parameters defining the signal have been chosen in order to mimic the values typically encountered in experiments and in order to have an adequate signal for the subsequent optimization procedure. The desirable properties of the signal are: a wide enough distribution of frequencies and damping times, probing different regimes of decoherence, and an equal contribution to the total signal for the different components. We want that each component of the signal counts equally in the optimization step. In other words, if one component of the signal is predominant, the optimization procedure will drive the TFTs to best perform for the specific characteristic of the dominant component, i.e. specific frequency and damping time. Instead, we want to keep the discussion and the procedure as general as possible. The parameters are chosen as follows

$$\begin{aligned}
&\nu_1 = 200\text{cm}^{-1} && \tau_1 = 300\text{fs} && A_1 = 1/\sqrt{\tau_1} \\
&\nu_2 = 500\text{cm}^{-1} && \tau_2 = 1000\text{fs} && A_2 = 1/\sqrt{\tau_2} \\
&\nu_3 = 800\text{cm}^{-1} && \tau_3 = 500\text{fs} && A_3 = 1/\sqrt{\tau_3} \\
&\nu_4 = 1100\text{cm}^{-1} && \tau_4 = 150\text{fs} && A_4 = 1/\sqrt{\tau_4}.
\end{aligned} \tag{4.22}$$

The amplitudes are defined as $A_n = 1/\sqrt{\tau_n}$ in order to guarantee that the total energy of each component is the same, i.e. neglecting overlaps, each component has a peak with the same area in the power spectrum. Indeed, it is possible to demonstrate that for each $y_n(t)$ the total integral of the power spectrum is equal to the total integral of the square of the signal and it is a constant

$$\int_{-\infty}^{+\infty} d\nu \; |Y_n(\nu)|^2 = \int_{-\infty}^{+\infty} dt \; \left|y_n(t)\right|^2 = A_n^2 \frac{\tau_n}{2} = \frac{1}{2}, \tag{4.23}$$

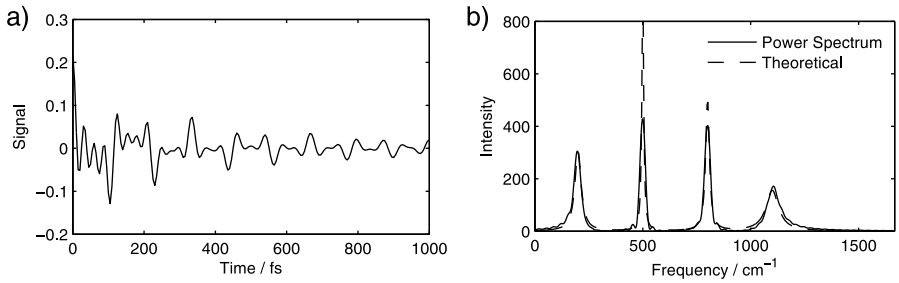

Figure 4.9: (a) Signal and (b) power spectrum obtained from parameters in 4.22. The theoretical power spectrum has been calculated using equation 4.24. The difference in the maximum intensity of the peaks is due to the limited time window spanned from the signal which is not sufficient to allow the complete decay of all the oscillating components. The non-complete decay of coherences is a feature typically encountered in experimental signals.

where the power spectrum and the square of $y_n(t)$ are calculated as

$$\begin{aligned} |Y_n(\nu)|^2 &= A_n^2 \frac{1}{4\pi^2(\nu-\nu_n)^2+\tau_n^{-2}} \\ \left|y_n(t)\right|^2 &= A_n^2 e^{-2\frac{t}{\tau_n}}. \end{aligned} \tag{4.24}$$

It is useful to stress the fact that the signal $y(t)$, defined by equation 4.21, is assumed to exist only for positive times. The resulting signal and its power spectrum are shown in figure 4.9. It has been calculated in the interval $0 \leq t \leq 1000$ fs with 5 fs time step, which are typical values for ultrafast experiments.

In order to define a meaningful fitness parameter, a theoretical bilinear time-frequency representation THEO is introduced. This function is specifically tailored for exponentially damped signals. The most important property imposed in the definition of this distribution is the fulfillment of the marginal

conditions as in equation 4.16. The function THEO is defined as

$$\begin{aligned} \mathrm{THEO}(t,\nu) &= \sum_{n=1}^{N} \frac{|Y_n(\nu)|^2 \left|y_n(t)\right|^2}{A_n^2 \frac{\tau_n}{2}} \\ &= \sum_{n=1}^{N} A_n^2 \frac{2}{\tau_n} \frac{1}{4\pi^2(\nu-\nu_n)^2 + \tau_n^{-2}} e^{-2\frac{t}{\tau_n}} \end{aligned} \tag{4.25}$$

note that this equation incorporates the analytical expressions reported in equation 4.24. The marginal properties are rigorously respected for a signal with $N = 1$ and they are still satisfactorily valid if the components of the signal do not strongly overlap in the time-frequency plane, as in our case. For each component n it is possible to demonstrate that

$$\begin{aligned} \int_{-\infty}^{+\infty} dt\, \mathrm{THEO}(t,\nu) &= |Y_n(\nu)|^2 \\ \int_{-\infty}^{+\infty} d\nu\, \mathrm{THEO}(t,\nu) &= \left|y_n(t)\right|^2 \\ \int_{-\infty}^{+\infty} dt \int_{-\infty}^{+\infty} d\nu\, \mathrm{THEO}(t,\nu) &= A_n^2 \frac{\tau_n}{2}, \end{aligned} \tag{4.26}$$

which implies that the total energy of the signal is conserved when distributed on the time-frequency plane trough the function THEO. The idea behind this definition of the theoretical time-frequency distribution is very simple; a Lorentzian shape is used for the frequency profile of the features and an exponential decay is used for the time profile. A factor $2A_n^{-2}\tau_n^{-1}$ is introduced in order to guarantee the conservation of the energy. This theoretical time-frequency transform represents the hypothetical limit for any time-frequency transform: it is characterized by the highest possible frequency resolution of the Fourier transform and the perfect time evolution of the originating signal without the presence of any cross-term interference. The function THEO is the limit that each TFT must aspire to reproduce as close as possible. It is thus natural to define the fitness parameter as the norm of the difference between

THEO and a generic TFT.

An unconstrained minimization problem over the set of parameters $\mathbf{p} = (p_1, p_2, ..., p_M)$ that characterize each investigated TFT can be solved

$$\min_{\mathbf{p} \in \mathbb{R}^M} \quad \left|\left|\mathrm{THEO}(t,\nu) - \mathrm{TFT}(t,\nu;\mathbf{p})\right|\right|^2. \tag{4.27}$$

The minimum of the problem represents the TFT realization that gives the minimum difference with respect to the theoretical transform, and thus delivers the best performance. A scale factor has been inserted in the array of parameters $\mathbf{p}$ to assure that the best matching condition is not affected by differences in the normalization of the time-frequency representation. This is particularly relevant in the case of $|\mathrm{CWT}|^2$ where the stretching of the wavelet is not able to guarantee the marginal properties. For example, in the case of SPWV, the expression inserted in the minimization problem 4.27 is

$$\mathrm{TFT}(t,\nu;\mathbf{p}) = p_1 \mathrm{SPWV}(t,\nu;p_2,p_3), \tag{4.28}$$

where p_1 is the scale factor, $p_2 = \sigma_h$ and $p_3 = \sigma_g$ are width parameters of the window functions. It is important to highlight that, in the minimization procedure, not only the auto-terms are optimized for the best match with the theoretical representation, but also the interference terms are reduced. The function THEO does not contain any interference by definition, thus every interference contribution in the TFT increases the norm in the minimization problem. The final solution of the problem will be a compromise between interference suppression and sharpening of the features. For sake of completeness, three widely used time-frequency representations have been added to the comparison in addition to the ones already described in the previous sections: the Zhao-Athlas-Marks distribution ZAM [78], the Born-Jordan distribution BJ [85] and the Butterworth distribution BUD [90].

Figure 4.10 reports the output of the minimization problem for all the

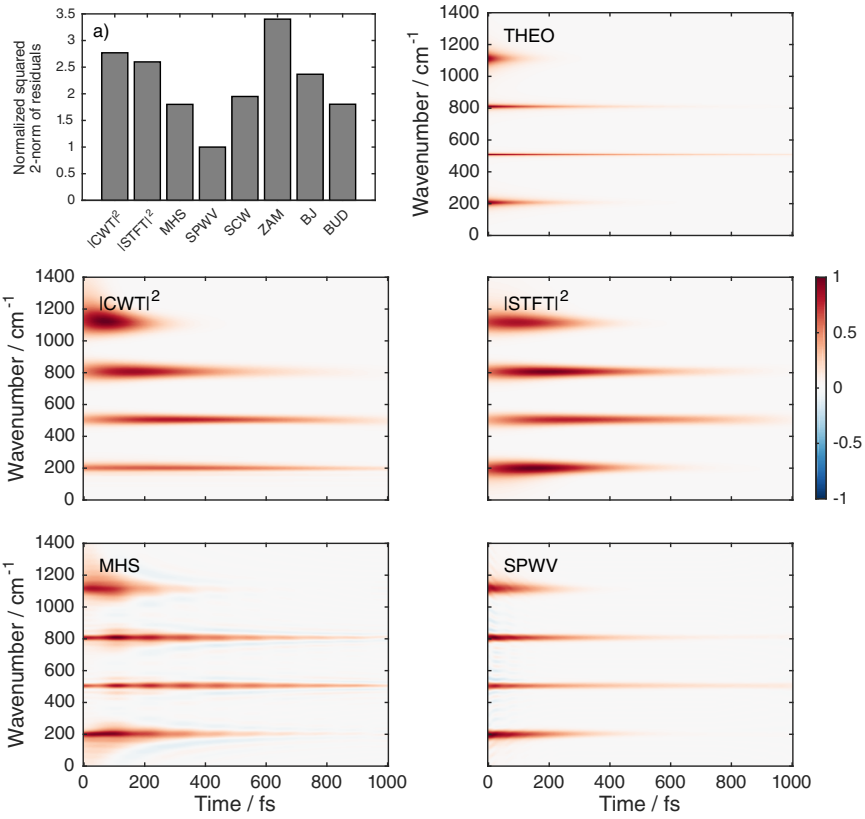

Figure 4.10: (a) Histogram of the norm of the residuals for all the TFTs after the optimization step. (other panels) Optimized TFTs considered in the comparison.

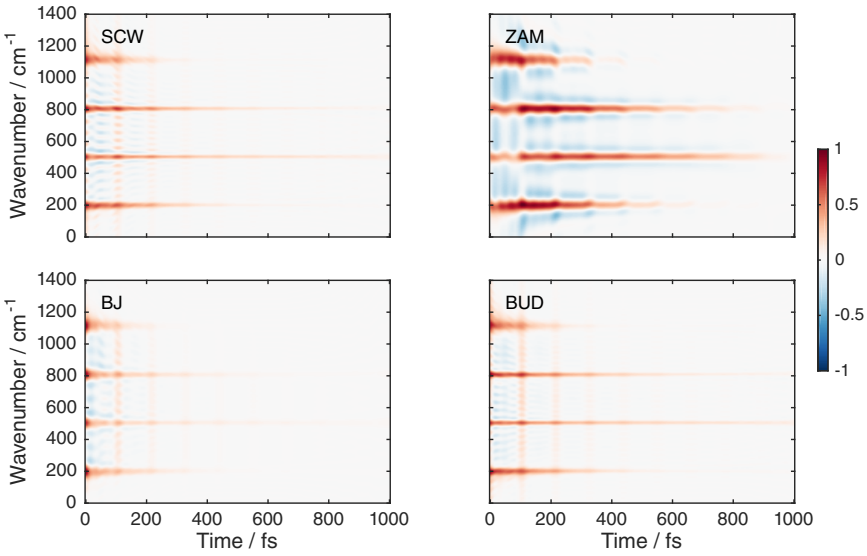

Figure 4.11: (continuation of figure 4.10) Optimized TFTs considered in the comparison.

considered TFTs. Looking at the histogram in panel (a), it emerges that the SPWV distribution is the TFT that gurantee the best matching with the theoretical one. As can be deduced from figures 4.10 and 4.11, in the optimized SPWV the cross-term interference is mostly eliminated maintaining at the same time an high time-frequency resolution. What was already predicted from the qualitative comparison is confirmed after the numerical optimization step. We can conclude that the smoothed-pseudo-Wigner-Ville distribution, over all the considered TFTs, is the most suited transform in the analysis of sum of exponentially damped signals with frequency and damping time typically encountered in ultrafast optical experiments.

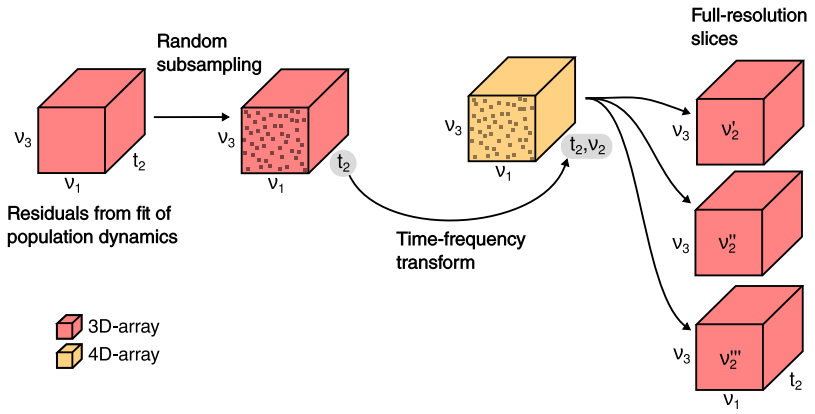

Figure 4.12: Schematic representation of the time-frequency analysis of a 2DES dataset. The residuals from the fit of the population dynamics are random subsampled in the (ν_1, ν_3) dimensions and time-frequency transformed along the t_2 axis to obtain a 4D-array of data. Full-resolution slices of the 4D-array are computed for selected values of ν_2.

4.2.6 Application to 2DES data

A 2DES dataset can be imagined as a collection of decays trajectories of the third order signal along the population time. Each trajectory is extracted at a certain (ν_1, ν_3) coordinate of the 2D map. For each one of these 1D trajectories, the application of the TFT analysis generates a 2D time-frequency representation. Therefore, the composition of all the 2D time-frequency representations gives a 4D-array of data which is a function of ν_1, t_2, ν_2 and ν_3. A schematic representation of the analysis is reported in figure 4.12.

In order to visualize and investigate the content of this huge amount of data it is convenient to slice the 4D-array along specific dimensions. The most useful way is slicing the data along the ν_2 axis at a certain frequency, which is known to be relevant. A 3D-array of data is obtained with the same size and axis

labels of the originating residues data, i.e. the signal is reported as function of ν_1, t_2 and ν_3. This 3D-array not only provides the same information contained in the classic Fourier maps, i.e. at which positions in the 2D spectrum that specific frequency contributes more, but also it gives details of the dynamics of the coherence. Indeed, it is possible to follow the evolution of the FT map along the population time t_2. Indeed the dephasing of the coherence appears as a decay of the map as t_2 evolves.

In complex systems where more than one process can generate a coherence at a certain frequency with multiple dephasing times, it is not possible to disentangle the different contributions with a simple Fourier analysis. This because FT discards the dynamical information. Instead, looking at the 4D time-frequency transform we can monitor different portions of the map decaying with different rates highlighting the presence of separate processes.

There are several computational challenges in the computation of the 4D-array containing the time-frequency information. First of all, there is the necessity of dealing with big amount of memory to handle the huge amount of data. Moreover, the computational time can be high especially if we opt to use a bilinear transform like SPWV, which is much more demanding than STFT end CWT. With a modern desktop computer this is a possible, although intensive, task. Nevertheless cleaver ways to slim down the computation can be implemented. A downsampling of the ν_1 and ν_3 axes can be operated. A simple procedure is to random sample the 2DES maps, retaining only a small portion of the coordinates. The 2DES data of systems with broad lineshapes can be strongly downsampled without degrading substantially the information content [91]. The reduced collection of decay trajectories is then time-frequency transformed in a fraction of the time necessary for the complete computation. Some relevant values of the ν_2 axis are selected and only for those, the full resolution 3D-slices are reconstructed using specialized algorithm for in-painting of missing values, for example using a fast and reliable algorithm as described in

[92]. With this procedure memory usage and computation time are optimized.

The systematic study described in the previous sections, on the possible artifacts and interferences possibly arising in the different TFTs, turned out to be extremely useful when investigating 3D-slices of a full 2DES dataset. Indeed, the selection of a single frequency on the ν_2 axis limits our control of the outcome of the time-frequency transform. It is not possible to distinguish easily what is artifact and what is real dynamics unless we are sure about the possible outcome of the transform. Furthermore it is of pivotal importance to use the best performing TFT with optimal parameters in order to minimize the artifacts from the beginning.

If we are interested not in the full 3D slice, but only in an average damping time, it is possible to integrate along ν_1 and ν_3 axes obtaining a single decay trace that represents the average behavior of the time evolution of the Fourier map. The averaging as the benefit of smooth out the cross-term artifacts to some extent. Alternatively, it is possible to operate on the population time t_2 and obtain a value of damping time for each coordinate of the 2DES map. Assuming an exponential model for the dephasing of the coherences we can use the function $s(t_2)$ to model the evolution of the Fourier map as

$$s(t_2) = Ae^{-\frac{t_2}{\tau}}, \tag{4.29}$$

where A is the amplitude and τ is the dephasing time. We can evaluate the logarithm of $s(t_2)$ obtaining a linear function

$$\ln(s(t_2)) = \ln(Ae^{-\frac{t_2}{\tau}}) = \ln(A) - \frac{t_2}{\tau}, \tag{4.30}$$

and then evaluate numerically τ as the slope of this line. Finite time step Δt_2 can be used to calculate the average τ at different values of t_2 as

$$\tau = \frac{\ln(s(t_2)) - \ln(s(t_2 + \Delta t_2))}{\Delta t_2}. \tag{4.31}$$

Repeating this calculation for each coordinate of the 2DES map we get a damping-time-map $\tau(\nu_1, \nu_3)$, which shows the dependence of the damping time of the investigated coherence as a function of emission and excitation frequencies. This kind of analysis of the signal could be useful when investigating complex systems in which a distribution of damping times is expected.

4.3 Global analysis [93]

The global procedure proposed in this section goes beyond the main issues of the standard analyses presented in section 4.1 and it allows extracting all information from a complete 2DES dataset, analyzing simultaneously non-oscillating and oscillating components, without any preliminary subtraction operation. This is particularly relevant when fast decays and strongly damped low-frequency beatings cannot be easily disentangled with FT methods. Using the most general approach, both population and coherence contributions can be described with a complex exponential function: in the former case, the imaginary part of the complex function is zero and the real part carries all the information on the decay constants. In the latter case, real and imaginary part are nonzero and the function accounts for amplitude, dephasing rate, frequency and phase of oscillation.

The algorithm proposed here consists in a single robust fitting procedure that can simultaneously investigate both rephasing and non-rephasing signals. The validity of this method has been tested through the analysis of experimental 2DES data collected at room temperature for a standard dye, Zinc(II) phthalocyanine (ZnPc) in tetrahydrofuran (THF).

4.3.1 The fitting model

Mathematically, 2DES datasets can be described as three dimensional complex valued arrays X_{ijk} in which the third order optical signal is collected as a

function of excitation frequency, emission frequency and population time. The signal is visualized as a series of maps with (i, j) frequency indexes at the k-th population time. Hereafter the population time t_2 will be simply labeled t with the index k indicating different sampled values.

A simple and general model able to reproduce the oscillating and non-oscillating dynamics of a time-evolving signal is a sum of N independently decaying complex exponential functions. This model is applied to the study of the evolution of the 2DES signal during the population time. Such a superposition of independent decays is often called parallel model [55]. The decomposition of a signal in terms of damped complex exponential functions also recalls the Prony analysis method [94, 95, 96].

The n-th exponential component is expressed as $c_{nk} = a_n e^{b_n t_k}$. The complex parameter $a_n = |a_n| e^{i\phi_n}$ embeds the phase ϕ_n and amplitude $|a_n|$ information, while the exponential parameter b_n includes decay and frequency properties. In a more explicit form, each exponential component can be rewritten as $c_{nk} = |a_n| e^{i\phi_n} e^{-t_k/\tau_n} e^{i\omega_n t_k}$, where the decay constant is the negative inverse of the real part of the exponential parameter, $\tau_n = -1/\Re\{b_n\}$, and the angular velocity of the oscillation is the imaginary part, $\omega_n = \Im\{b_n\}$.

In order to ease the formulation of the fitting problem, the dataset dimensionality is reduced. The 3D-arrays are converted into 2D ones using a collective index h which includes all the possible excitation and emission frequency coordinates, $X_{ijk} \rightarrow Y_{kh}$. Each column of the newly defined $\mathbf{Y}$ matrix represents the decay of the signal at a specific coordinate of the 2DES map. The total number of frequency coordinates is H and the total number of sampled times is K, so that for the running indexes applies that $1 \leq h \leq H$ and $1 \leq k \leq K$. Moreover, the dataset structure Y_{kh} resembles the one of pump-probe data, thus allowing the application of well established analysis and fitting tools [55, 97]. In this section a global fitting procedure based on the variable projection algorithm [98, 99, 100] is developed following an established method for time-resolved

spectra analysis [101, 102].

Each complex exponential parameter b_n of the n-th component is shared between all the frequency coordinates of the maps. All b_n parameters are arranged in a row vector **b**. The complex amplitudes are conversely resolved in the two frequency dimensions and are arranged in a matrix with elements A_{nh}. Recalling the transformation $\mathbf{X} \rightarrow \mathbf{Y}$, each row of **A** represents a map of the amplitude of the n-th component. The multi-exponential model is written as

$$M_{kh} = \sum_{n=1}^{N} e^{t_k b_n} A_{nh}. \tag{4.32}$$

This model can be recast in a more compact form in matrix notation as $\mathbf{M} = \mathbf{EA}$, where the matrix **E** has elements $E_{nk} = e^{b_n t_k}$, i.e. each column contains a complex exponential function with unitary amplitude. Note that **E** is function only of **b**. The total number of parameters $P = N(1 + H)$ of the model can be partitioned in two groups: a small set of N exponential factors and a larger group of $N \times H$ complex amplitudes. We can organize all P parameters of the model in an array **z** of P elements in order to express the model function as $\mathbf{M}(\mathbf{z}) : \mathbb{C}^P \rightarrow \mathbb{C}^{K \times H}$.

4.3.2 The variable projection algorithm

The problem of finding the best **z** that fits the experimental data **Y** can be written in term of the following unconstrained minimization of the least squares of the residuals

$$\min_{\mathbf{z} \in \mathbb{C}^P} \|\mathbf{Y} - \mathbf{M}(\mathbf{z})\|^2. \tag{4.33}$$

For a typical 2DES dataset the number of parameters is very large and finding the optimal set which satisfies problem in equation 4.33 is nearly impossible. For example, for a model with $N = 10$ components to fit maps with a resolution

of 256×256 pixels, the total number of parameters is $P = 10(1 + 256^2) = 655370$. In order to tackle this major limitation, the mathematical structure of the function $\mathbf{M}(\mathbf{z})$ can be exploited. In particular, the partitioning of the parameters in linear A_{nh} and nonlinear b_n allows the minimization problem to be separable [102]. One can recognize that the subproblem of minimization

$$\min_{\mathbf{A}\in\mathbb{C}^{H\times K}} \|\mathbf{Y} - \mathbf{M}(\mathbf{A}, \mathbf{b})\|^2 \tag{4.34}$$

is easy to solve for fixed $\mathbf{b}$. Given $\mathbf{E}$ of full rank, i.e. there is no linear relationship between the columns of $\mathbf{E}$, the subproblem can be solved analytically as $\mathbf{A} = \mathbf{E}^+\mathbf{Y}$, where $\mathbf{E}^+$ is the Moore-Penrose pseudo inverse [103]. In this way the optimization procedure can operate only on the nonlinear b_n parameters and all the linear A_{nh} parameters are analytically computed at each iteration of the minimization algorithm. In other words, for a given set of exponential factors $\mathbf{b}$, the best possible amplitude maps able to fit the experimental data are immediately determined and easily accessible.

Given the solution of problem in equation 4.34, the separable optimization problem can be formulated in the reduced space of $\mathbf{b}$ alone as

$$\min_{\mathbf{b}\in\mathbb{C}^N} \|\left(\mathbf{I} - \mathbf{E}(\mathbf{b})\mathbf{E}(\mathbf{b})^+\right)\mathbf{Y}\|^2, \tag{4.35}$$

where $\mathbf{I}$ is the identity matrix of size $K \times K$. The objective function of this minimization problem is called the variable projection functional and $\mathbf{I} - \mathbf{E}(\mathbf{b})\mathbf{E}(\mathbf{b})^+$ is the projector on the orthogonal complement of the column space of $\mathbf{E}$ [102].

The elimination of the set of linear amplitudes parameters from the minimization problem has several benefits. The computation of matrix $\mathbf{A}$ and its initial guess are not necessary, therefore only the complex array $\mathbf{b}$ has to be estimated. Moreover, the number of iterations is drastically reduced with respect to the minimization in the complete space of parameters. The minimization of the variable projection functional is efficient and, more importantly, it has

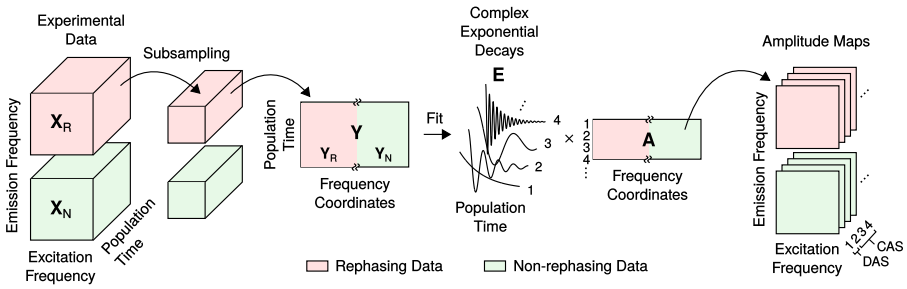

Figure 4.13: Schematic illustration of the fitting method. Rephasing and non-rephasing data ($\mathbf{X}_R$ and $\mathbf{X}_N$) are subsampled and reshaped into the matrix $\mathbf{Y}$, to which the global fitting procedure is applied. Decay constants, frequencies and matrix $\mathbf{A}$ are then recovered. Rephasing and non-rephasing amplitude maps are obtained from matrix $\mathbf{A}$ for each complex exponential decay component. Two types of maps can be identified: decay-associated spectra (DAS) and coherence-associated spectra (CAS). Reproduced from ref. [93].

higher probability of finding the global minimum solution instead of a local one [100].

4.3.3 Application to 2DES data

In the specific case of 2DES data analysis, the fitting procedure here reported allows for a convenient global fitting of rephasing and non-rephasing data simultaneously. This can be particularly important in the investigation of the nature (electronic or vibrational) of the coherences excited during the experiments, since electronic and vibrational coherences typically manifest completely different behaviors in rephasing and non-rephasing parts of the signal [28]. To this purpose, the data matrix is built appending blocks of columns relative to the two experiments

$$\mathbf{Y} = [\,\mathbf{Y}_R, \mathbf{Y}_N\,], \tag{4.36}$$

where $\mathbf{Y}_R$ and $\mathbf{Y}_N$ are the rephasing and non-rephasing data, respectively. The model described above is then applied to the final matrix $\mathbf{Y}$. As summarized in the scheme reported in figure 4.13, at the end of the fitting procedure, each row of the matrix $\mathbf{A}$ contains the two amplitude maps associated with a complex exponential decay component, one for the rephasing and one for the non-rephasing data. Each pair of complex amplitude maps is associated with a damping time and a frequency.

The minimization over two complete rephasing and non-rephasing datasets is computationally intense. In order to lighten the amount of computations involved in each step of the minimization procedure, the data are subsampled in the frequency dimensions. We implemented a simple subsampling algorithm based on the construction of an evenly spaced grid over the 2D maps. The degree of subsampling is controlled by the dimension of the grid step g. The features recorded in typical 2DES maps are usually broad and the information about the evolution of the complete signal is captured using a reasonably small number of points of the map [91]. For the experimental example reported below, we observed that, even retaining less than 5% of the frequency coordinates, the output of the fit is conserved. After the convergence of the minimization problem using the sub-sampled data, the amplitude maps with full resolution are recovered using the solution of the minimization problem equation 4.34 on the complete dataset. The entire procedure on a subsampled dataset takes tens of seconds to converge on a standard computer.

A set of generally reasonable constraints can be implemented in order to reduce the parameter space to be explored. The exponential components are divided into two sets, the decay-set and the coherence-set, each with different boundaries. The former set models the non-oscillating dynamics of the data and it has frequencies fixed at 0 cm^{-1} and no boundaries are applied to the time

constants. The latter set models the oscillating dynamics. Absolute values of frequencies of these components are taken smaller than the Nyquist frequency associated with the sampling over the population time. Damping times are forced to be positive. A coherence associated with a specific process appears with both positive and negative frequencies in complex rephasing and non-rephasing signals [59]; to further reduce the dimensionality of the minimization problem, it is thus possible to consider pairs of oscillating components with the same damping time and with the same frequency but opposite sign. Amplitude maps can be classified according to the set to which they are associated. Maps associated with the decay-set are called decay-associated spectra (DAS), in analogy with the definition previously proposed in similar methods [104], whereas maps associated to the coherence-set are called coherence-associated spectra (CAS), see figure 4.13. Although the definition of DAS and CAS proposed above has been based on the assumption of a set of boundaries, this distinction emerges naturally directly from the unconstrained minimization problem. However, the *a priori* definition of suitable boundaries prevents solutions with CAS associated to a negative dephasing time and CAS with frequency higher than the Nyquist limit.

To assess if the model is satisfactorily reproducing the experimental data is not an easy task when dealing with multidimensional datasets. Moreover, the use of too many components when working with multi-exponential fits is a well-known issue [105]. In this context, the singular value decomposition (SVD) is an useful tool to investigate the data in a reduced space [55, 106, 107]. For example, an estimate of the necessary number of components to be included in the fitting model can be obtained as the number of principal values in the singular spectrum of the matrix $\mathbf{Y}$. Moreover the SVD of the residues matrix is helpful to check if the model is capturing all the dynamical features of the data [55]. A second test to assess if the correct number of parameters has been chosen consists in the calculation of the correlation matrix of fitted parameters

[108]. The inspection of this matrix allows establishing the possible presence of interdependence between couples of parameters, in which case the number of parameters must be reduced.

4.3.4 Experimental results

2DES experiment was performed at room temperature on a commercial (Sigma Aldrich®) Zn (II) phthalocyanine dissolved in spectroscopic grade THF (optical density was 0.25 with a pathlength of 1 mm). This dye is used as standard to validate the procedure and to discuss the advantages of the proposed methodology with respect to the currently employed analysis procedures. The experiment was conducted using a laser spectrum centered at 680 nm with a time duration of about 10 fs.

As shown in figure 4.14(a) the laser spectrum is tuned to cover the electronic transition to the first excited state of ZnPc. Time-resolved fluorescence measurements ascertained for this state a lifetime in the nanoseconds timescale, confirming that no relaxation of the excited state population should be recorded in the ultrafast regime investigated here [109, 110]. The vibrational properties of the molecule have been characterized by resonant Raman spectroscopy and the relative Raman spectrum is shown in figure 4.14(b). The laser bandwidth used in the 2D experiment can excite simultaneously all the vibrational states within 1000 cm^{-1} on both red and blue sides of the maximum of the absorption spectrum (14580 cm^{-1}), as highlighted in figure 4.14(c).

We describe the molecular system in the framework of the displaced harmonic oscillator model (DHO), with the ground and the first excited states having the same vibrational potential energy surface displaced along the mode coordinate. The system consists in a set of independent oscillators associated to the modes coupled to the electronic transition. Within this model the vibrational properties of ground state and excited state are identical, i.e. frequencies and damping times of vibrational coherences are indistinguishable. As already

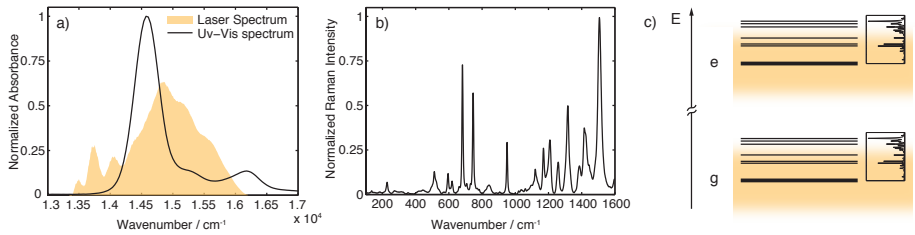

Figure 4.14: (a) Normalized absorption spectrum of ZnPc in THF (black line) and laser spectrum (yellow area). (b) Raman spectrum of ZnPc powders with 633 nm excitation wavelength. (c) Energy levels diagram for ZnPc. Reproduced from ref. [93].

discussed, this assumption, physically meaningful for many systems, simplifies considerably the dimensions of the minimization problem. However, the fitting model can be easily generalized including more components distinguishing between ground state and excited state coherences.

The photophysical data obtained from the preliminary time-resolved and Raman characterization have been used for a first estimate of the number and values of the fitting parameters. The fitting algorithm takes tens of seconds to fit a dataset of 256×256 rephasing and non-rephasing maps subsampled with 8 points grid step on a regular laptop computer. The outcoming parameters are listed in table 4.1.

Rephasing and non-rephasing maps recorded at $t = 600$ fs are reported in figure 4.15 together with six examples of fitted traces extracted in representative points of both rephasing and non-rephasing datasets. The multi-exponential model function well reproduces the decay and the beating of the experimental data. It is also worthy to notice that the fitting method is able to clearly resolve and distinguish signal features having similar frequencies and damping times, as displayed by the beat between the components 4 and 5 shown in figure 4.15(c).

Component Index n	1	2	3	4	5	6	7
Frequency ω_n (cm^{-1})	0	0	±31	±607	±702	±768	±938
Time constant τ_n (ps)	$\gg 2$	0.38	1.42	0.48	1.76	1.23	0.66

Table 4.1: Output parameters of the fitting procedure applied to rephasing and non-rephasing 2D data collected on ZnPc solutions. Confidence intervals obtained from standard errors of the fit are less than 1 cm^{-1} for frequencies and less than 60 fs for time constants. The estimation of the errors was performed using a procedure based on the analysis of the Jacobian of the residuals as reported in [102].

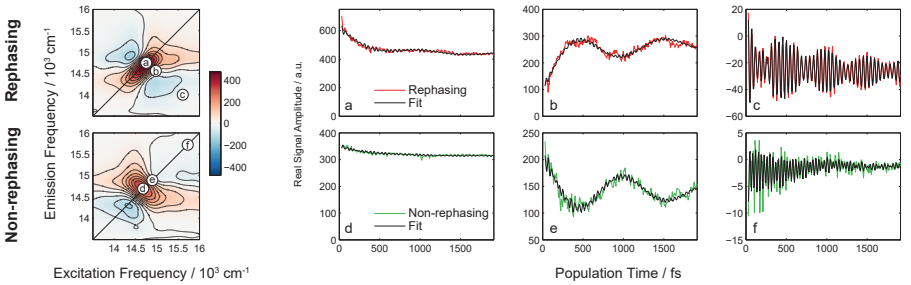

Figure 4.15: Rephasing (upper) and non-rephasing (lower) maps at $t = 600$ fs. Six traces extracted at representative points in rephasing (red lines) and non-rephasing (green lines) maps are shown (panels a-f). Reproduced from ref. [93].

The first two components ($n = 1,2$) are non-oscillating decaying components. The first one has a time constant estimated to be $\gg 2$ ps, it is thus almost constant in the investigated time window. It is related to the lifetime of the first excited state. The real DAS for the rephasing and non-rephasing datasets are shown in Figs. 4.16(a) and 4.16(c). They effectively account for the contributions to the signal that do not evolve within the investigated time window.

The second non-oscillating component has a time constant of 0.38 ps. The

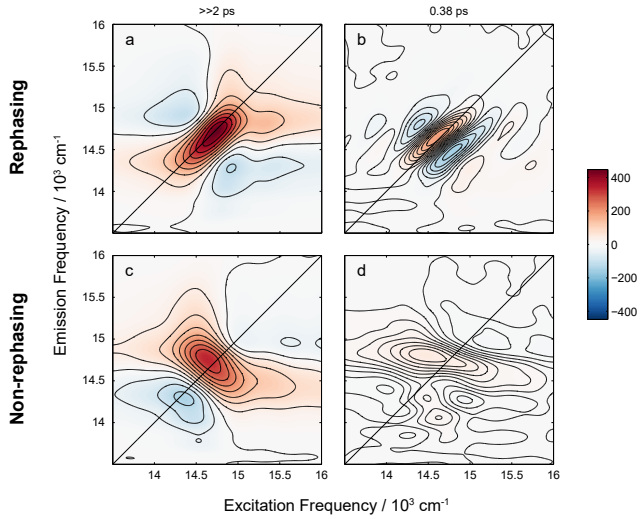

Figure 4.16: Real part of DAS of the two non-oscillating components for the rephasing (a,b) and non-rephasing (c,d) signals. (a) and (c) are related to the component $n = 1$ with a long decay time. (b) and (d) are associated to the component $n = 2$ with time constant 0.38 ps. Reproduced from ref. [93].

physical origin of this decay is unraveled by its DAS shown in Figs. 4.16(b) and 4.16(d). Rephasing real DAS in panel (b), points out that the signal is decaying on the diagonal (red area) and rising on two parallel regions above and below diagonal (blue areas). This DAS represents a broadening of the rephasing peak as a function of t, typically associated with the spectral diffusion phenomenon [111, 112]. Moreover, as expected for spectral diffusion, this contribution is negligible in the non-rephasing real DAS in panel (d) [10].

The five oscillating components identified by the fitting procedure ($n = 3-7$) have frequencies in agreement with the main vibrational modes detected in the Raman spectrum, except for component 3 that has a frequency of 30 cm^{-1} lying outside the investigated Raman spectral range. It is convenient to

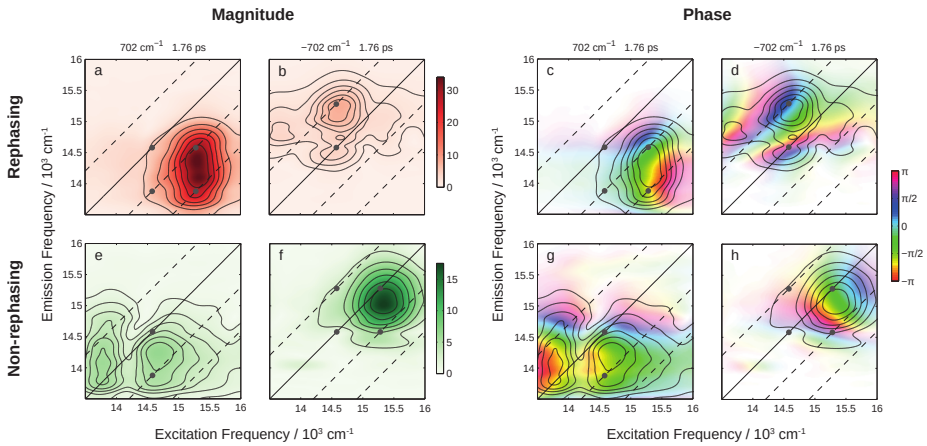

Figure 4.17: Complete set of information obtained with the fitting procedure for a single oscillating component. The magnitude and the phase of the CAS are shown for positive and negative beating frequencies and for rephasing and non-rephasing signals. As an example, the results for the 702 cm^{-1} component ($n = 5$) are shown. Reproduced from ref. [93].

analyze CAS in terms of magnitude and phase maps. The magnitude of CAS shows where that particular beating frequency contributes more in the 2D spectra, in analogy with the information provided by conventional FT-maps [59]. The phase of CAS displays the phase of the beating component at $t = 0$ fs. These maps have been demonstrated to be very sensitive to various system and laser pulse parameters. Despite the difficulty in their interpretation, their analysis may be of critical importance in the investigation of the origin of long lived coherences in multichromophoric systems [28]. figure 4.17 summarizes the complete set of information that can be extracted from the amplitude maps A_{nh} for each beating frequency.

The magnitude of CAS for the five oscillating components are reported in figure 4.18. CAS of $n = 3$ component, as expected for a low frequency mode, is mainly localized in the central area of the map close to the maximum of

the signal, Figs. 4.18(a) and 4.18(f). CAS of the higher frequency components present similar features, as shown in Figs. 4.18(b)–4.18(e) and 4.18(g)–4.18(j). In particular, in the rephasing CAS the oscillating signals are arranged in a "chair-pattern" as expected for vibrational coherences in the DHO model [113], as shown by the gray dots in Figs. 4.18(a)–4.18(e). The features are mainly localized below the diagonal, in particular at excitation frequency $\omega_{eg} + \omega_n$, where ω_{eg} is the resonant electronic transition frequency. Conversely, in non-rephasing CAS the amplitude is mainly distributed on the upper diagonal.

CAS of $n = 7$ component in Figs. 4.18(e) and 4.18(j) show a slightly different behavior since they present more contributions than what predicted by the DHO model. In fact, the frequency of this component (938 cm^{-1}) is close also to a Raman mode of THF (914 cm^{-1}), which can generate spurious contributions in the amplitude maps. Oscillating signatures resulting from vibrational modes of the solvent are known to contribute in the whole maps because of their non-resonant character [114]. Although the minimization procedure uses a single component to fit simultaneously the system and the solvent contributions, the corresponding CAS is able to clearly identify the presence of both contributions.

4.3.5 Discussion

The global fitting method proposed here has several advantages if compared to the currently available methods for the analysis of 2D spectra. The first remarkable feature is the simultaneous access to both the non-oscillating and oscillating dynamics of 2DES datasets in a unique step of analysis, while most of the previously proposed methods need separated and sequential treatments of the decaying part and of the beating part of the signal. Beyond the obvious advantage of reducing time and number of operations, this provides a remarkably higher reliability in the identification of the ultrafast decay and of the early part of the oscillating components. In fact, a standard real multi-exponential fit can easily fail to reproduce a fast decay because, at early times, it could

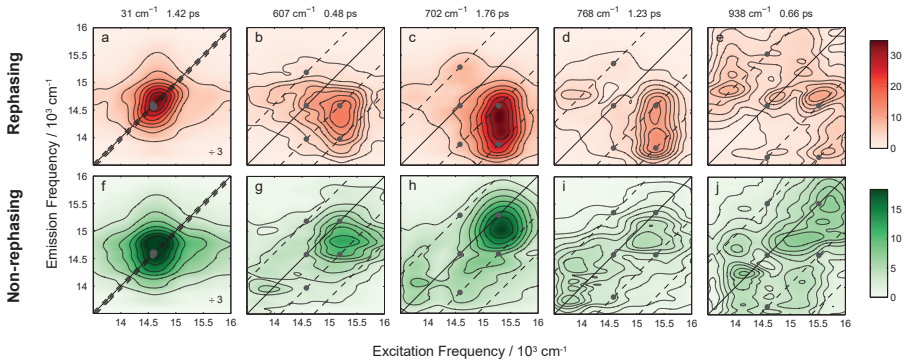

Figure 4.18: Sum of magnitude of CAS associated to positive and negative frequency for $n = 3-7$ components of rephasing (red) and non-rephasing (green) signal. Gray dots identify the coordinates where the oscillating signatures are expected to contribute, according to the DHO model. For an easier comparison, maps (a,f) are scaled by a factor 3. Reproduced from ref. [93].

be affected by strongly damped modes and low frequency oscillations. The proposed method naturally overcomes this issue since it fits simultaneously the decaying components and the oscillations. This is a particularly important aspect in the debate about the possible electronic nature of the beating recorded in 2D spectra of multichromophoric systems. Indeed, electronic coherence is usually strongly damped especially at room temperature[115]. The reliable determination of the amplitudes and damping times of oscillations contributing at early times is indeed at the base of a correct interpretation of the physical origins of the recorded beating [116].

A second remarkable advantage is the global character. The methods allows retrieving at the same time the frequencies, damping times and amplitude maps for all the fitted components considering simultaneously real and imaginary parts (i.e. the full complex dataset) of rephasing and non-rephasing signals. Since these features arise from common processes giving rise to real

and imaginary, rephasing and non-rephasing signals, the ability of considering the dataset in its completeness makes the final results more reliable and robust.

Moreover, since this method offers the possibility of selecting the number of components of the fitting function, the user can choose to quickly identify only the main components contributing to the overall signal, or analyzing in details also the weaker features. Indeed, as expected for a fitting method based on a least square minimization procedure, the components contributing the most to the overall decay will be identified first, independently on the values of the initial guess. The procedure is very robust and the main components will be always identified with a high degree of reliability. Additional weaker components possibly present are dropped in the residuals and one can choose if further analyze the data increasing the number of components.

A current limitation of the method is that it assumes that both coherence and population dynamics follow an exponential decay. This assumption is often fulfilled in simple systems, and in general it could satisfactorily reproduce any dynamics if enough exponential components are used. In systems affected by more complex dynamics the matrix **E** should be differently modeled in order to meaningfully capture the desired kinetics, for example associating specific species to the components of the model. Nevertheless, the procedure is quite flexible: any kind of kinetic model can be implemented suitably defining a correct form for the **E** matrix and then the minimization procedure can be applied as described.

Compared to Fourier transform based methods, the proposed procedure gives a clearer picture if the signal is corrupted by noise. Indeed, Fourier transform uniformly distributes time-domain noise throughout the frequency domain leading to a limitation of the accuracy in extracting peak frequencies, widths and magnitudes. An additional source of spurious signals in FT methods is caused by the finite duration of the experimental time-domain signals. Fourier transform of truncated time-domain signal generates undesirable

frequency-domain wiggles (called “Gibbs oscillations”) that hamper the identification of possible weak signals close to more intense peaks [117]. Indeed, if a FT-map at a certain frequency has an intense amplitude, it generates ghosts features in the FT-maps relative to close frequencies, hindering the detection of subtle features. Moreover, the performances of the FT methods are strongly dependent on experimental conditions, such as the time window and the time step used in the experiment, and this has a strong influence on the resolution and on the spectral range of the Fourier transform [117]. The method proposed here overcomes all these issues. The finite duration of the signal is indeed not a limitation since the fitting model reproduces the data within the chosen time window without truncation artifacts. The consequence is that components with close frequencies can be distinguished easier than in FT methods.

A relevant novel aspect of this method, if compared to FT methodologies, is its ability to distinguish components based on their dynamic behavior. Indeed, if the components have different physical origins and thus are characterized by different dephasing times, the fitting method will recognize different components with similar ω_n but different τ_n and will produce CAS, also expected to have different amplitude distribution. It would be thus possible, for example, to distinguish between electronic and vibrational coherences, typically dephasing at room temperature in tens and thousands of femtoseconds, respectively. In the same way the contribution of solvent modes could be distinguished from molecular vibrations contributing in the same spectral region [114].

The disentanglement of beating components with close frequencies is a crucial aspect to assess the electronic or vibrational nature of coherent oscillations and verify the possible interplay between vibrational and electronic degrees of freedom. Time-frequency transforms could in principle give access to time resolution and to the same information, but one must be careful and consider all the possible artifacts. As a consequence time-frequency analysis is not the best tools to perform a quantitative analysis for typical 2DES signals.

CHAPTER 5

Model Systems

Model artificial systems can greatly help the understanding of subtle properties of the coherent dynamics of multichormophoric systems. They allow systematic studies in which trends in series of samples can be rationalized. This approach contrasts the direct study of complex biological systems that are usually characterized by intricate structures and optical responses. In this chapter the investigation of a porphyrin-based multichromophoric system is pursued. In section 5.1 the general structure of the samples is described. Linear absorption spectra are simulated with an effective model Hamiltonian in section 5.2, whereas conformational ordering of chromophores is unraveled with molecular dynamics simulations in section 5.3. After this preliminary investigation, 2DES measurements are presented in section 5.4 and discussed in section 5.5.

5.1 Structure

The studied systems are porphyrin-based multichromophoric polymers [118, 119], provided by Prof. Giorgini research group of the University of Bologna. The polymer is composed of a polymethacrylate backbone with tetraphenil-porphyrin moieties linked at each monomeric residue. Two slightly different polymeric samples have been compared and characterized. In figure 5.1 the detail of the structure is shown. In polymer P1 the porphyrin moieties are connected to the backbone by a lactic acid residue whereas in polymer P2 the chromophores are directly linked to the methacrylate chain. The polymers are quite short and contain about 8-10 monomeric units. All the characterization have been carried out also on the monomer M as a control.

The porphyrin moieties were chosen because they mimic chlorophylls, ubiquitous biological antennae chromophores [120]. The key design idea behind this system is the construction of a synthetic multichromophoric system as simple as possible but still retaining the basic characteristics of an antenna. The polymeric backbone acts as a scaffold which keeps the chromophores together and constrains distances and orientations. The similarity with the biological system is not the closest possible but the aim is to work with a highly modular and easy modifiable system and verify how structural aspects affect the interaction between the chromophores. The study of simplified model systems should be pay back with a deeper understanding of details of the spectroscopic responses of the samples.

The electronic properties of porphyrins are determined by the aromatic nature of the tetrapyrroles core. Moreover the symmetry of the macrocycle core is crucial for the degeneracy of the electronic transitions involving frontier orbitals. The typical UV-Visible spectra of porphyrins exhibit absorptions in two regions termed the Soret or B band (~380-420 nm) and the Q bands (~500-800 nm). This is a result of the splitting of the main frontier molecular orbitals, as

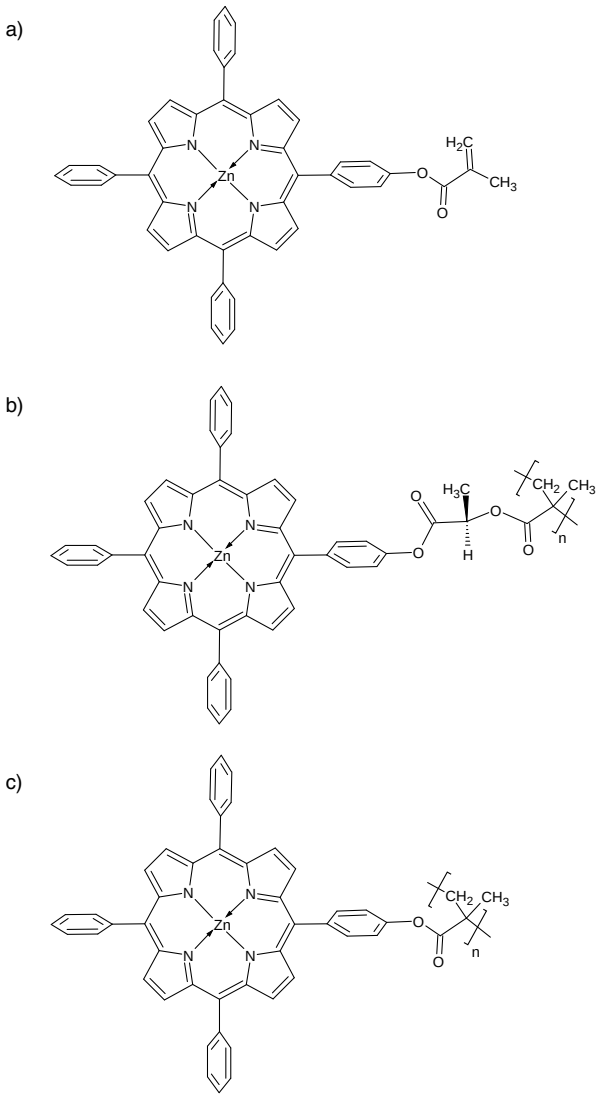

Figure 5.1: Chemical structure of the studied systems ($n \approx 8-10$): (a) M, (b) P1 and (c) P2.

described by the semi-quantitative four-orbital model of Gouterman in figure 5.2, a mixture of Hückel and configuration interaction theory [121, 122]. A key-difference between the spectra of metalloporphyrins and their free-base counterparts is the number of observed Q bands. The Zinc tetraphenylporphyrin belongs to the D_{4h} molecular point group and exhibits the highest symmetry possible for a porphyrin derivative, so that two doubly degenerate electronic transitions are predicted. Linear absorption spectra of the samples in the visible range are plotted in figure 5.3. They show an intense Soret band at about 23700 cm^{-1} and two less intense Q bands at about 16800 and 18000 cm^{-1}. Both Soret and Q bands are associated to doubly degenerate electronic transitions mainly involving four frontier orbitals, see figure 5.2. The vibronic structure of the Q bands is generated by a strongly coupled molecular vibration with frequency ~1300 cm^{-1} associated to vinyl stretching of the tetrapyrroles ring [123]. Moreover Q bands have very small oscillator strength which suggests that this electronic transition should not be significantly affected by interaction between chromophores in the polymer. Indeed their shapes, relative intensities and peaks positions are well preserved in all the spectra.

Polymers exhibit a remarkable decrease of intensity and a broadening of the Soret bands. These modifications are the signature of the interaction between chromophores. The right panel of figure 5.3 clearly highlights that in polymers the maximum of the band is shifted. In P1 and P2 the shift from the monomer band is about 60 and 170 cm^{-1}, respectively. A trend in the shape, broadening and peak position of Soret bands can be glimpsed in the linear absorption spectra going from M to P1 to P2. P1 acts like an intermediate case between the isolated monomer, in which chomophores do not interact, and the polymer P2, in which chromophores are held closer by the methacrylic backbone.

Clear formation of new excitonic bands is not observed, therefore it is not easy to extract direct information about the coupling strength from the linear absorption spectra. There might be two main reasons for that: (i) the

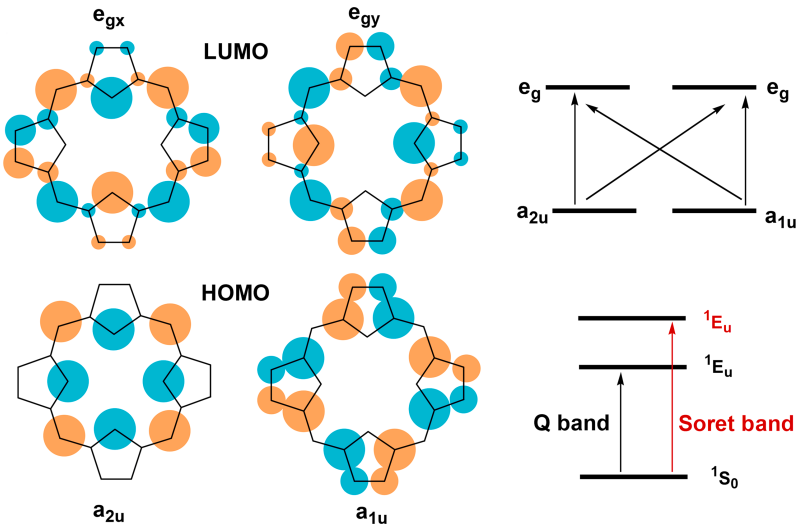

Figure 5.2: (left) The orbitals involved in the Gouterman four-orbital theory [122] and (right) the simplified representation of the electronic transitions from HOMO to LUMO, adapted from [121].

chromophores are interacting in the low coupling regime and the amount of splitting is not enough to emerge from the broadening of the bands, (ii) the system has a lot of conformational degrees of freedom, a great number of structures are possible and the linear absorption spectrum is the result of the average of a very disordered behavior. In order to address this problem a model was developed to simulate the linear absorption spectrum of all the samples in the Soret band range. It is presented in the next section.

5.2 Model for linear absorption

Let's consider a polymer composed by N monomeric residues, each one containing a chromophore moiety which can be electronically excited. Each monomeric residue is labeled with the number $n = 1,2,3,...,N$. In order to

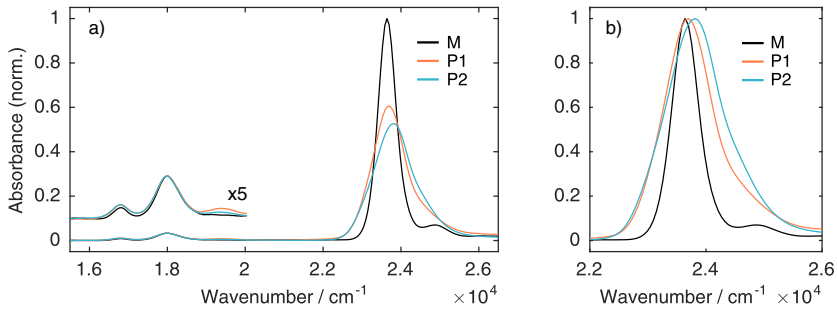

Figure 5.3: Linear absorption spectra of the samples M, P1 and P2 in THF solvent at room temperature, recorded in 1 mm optical path cuvettes with a Varian Cary 5 Spectrometer. (a) Spectra normalized on the Q bands and (b) spectra normalized on the Soret bands.

account quantitatively for exciton-vibrational coupling we start from a simple model in which the nuclear potential corresponding to the ground (g) and electronically excited (e) molecular states are shifted harmonic wells of identical frequency ω_0 [35]. The shift is quantified by the Haung-Rhys factor HR, defined as the average number of phonons created during a vertical transition [124]. This model can easily explain the main coupled normal mode to the B band which induce a side peak in the linear absorption spectrum of the monomer. The absence of a vibronic progression is a signature of small coupling and thus low HR. The main observed coupled mode has a frequency of about 1300 cm^{-1} and, like the Q bands, it is associated with vinyl stretching modes of the porphyrin ring.

The polymer Hamiltonian is defined starting from the one-particle approximation [35]: in this assumption an excitation consists of a vibronically excited chromophore at site n with v excited-state quanta in the e nuclear potential, with all other molecules electronically and vibronically unexcited. The one-particle approximation is enough to describe systems in which the excitonic

coupling is small [125]. Using this simplified picture the basis set is specified as $|n,v\rangle = \{|1,0\rangle, |1,1\rangle, |2,0\rangle, |2,1\rangle, ..., |N,0\rangle, |N,1\rangle\}$, meaning that in the state $|n,v\rangle$ the chromophore n is electronically excited and the vibration can be unexcited ($v = 0$) or singly excited ($v = 1$). The states $|n,v\rangle$ are still related to the non interacting isolated monomeric units. Here only the first excited vibrational state is included and necessary due to the low HR. For a N units polymer the total number of states in the basis set is $2N$.

The α-eigenstate of the aggregate Hamiltonian can be expanded in one-particle states of the isolated monomer:

$$|\psi^{(\alpha)}\rangle = \sum_{n=1}^{N} \sum_{v=0}^{1} c_{n,v}^{(\alpha)} |n,v\rangle . \tag{5.1}$$

The coefficients of the expansion can be evaluated diagonalizing the aggregate Hamiltonian H. The diagonal elements of H consist of the energies of the localized states $\epsilon + \delta\epsilon_n + v\omega_0$. Here ϵ is the energy of the $0 \leftarrow 0$ transition of the monomer and $\delta\epsilon_n$ represents a static disorder-induced change in the transition energy at site n. The value of $\delta\epsilon_n$ is picked from a Gaussian distribution with zero mean and a standard deviation σ_ϵ. The off diagonal elements of H are represented by the usual excitonic Hamiltonian,

$$H_{ex} = \sum_{n,n'} J_{nn'} |n\rangle \langle n'| \tag{5.2}$$

where $|n\rangle$ represents a pure electronic excitation at site n and $J_{nn'}$ is the excitonic coupling between the n-th and the n'-th chromophoric unit. The off diagonal matrix element of H connecting one-particle states allows for wave-like energy transfer in the conventional Frenkel exciton theory [126]. In the considered system the coupling is supposed to be small and we assume that only nearest neighbors can interact significantly in the average picture. A lot of conformations for the polymer are possible and we assume that the interaction

between consecutive units are much more probable than the interaction between non consecutive units. We can rearrange equation 5.2 introducing this simplification,

$$H_{ex} = \sum_{n=1}^{N-1} (J + \delta J_n) \left(|n\rangle \langle n+1| + |n+1\rangle \langle n| \right). \tag{5.3}$$

Now the chromophore pairs interact with an average nearest-neighbor coupling constant J. The coupling disorder is inserted using δJ_n picked from a zero-mean Gaussian distribution with sigma σ_J. Moreover all the matrix elements of H_{ex} necessarily involve vibrational overlap integrals between g and e which depend on the HR factor [125], see equation 5.4. The overlap $f_{00} = e^{-\frac{HR}{2}}$ is calculated for the $0 \leftarrow 0$ transition and the overlap $f_{10} = \sqrt{HR} e^{-\frac{HR}{2}}$ is for the $1 \leftarrow 0$ transition.

The matrix representation of the Hamiltonian is then

$$H = \begin{pmatrix} \epsilon_1 & 0 & J_1 f_{00} f_{00} & J_1 f_{00} f_{10} & 0 & 0 & \cdots \\ 0 & \epsilon_1 + \omega_0 & J_1 f_{10} f_{00} & J_1 f_{10} f_{10} & 0 & 0 & \cdots \\ J_1 f_{00} f_{00} & J_1 f_{10} f_{00} & \epsilon_2 & 0 & J_2 f_{00} f_{00} & J_2 f_{00} f_{10} & \cdots \\ J_1 f_{00} f_{10} & J_1 f_{10} f_{10} & 0 & \epsilon_2 + \omega_0 & J_2 f_{10} f_{00} & J_2 f_{10} f_{10} & \cdots \\ 0 & 0 & J_2 f_{00} f_{00} & J_2 f_{10} f_{00} & \epsilon_3 & 0 & \cdots \\ 0 & 0 & J_2 f_{00} f_{10} & J_2 f_{10} f_{10} & 0 & \epsilon_3 + \omega_0 & \cdots \\ \vdots & \vdots & \vdots & \vdots & \vdots & \vdots & \ddots \end{pmatrix}, \tag{5.4}$$

in which for compactness we have $\epsilon_n = \epsilon + \delta\epsilon_n$ and $J_n = J + \delta J_n$. The diagonalization of the Hamiltonian H gives a new set of $2N$ energies and all the coefficients $c_{n,v}^{(\alpha)}$ of the new eigenstates.

The first step to calculate the theoretical absorption spectra of polymers is to simulate the monomer spectrum. M can be imagined as a polymer with $N = 1$. In this case the basis functions $|1,0\rangle, |1,1\rangle$ are already eigenstates. Ac-

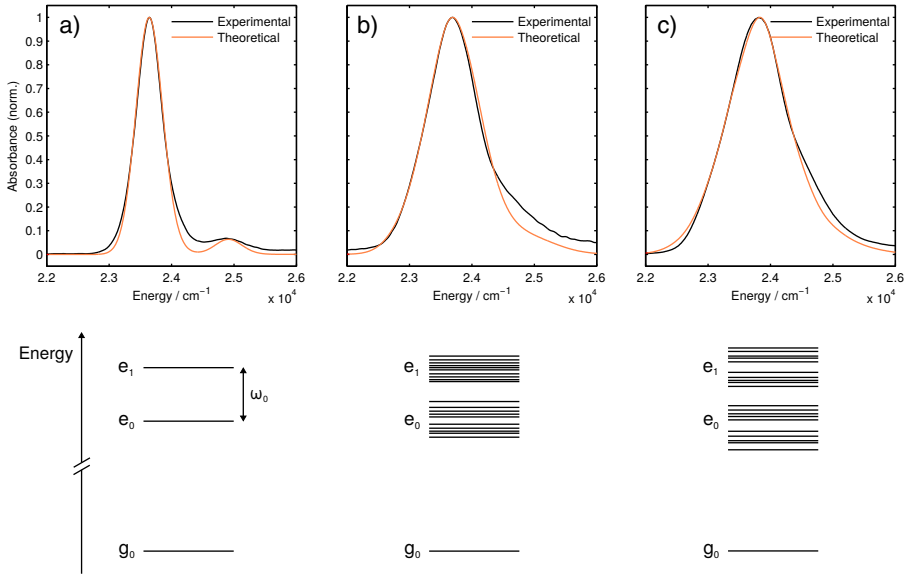

Figure 5.4: Comparison of experimental and simulated linear absorption spectra in the spectral region of the B band. (a) Simulation of the M spectrum with parameters: $\epsilon = 23650$ cm^{-1}, $HR = 0.06$, $\omega_0 = 1270$ cm^{-1}, the lineshape function including two over-damped Brownian oscillator was optimized to fit the bandwidth of the peaks. (b) Simulation of the P1 spectrum with parameters: $N = 10$, $J = 23$ cm^{-1}, $\sigma_J = 49$ cm^{-1}, $\sigma_\epsilon = 395$ cm^{-1}. (c) Simulation of the P2 spectrum with parameters: $N = 10$, $J = 61$ cm^{-1}, $\sigma_J = 39$ cm^{-1}, $\sigma_\epsilon = 479$ cm^{-1}. The polymer spectra were averaged over 200 realizations in order to cancel out the random behavior of the model. Under each spectrum a schematic representation of the energy levels is reported.

cording to this model two transitions far apart ω_0 are expected in the UV-Visible spectrum with transition dipoles proportional to the vibrational overlap f_{00} and f_{10}. The linear absorption spectrum $S(\omega)$ is calculated using the expression [10]

$$S(\omega) = \sum_{\alpha} |\mu^{(\alpha)}|^2 \, \Re \int_0^{\infty} dt \, \exp(i\omega^{(\alpha)} t - g^{(\alpha)}(t)) \tag{5.5}$$

which contains the transition dipoles $\mu^{(\alpha)}$ to account for the intensity of each transition, the frequency of the transition $\omega^{(\alpha)}$ to set the absorption peak in the correct position and a lineshape function $g^{(\alpha)}$ to introduce the broadening of the peaks induced by the coupling with the external bath. The lineshape function is obtained from the autocorrelation function of the transition energy fluctuations [10]. It contains the information related to the interaction with the environment and it is crucial to reproduce the shape of the spectrum. Generally $g^{(\alpha)}(t)$ is modeled using low-frequency coupled overdamped Brownian oscillators [27]. In the overdamped semi-classical approximation of the bath the lineshape function can be defined as

$$g^{(\alpha)}(t) = \sum_{m=1}^{M} \frac{\lambda_m}{\gamma_m} \left(\frac{2}{\beta \gamma_m} - i \right) \left(e^{-\gamma_m t} + \gamma_m t - 1 \right), \tag{5.6}$$

where M is the total number of employed Brownian oscillators, $\beta = 1/k_B T$ is the inverse of the Boltzmann constant multiplied by the absolute temperature, λ_m and γ_m are respectively the reorganization energy and the damping factor for the m^{th}-oscillator. A general lineshape, with variable contribution of inhomogeneous and homogeneous broadening, can be usually reproduced using a fast and a slow overdamped oscillators. For the simulation of the monomer spectrum, the same lineshape function is used for the two vibronic transitions, the parameters are $\lambda_1 = 20$ cm^{-1}, $\gamma_1 = 3.33$ cm^{-1} and $\lambda_2 = 100$ cm^{-1}, $\gamma_2 = 166.8$ cm^{-1}. We will denote the corresponding lineshape function as $g^{(\mathrm{M})}(t)$, and accordingly the dipole moment will be denoted as $\mu^{(\mathrm{M})}$.

Once the parameters that reproduce a good monomer spectrum are obtained, the polymer spectrum is calculated using equation 5.5. The transition dipole moments of the polymers are obtained from a combination of the transition dipole moments of the monomer using the coefficients $c_{n,\nu}^{(\alpha)}$,

$$\mu^{(\alpha)} = \sum_{n=1}^{N} \sum_{\nu=0}^{1} c_{n,\nu}^{(\alpha)} f_{\nu,0} \mu^{(M)}, \tag{5.7}$$

similarly the lineshape functions of polymer eigenstates are obtained from a suitable combination of monomer lineshapes [22]. Therefore the majority of the input parameters of the model are shared with the simple monomer description. Finally an average over multiple realizations has to be carried out in order to cancel out the random properties introduced by the random contribution δ_J and δ_ϵ. Three polymer-specific parameters remain to be determined: J, σ_J and σ_ϵ. These were calculated implementing a fitting procedure of the experimental data, the results are reported in figure 5.4.

Theoretical and experimental data have a general good agreement. The higher the value of the average coupling J, the bigger the shift of the maximum of the peak. This trend is coherent with the fact that the polymer P2 is more constrained, the chomophores are forced to stay closer, and it is characterized by a higher positive J leading to a higher H-aggregate character. The polymer P1 has a smaller positive J and at the same time a less prominent static disorder σ_ϵ, this confirms the fact that P1 has an intermediate behavior between M and P2. The off-diagonal disorder, quantified by σ_J, is greater in polymer P1 than P2. This seams reasonable because of the presence of the spacer which enhances the mobility of the porphyrin planes increasing the variability of the interaction in couples of chromophores. What prevents a perfect match of the simulation with experimental data is the absence in the model of weakly coupled low frequency modes. In the monomer, the inclusion of these modes should be able to fill the gap between the two transitions considered in the

theoretical spectrum. Nevertheless the results are satisfactory and provides the wanted information about couplings and disorder.

5.3 Computational Investigation

A fine investigation on the structure was performed using fully-atomistic molecular dynamics (MD) in collaboration with Dr. Mirco Zerbetto from the University of Padova. For each system a simulation box containing one molecule of sample solvated with THF molecules was prepared. Figure 5.5 shows an example of three snapshots of the simulation boxes. The force field was derived from the CHARMM protein force field [127], a polymethylmethacrylate force field [128] and a THF force field [129]. The electrostatic potential of the monomeric residues of each sample was calculated with a quantum mechanical simulation with the software Gaussian® release 03 (geometry optimization, Hartree-Fock energy calculation and a 6-31G(d,p) basis set). Then the partial charges of all the atoms were determined fitting the electrostatic potential using the AMBERTOOLS suite [130]. Figure 5.6, 5.7 and 5.8 report in details atom labeling and partial charges. For the three samples, a 70 ns long molecular dynamics (MD) trajectory has been calculated with an integration time step of 2 fs using the software NAMD [131]. System configuration was dumped every 100 integration steps, i.e. the resolution of the trajectories is of 200 ps. In a first step of the computational study, the effect of different flexibility of the two polymers backbones on the ordering and staking of the porphyrins is investigated. To this purpose, orientational order parameters and average distances are compared for couples of porphyrins in the two polymers. While distances are calculated as the distance between the Zn atoms, which is trivially extracted from the MD trajectories, for the orientational order we define a porphyrin-fixed reference frame, see panel 5.9(a).

The first step is to calculate the Euler angles $\mathbf{\Omega}_{i,j}$ providing the relative

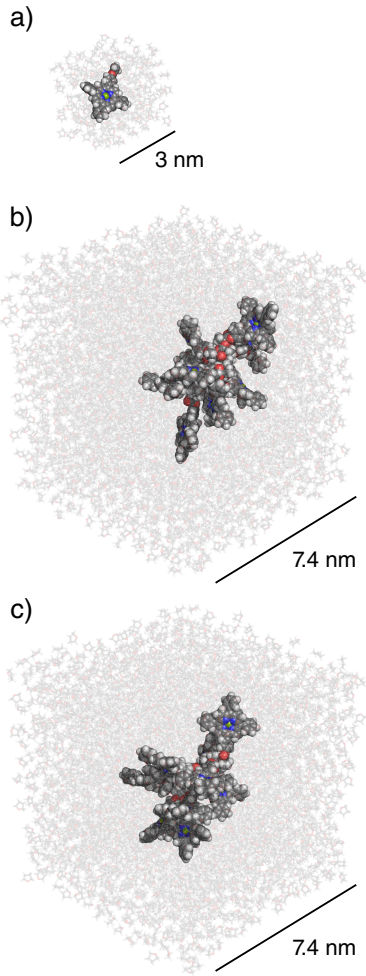

Figure 5.5: Renders of a snapshot of the simulation boxes for (a) M, (b) P1 and (c) P2. Solvent molecules are represented as partially transparent to better expose the chromophoric systems.

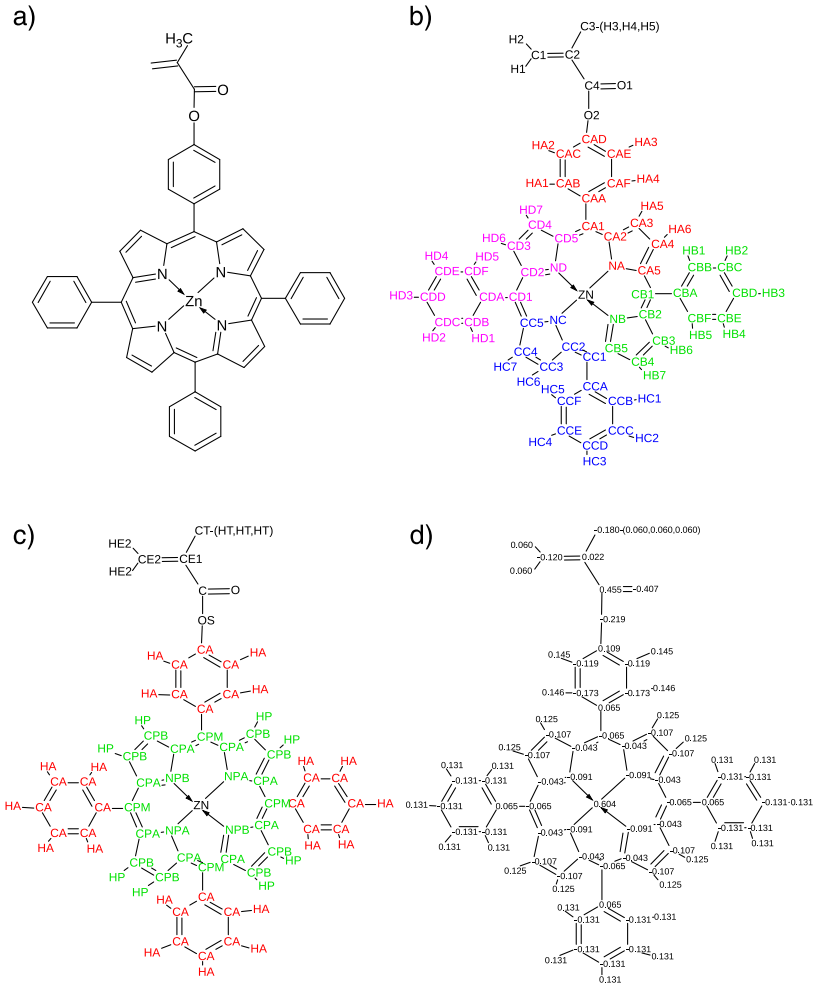

Figure 5.6: (a) Chemical structure of M; (b) atom labeling; (c) atom types that share the same force field parametrization; (d) partial charges that best fit the electric field obtained trough quantum mechanical simulation.

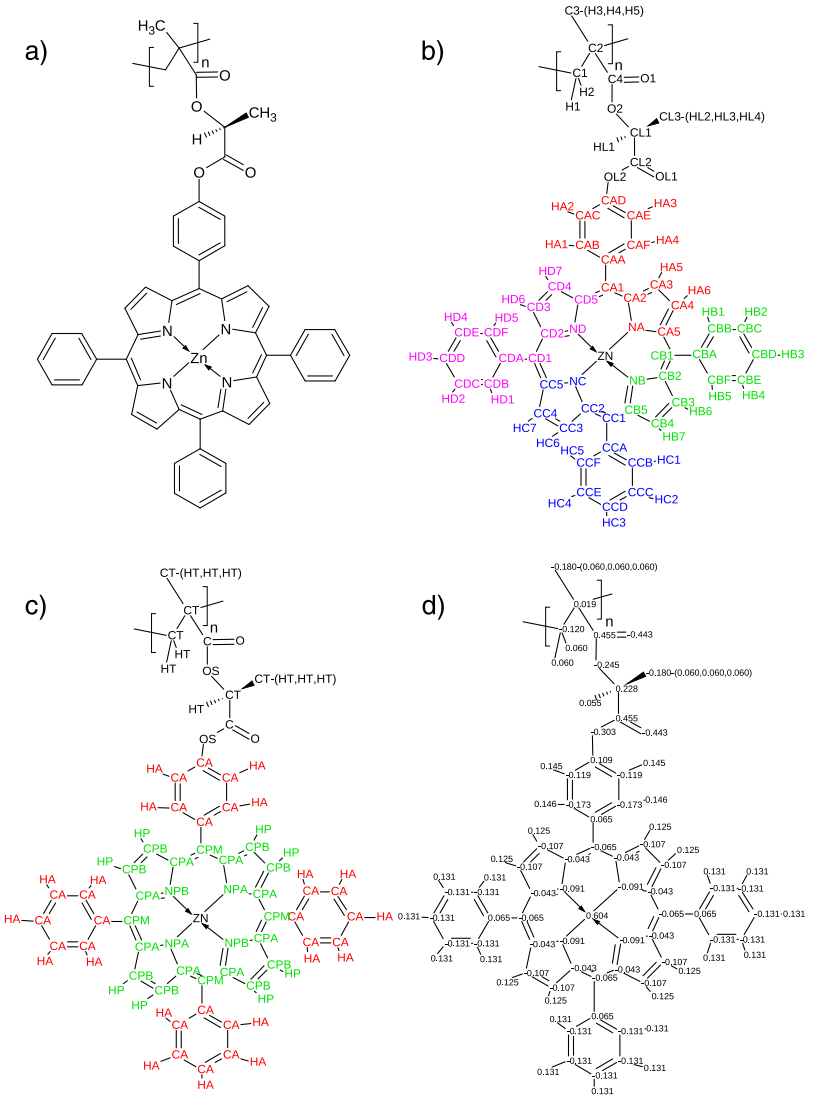

Figure 5.7: (a) Chemical structure of P1; (b) atom labeling; (c) atom types that share the same force field parametrization; (d) partial charges that best fit the electric field obtained trough quantum mechanical simulation.

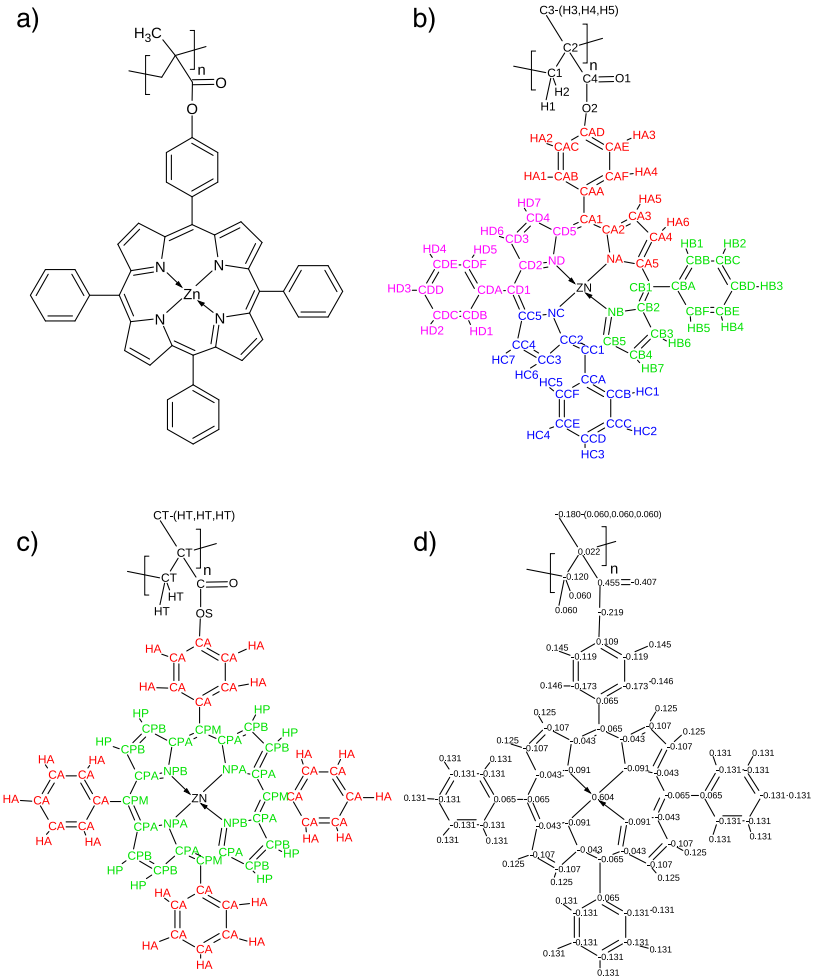

Figure 5.8: (a) Chemical structure of P2; (b) atom labeling; (c) atom types that share the same force field parametrization; (d) partial charges that best fit the electric field obtained trough quantum mechanical simulation.

orientation of porphyrin j with respect to porphyrin i. From a general set of Euler angles $\mathbf{\Omega}(t)$ evolving during the MD trajectory, it is possible to define several order parameters. Here we select two parameters usually employed in analysis of liquid crystals ordering, which are obtained from rank 2 Wigner matrices, $D^2_{m,m'}(\mathbf{\Omega})$, as

$$S_0^2 = \left\langle D^2_{0,0}(\mathbf{\Omega}) \right\rangle \tag{5.8}$$

which, based on the definition of the porphyrin-fixed frame, provides information about the degree of collinearity of the normals of the two porphyrin planes, and

$$S_2^2 = \left\langle D^2_{0,2}(\mathbf{\Omega}) + D^2_{0,-2}(\mathbf{\Omega}) \right\rangle \tag{5.9}$$

which is an index of the tilting around the normals of the porphyrin rings, usually called rhombic ordering. The brackets denote the average over the complete MD trajectory.

While order parameters are important to establish spatial confinement of the motion, correlation times are the quantities that bring information about the motional regime. Thus, to complete the desciption of the motion of the porphyrin moieties we calculate the auto-correlation functions

$$G_{2,0} = \left\langle \left(D^2_{0,0}(\mathbf{\Omega}(0)) \right)^* D^2_{0,0}(\mathbf{\Omega}(t)) \right\rangle \tag{5.10}$$

and

$$G_{2,0} = \left\langle \left(D^2_{0,2}(\mathbf{\Omega}(0)) + D^2_{0,-2}(\mathbf{\Omega}(0)) \right)^* \left(D^2_{0,2}(\mathbf{\Omega}(t)) + D^2_{0,-2}(\mathbf{\Omega}(t)) \right) \right\rangle. \tag{5.11}$$

At $t = 0$ the two correlation functions provide the amount of correlation of the relative orientational motion of the two porphyrins, i.e. to which extent the two tetrapyrrole rings yaw or roll-pitch in concert. When $t \to \infty$, the correlation function tends to the square of the order parameters defined in equations 5.8 and 5.9. The decay of the correlation function is, in general, multi-exponential

with several correlation time components influencing the relaxation towards equilibrium. To simplify the discussion, we will compare the effective correlation times, defined as

$$\begin{aligned}\tau_{2,0} &= \int_0^\infty dt\, \frac{G_{2,0}(0) - \left(S_0^2\right)^2}{G_{2,0}(t) - \left(S_0^2\right)^2} \\ \tau_{2,2} &= \int_0^\infty dt\, \frac{G_{2,2}(0) - \left(S_2^2\right)^2}{G_{2,2}(t) - \left(S_2^2\right)^2},\end{aligned} \tag{5.12}$$

which correspond to the area of the normalized average-less auto-correlation functions.

Order parameters S_0^2 and S_2^2 and correlation times $\tau_{2,0}$ and $\tau_{2,2}$ are calculated for all the possible couples of porphyrins and are reported in panels 5.9(c) and 5.9(d). For both polymers most of the couples of porphyrins are located in the low ordering region. However, the most relevant feature of panel 5.9(c) is the fact that a considerable number of couples of P2 porphyrins are located in the center of the plot where the order parameters are higher, while this is not observed for P1. This means that a certain degree of stacking is present in P2.

In order to discuss the correlation times we must recognize that the concept of mobility is the results of two combined effects. The first is the mechanical mobility, which is related to the hypervolume in phase-space that the coordinates can explore, based only on energetic arguments. The second contribution is related to the kinetic mobility that describes the ease of motion within the accessible hypervolume. In terms of stochastic motion, the second kind of mobility is related to the friction force that opposes to a change in molecular configuration. The mechanical and kinetic mobilities both influence the time scales of the motion, i.e. they influence correlation times. In particular, given a dynamic process, its characteristic time scale will be larger for (i) larger mechanical mobility, i.e. wider hypervolume to be explored, and (ii) for smaller kinetic mobility, i.e. high friction is preventing the molecules to explore the

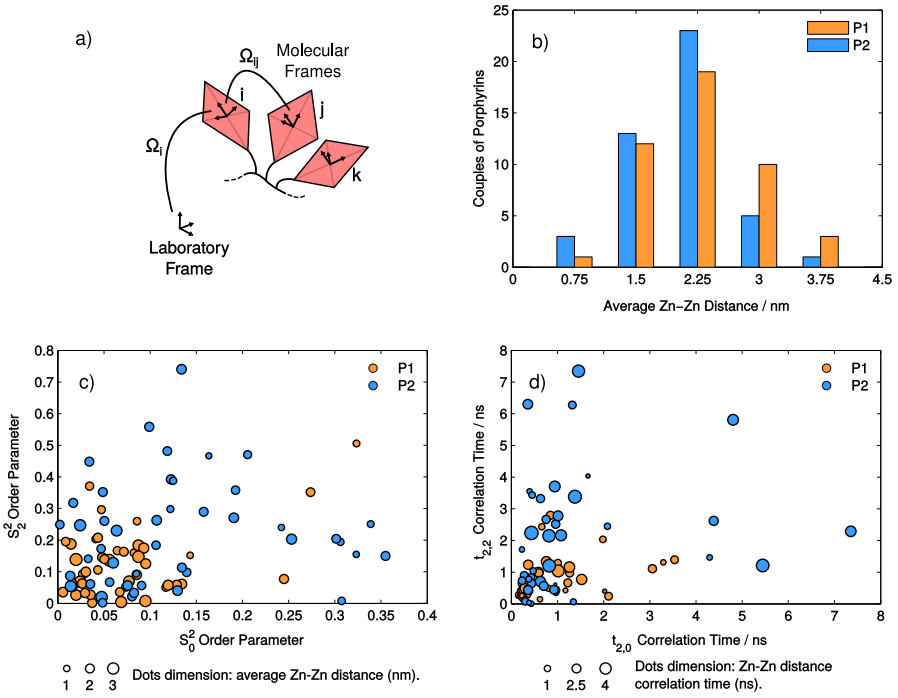

Figure 5.9: Molecular dynamics trajectory analysis. (a) Each chromophore represented by a red square has a molecular reference frame with origin on the Zn atom to probe porphyrin plane orientation. (b) Histogram of Zn-Zn distances between all couples of porphyrins; P1 has bigger average distances than P2. (c) Order parameters for axial, S_0^2, and rombic, S_2^2, ordering; P1 has more dots near the origin of the graph suggesting less order than P2. (d) Correlation times for axial, $t_{2,0}$, and rombic, $t_{2,2}$, degrees of freedom; P1 has shorter correlation time than P2.

available free phase-space. In panel 5.9(c), polymer P2 shows longer correlation times than P1. Considering also the higher order parameters found for P2, the slower time-scales are realistically due to a smaller kinetic mobility due to the friction induced by the shorter distances between porphyrin moieties.

5.4 2DES expertiments

The dynamics within the Soret band was investigated with the 2D electronic spectroscopy technique. We decided to focus on this band for two main reasons: (i) this band owns the bigger oscillator strength and its excitation generates higher 2D signals and thus better quality data with respect to Q bands, (ii) as confirmed by linear absorption spectra, the Soret band represents the optimal choice to investigate the effect of the interaction between chromophores in polymer samples.

Unfortunately, the frequency range around 23700 cm^{-1}, ~420 nm, turned out to be not very convenient for what concerns the experimental apparatus efficiency. The Ti-sapphire laser source of our setup emits light at 800 nm and the non-collinear optical parametric amplifier is not efficient when it is tuned to produce pulses near the pump wavelength range or near its second harmonic. The setup had to be slightly modified from the standard; the TOPAS was tuned to produce pulses at about 840 nm and then a second harmonic generator crystal was used to obtain the wanted exciting wavelength. Pushing the setup to its limit, a pulse length of about 50 fs centered on top of the Soret band was recovered for the experiment. These conditions are far from the ideal maximum efficiency when pulses of about 10-20 fs can be generated. The ideal 2DES experiment requires the shortest possible laser pulse to investigate a large spectral window and to obtain the maximum amount of information from the dataset. Indeed, for nearly transform limited pulses, the shorter is the pulse duration, the widest is the spectral bandwidth. A long pulse has a second

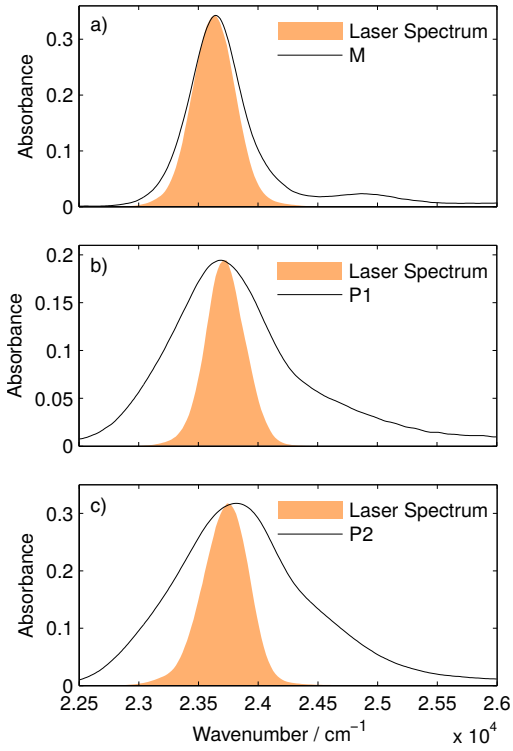

Figure 5.10: Superposition of linear absorption spectra and pulse spectrum in 2DES experiments. (a) M, (b) P1 and (c) P2.

negative effect: it smooths out the coherences reducing the detectable signal. All these technical difficulties probably explain why only one 2DES experiment centered on the Soret band of porphyrins has been published to date [132]. Nevertheless, good quality data could be recorded thanks to the experimental improvements implemented, as described in chapter 3.

In figure 5.10 superpositions of laser spectra and linear absorption spectra are reported. The laser spectrum is not covering the entire absorption bands. For polymers, in particular, the laser band has a strong effect on the recorded

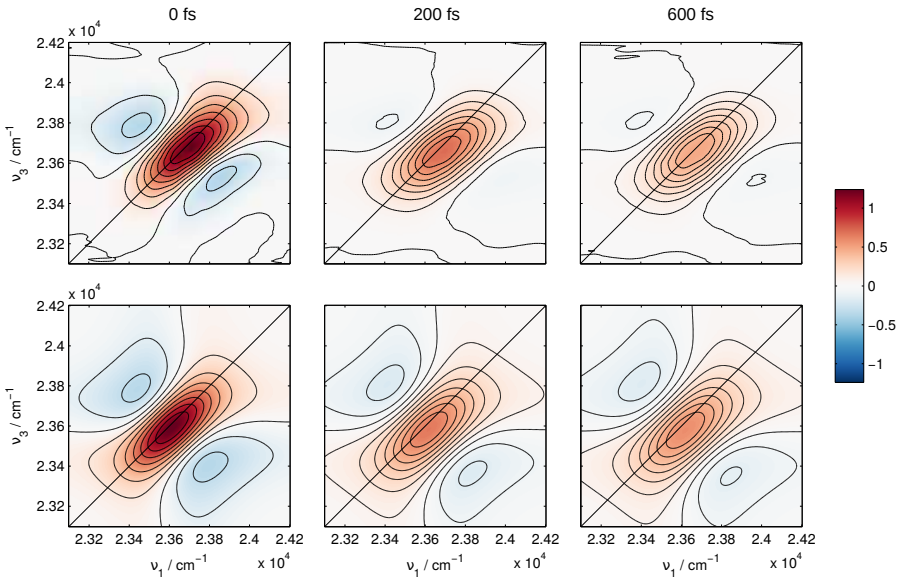

Figure 5.11: Experimental (top row) and theoretical (bottom row) real rephasing 2DES maps of the monomer at t_2 equal to 0, 200 and 600 fs. The simulation takes into account the pulse length and spectrum using the convolution procedure presented in [133].

third order signal. The positions of signal maxima in 2DES maps depend on the maximum of the laser spectrum, and the width of the features are limited by the maximum bandwith of the laser spectrum [133, 134].

As for the analysis of the linear absorption spectra, the first step is to investigate the information encoded in the monomer data. A selection of maps at different t_2 delay times is reported in figure 5.11. Two main contributions are present in the rephasing maps of the monomers: ground-state bleaching (GSB) and stimulated emission (SE). They can be interpreted using the double-sided Feynman diagrams reported in figure 5.12. In the maps of figure 5.11 the main peak along the diagonal corresponds to the Soret transition cen-

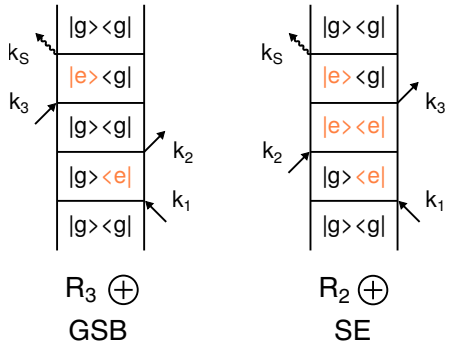

Figure 5.12: Double-sided Feynman diagrams for GSB and SE contributions to the rephasing signal of the monomer; the vibronic structure in each electronic state is not considered. The density matrix formalism is employed, $|e\rangle$ is the exited state responsible for the Soret band transition and $|g\rangle$ is the ground state.

tered at ν_{eg} =23650 cm^{-1}. The vibronic shoulder at 24890 cm^{-1} is outside the laser spectral window and thus it is not captured by the experiment. The two contributions, GSB and ES, are both responsible for the positive peak on the diagonal. In fact, both Feynman diagrams in figure 5.12 evolve during the time t_1 and t_3 with the coherences $|g\rangle\langle e|$ and $|e\rangle\langle g|$, respectively, both oscillating at the characteristic frequency ν_{eg}. Indeed most of the signal is centered at the coordinate $(\nu_1, \nu_3) = (\nu_{eg}, \nu_{eg})$. The main difference between the two kind of signals is the pure state evolving during time t_2: ground state $|g\rangle\langle g|$ in GSB and excited state $|e\rangle\langle e|$ in SE. The two contributions can not be separated and a single main feature is observed. The spectrum is elongated along the diagonal because of the inhomogeneous broadening. As t_2 evolves, the peak shape becomes rounder because of the spectral diffusion: after the excitation event, the environment fluctuations induce gradually a loose of correlation between excitation and emission.

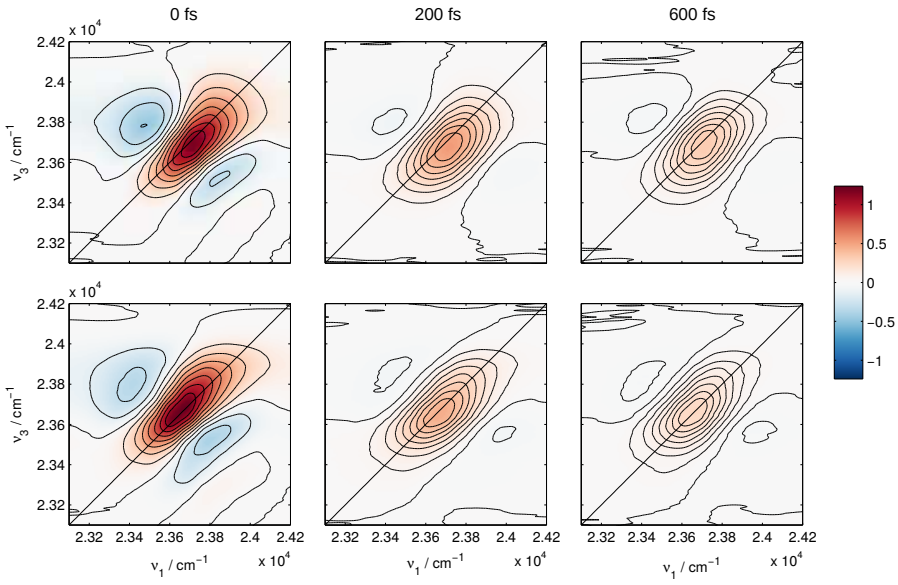

Figure 5.13: (top row) P1 and (bottom row) P2 real rephasing 2DES maps at t_2 equal at 0, 200 and 600 fs.

The simulation of the 2D spectra reported on the bottom of figure 5.11 was performed following the general treatment of Mukamel's book [10] and reported in chapter 2. As will be deduced from the analysis of the coherent dynamics, two vibrational modes at 250 and 410 cm^{-1} are coupled to the electronic transition. In the simulation these modes can be modeled inserting two underdamped Brownian oscillators in the lineshape function $g(t)$ following the procedure described in reference [27]. In practice, this corresponds to consider the chromophore inside a bath that evolves randomly but at the same time contains some coherent fluctuations due to molecular vibrations. Due to the small coupling, the effect on the maps is very subtle, the coupled modes affect mainly the region below the diagonal and induce oscillations of the signal.

A selection of polymers 2DES maps is reported in figure 5.13. Despite the greater homogeneous disorder characterizing the polymeric samples, the elongation of the third order signal along the diagonal of the maps in figure 5.13 is comparable to the one of the monomer. This is the result of the filter effect induced by the limited laser bandwidth and we should be aware that we are not exciting all the states inside the Soret band. In these conditions, the comparison with the monomer data is even more important to deeply understand the polymer data. The 2DES spectra of P1 and P2 are again dominated by GSB and ES and a single central main feature is present. Inspecting in details the shape of the spectra, they are less symmetrical with respect to the diagonal when compared to the monomer ones. Especially P2 shows a bent shape and, as t_2 evolves, a gradual displacement of the signal from the top part to the lower part is recorded, meaning that a relaxation is happening. A small fraction of the higher excited states population is moving towards lower energy states. We can imagine that the small electronic coupling and the static disorder transform the vibronic states in a manifold of states.

Figure 5.14 shows selected decay traces of the real rephasing signal for all the samples. The overall decays of the maps is strongly correlated with the degree of coupling between the chromophoric units. The normalized decay traces extracted from the squared marker in panels (d,e,f) show that the ultrafast decay of the rephasing signal is much faster in P2 than P1 and M. The lower part of the maps are dominated by the coherent contributions manifested as oscillations of the signal, as shown in panels (g,h,i).

5.4.1 Fourier analysis

The coherent behavior of 2DES datasets can be analyzed after removing the decay contribution. A bi-exponential model satisfactorily reproduces the non-oscillating part of the signal of all samples, table 5.1 shows decay times and relative amplitudes.

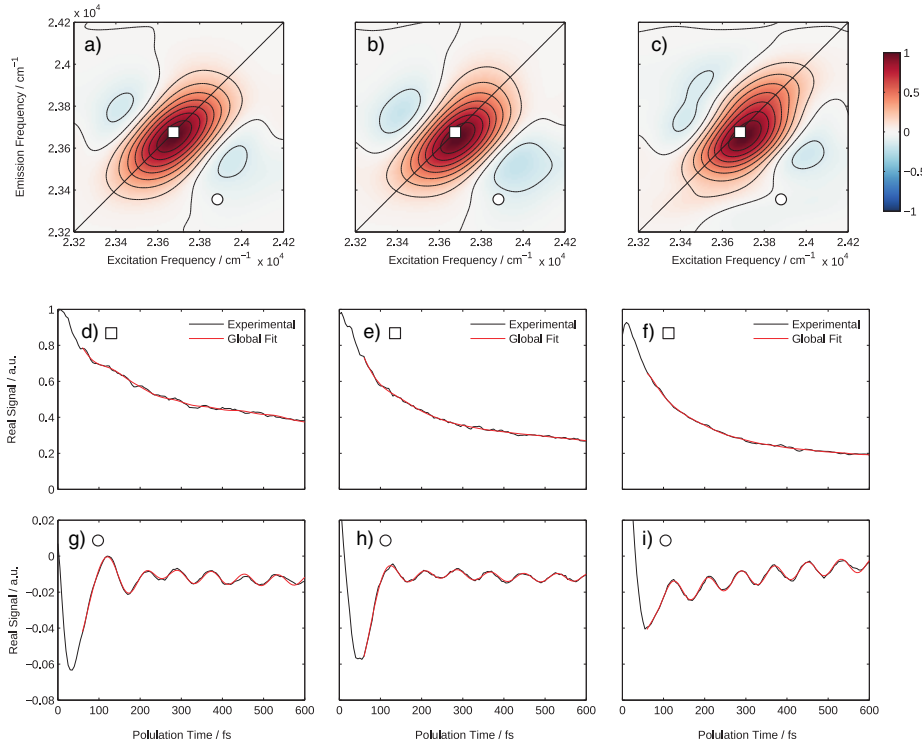

Figure 5.14: Signal decay traces along the population time extracted at selected coordinates of the maps. (a,b,c) Real rephasing 2DES maps at population time equal 100 fs for M, P1 and P2, respectively. (d,e,f) Decay traces extracted on the diagonal in correspondence of the maximum signal at points pinpointed with square markers. (g,h,i) Decay traces extracted on the lower part of the maps at coordinates identified with circle markers, where oscillating contributions dominate the signal. The global fit of the data using the method reported in section 4.3 is superimposed to the experimental data.

	M	P1	P2
τ_1 / ps	0.22 (59.4%)	0.094 (59.9%)	0.079 (64.1%)
τ_2 / ps	$\gg$1 (40.6%)	1.3 (40.1%)	0.80 (35.9%)

Table 5.1: Output parameters of the global fitting procedure described in section 4.3 applied to the rephasing data. A bi-exponential model is employed, and signal at population time below 50 fs has been discarded. The relative amplitude of the two components with time constants τ_1 and τ_2 are shown between brackets. Confidence intervals obtained from standard errors of the fit are in the order of 5% of the time constants.

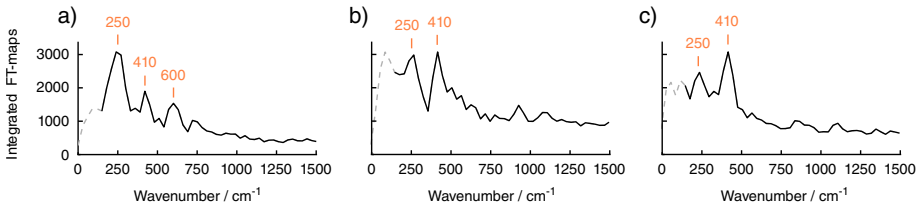

Figure 5.15: Integrated FT-maps of (a) M, (b) P1 and (c) P2.

The residuals of the bi-exponential fit contain the oscillating portion of the signal. Frequencies and amplitudes of the oscillations emerge after Fourier transforming along t_2. As already discussed in chapter 4, a three dimensional signal function of (ν_1, ν_2, ν_3) is obtained and it is typically explored as maps at fixed ν_2. In order to explain these signals, Feynman diagrams containing suitable coherences in the evolution time t_2 must be written down [28, 113].

An outlook of the main coherences evolving during t_2 comes from the integration of the Fourier maps along excitation and emission frequencies, these data are plotted in figure 5.15. Two main frequencies are present in all the samples: 250, 410 cm^{-1}; a 600 cm^{-1} component is also present in M. Peaks at frequencies higher than 600 cm^{-1} are not observed because of pulse bandwidth

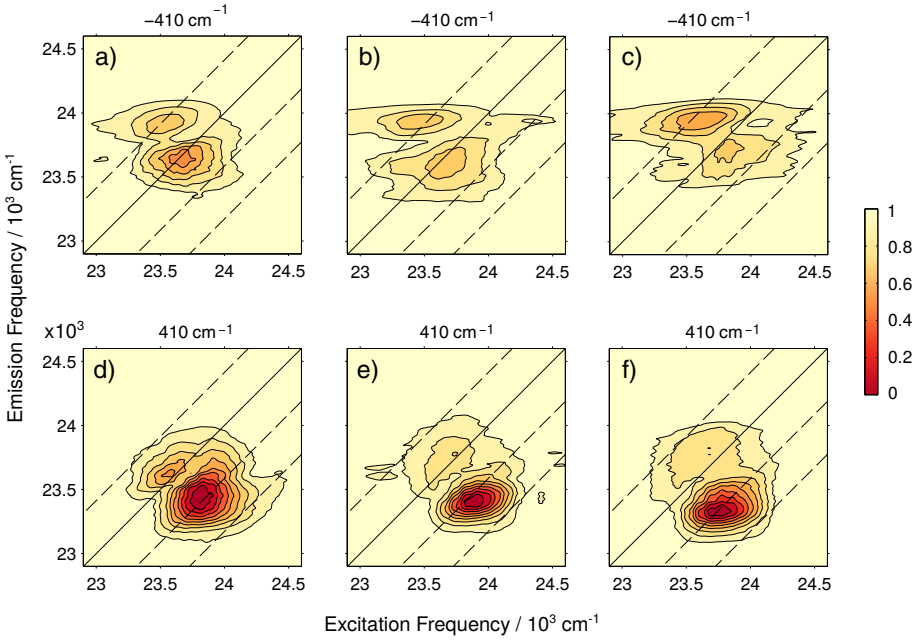

Figure 5.16: FT-maps of rephasing 2DES data at 410 cm^{-1} for (a,d) M, (b,e) P1 and (d,f) P2. (a,b,c) Negative and (d,e,f) positive frequencies contributions are shown.

restrictions. The laser is not able to excite coherences during the population time with an energy larger than its spectral width. The comparison of the plots in figure 5.15 shows that the relative amplitude of the frequency at 250 cm^{-1} with respect to the 410 cm^{-1} progressively decreases going from M to P1 to P2; at the same time the 600 cm^{-1} component vanishes below the noise level.

In the monomer case these coherences can be attributed to pure vibrational modes, in fact the Fourier maps associated with the found frequencies show the typical chair vibrational pattern. This specific pattern can be explained with a simple model in which the ground state and the excited state present

the same vibrational structure and a series of corresponding t_2-oscillating Feynman diagrams can be identified, the expected pattern is reported in figure 2.6. Fourier maps for the mode at 410 cm^{-1} are reported in figure 5.16, polymer maps resemble the monomer ones and thus the character of the modes is most likely still mainly vibrational.

5.4.2 Dephasing of coherences

The two vibrations coupled to the Soret transition at about 250 cm^{-1} and 410 cm^{-1} have rather different dynamic behaviors across the samples. Time-frequency analysis was employed in order to have a clear picture of the time evolution of the oscillating components; integrated SPWV plots are shown in figure 5.17.

The oscillations at 410 cm^{-1} are long lasting and shows a clear signature in the time-frequency plot for the full investigated time window of the experiment. On the contrary the oscillation centered at 250 cm^{-1} exhibits a much faster dynamics and it decays completely within 600 fs. A trend is clearly present ranging from M to P1 to P2: the higher the average coupling of the chromophores and the faster the damping time of this low frequency mode. The bandwidth of the features of the 250 cm^{-1} mode is also larger in polymers as a direct consequence of the time-frequency uncertainty principle.

Using the global analysis method described in section 4.3 the vibrational dephasing time was determinated for the two modes. The 410 cm^{-1} mode, lasting for the full time window of the experiment, has an exponential decay constant much larger than 600 fs. The 250 cm^{-1} mode presents decay constants of 87, 40 and 31 fs for M, P1 and P2, respectively; the standard error of the fit is estimated to be around 10 fs. Assuming a constant starting amplitude, a faster dephasing time implies a smaller amplitude in the Fourier transform, explaining the difference observed in figure 5.15. This trend is quite interesting because damping times encode information about the interaction with the

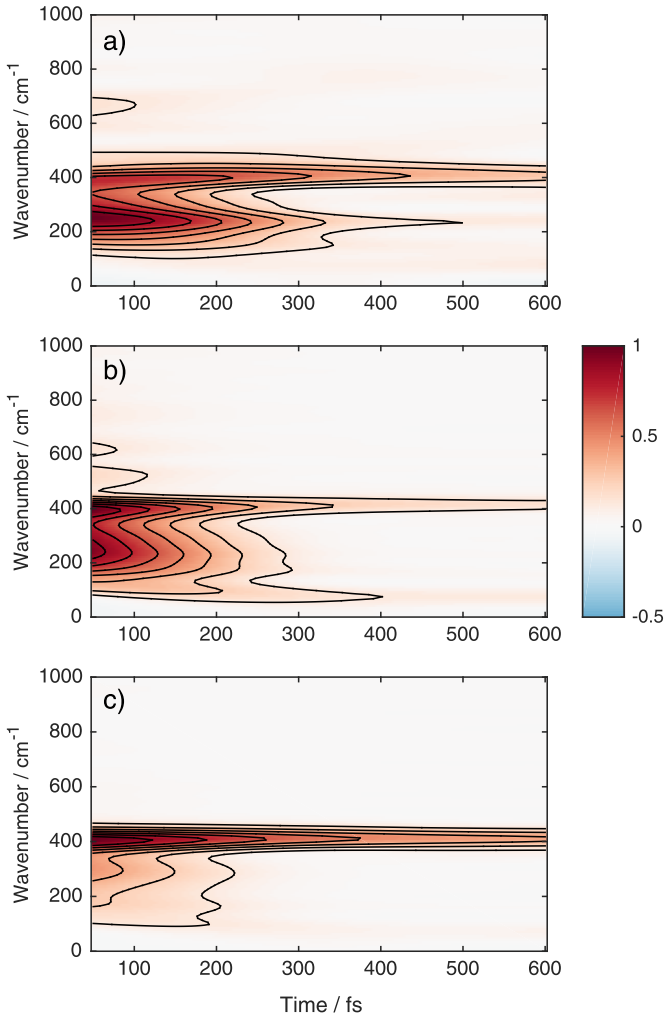

Figure 5.17: Normalized time-frequency transforms of the residuals of the bi-exponential fit for (a) M, (b) P1 and (c) P2. SPWV has been set with two identical Gaussian time windows with standard deviation of 100 fs. The four dimensional output of the time-frequency transform has been integrated along emission and excitation frequency in order to obtain bi-dimensional plots.

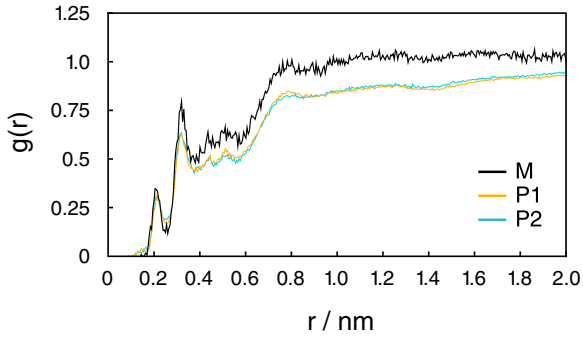

Figure 5.18: Average radial distribution function of the solvent around the Zn atom in all the samples.

environment and the degree of order of the system.

Coherent pump-probe studies with isotopically marked solvents suggested that, in metallated porphyrins, strongly damped low frequency modes are due to intermolecular vibrations involving clustered solvent molecules around the metal atom [135]. Most likely the 250 cm^{-1} mode can be assigned to such an intermolecular vibration involving one or more solvent molecules. To support this attribution, we verified the behavior of clustered solvent in the MD trajectories. In order to study the order of the solvent, the average radial distribution functions $g(r)$ of the THF molecules around the zinc atoms were calculated, they are reported in figure 5.18. A moderate difference in the radial distribution functions is present especially between monomer and polymers. The monomer exhibits more pronounced peaks at about 2.1 and 3.5 Å than polymers, suggesting that the solvent molecules can more easily self-organize around the metal center in the monomer form. Indeed, in polymers the solvent organization around the chromophoric units is hindered by the presence of the surrounding monomeric residues. This difference in the solvation order could support the different dephasing time in the samples. The higher the disorder

and the faster the damping of the observed coherence.

5.5 Discussion

Since the first application of 2DES spectroscopy to biological antenna systems, our knowledge about the factors regulating the relaxation and transport dynamics in complex multichromophoric systems is greatly advanced. 2DES spectroscopy with the help of increasingly refined and sophisticated analysis tools (some of them proposed in this thesis, see chapter 4) nowadays allows detecting details about relaxation dynamics with an unprecedented level of detail. The increasing complexity of the studied systems and of the level of information that can be extracted from the spectroscopic data requires more and more frequently also a corresponding increase in the complexity of the theoretical tools needed for the interpretation. In this work we interpret the 2DES data in the light of molecular dynamics simulations. The use of this approach has been motivated by the complexity of the studied systems and by their high level of disorder, preventing an easy application of quantum methodologies. Molecular dynamics simulation allows exploring properties of complex systems in the ground state. This is surely a drawback in this context since 2DES clearly captures excited state dynamics. Nevertheless, the obtained results are of great help in the interpretation of the data to quantitatively connect spectroscopic observables to the degree of disorder of the systems. To complement molecular dynamics simulations, in this work we also applied a simplified excitonic model, to grasp also the essential properties of the excited states modulated by the electronic coupling between chromophoric moieties. The results obtained applying this approach can be summarized in few relevant points:

(i) the data-analysis tools for the study of the coherent dynamics has given a clear overview of the experimental data. The mode at 410 cm^{-1} ap-

pears as a standard intramolecular vibrational mode which dephases in the picoseconds time-scale and which can be interpretated using the displaced harmonic oscillator model. The lower frequency mode at 250 cm^{-1} is characterized by a much faster dephasing dynamics with a clear trend in time constants going from M, to P1 to P2 (figure 5.17);

(ii) the excitonic model, used to reproduce the linear optical properties of the three samples, highlighted the presence of a higher excitonic coupling J for P2 (figure 5.4);

(iii) molecular dynamics simulations allowed quantitatively link this evidences to parameters describing the degree of disorder of the samples in terms of average chromophores distances, order parameters and correlation times (figure 5.9) as well in terms of the behavior of clustered solvent molecules possibly involved in the overall vibrational properties of the samples (figure 5.18).

All these evidences can find a common explanation with the argument outlined in figure 5.19. Panel (a) shows the distribution of the coupling constants for the three samples. As already discussed in section 5.2, the average value of the coupling J in both polymeric samples is such that the weak coupling regime can be easily invoked. Therefore we expect that, at least in average, the molecular vibrations are not affected by the exciton coupling and that the vibrational properties of the two polymers are not so dissimilar from the ones of the monomer. However, in polymers the disorder generates a multitude of conformations. Due to the non negligible amount of off-diagonal disorder, a fraction of the distribution of the chromophores are involved in particular conformations in which the exciton-vibrational resonance condition is fulfilled [34].

In order to correctly describe the energy level structure when the vibrational quanta and the exciton gap are comparable, a two-particle vibronic model is

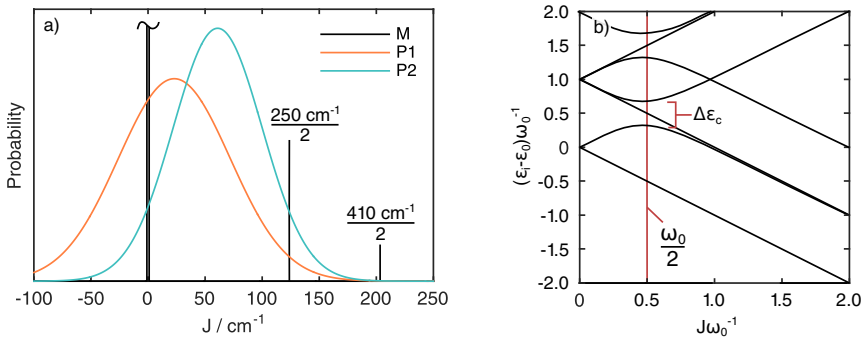

Figure 5.19: (a) Distributions of coupling constants among couples of chromophores obtained from the simulation of linear absorption spectra in section 5.2. For the monomer where by definition $J = 0$, the distribution is plotted as a Dirac delta function centred at 0. (b) Schematic representation of the energy levels of a vibronic dimer model in the two-particle approximation as a function of the coupling constant. The ith-level is labeled with the energy ϵ_i, the energy gap $\Delta\epsilon_c$ for the repelled level at the "crossing point" is highlighted in red. In the vicinity of the exciton-vibrational resonance, where $J = \omega_0/2$, new transitions with energy different from the vibrational quanta and the pure excitonic splitting are possible [35].

needed [35]. A schematic representation of the energy level of a vibronic dimer as a function of the coupling constant J is represented in figure 5.19 panel (b). When the coupling constant is in the vicinity of half the vibrational quanta, new transitions are possible between states with mixed character. For the vibrational mode at 250 cm^{-1} there is a significant population of chromophores couples having coupling constants close to half the vibrational quanta, greater for P2 than for P1. On the contrary, the population of chromophore couples with coupling constants in the vicinity of the exciton-vibrational resonance for the mode at 410 cm^{-1} is much smaller. This seems to suggest that the mode at 250

cm^{-1} dephases faster than the mode at 410 cm^{-1} also because, for a portion of chromophores population, the off-diagonal disorder generates a distribution of new mixed exciton-vibrational transitions. What these results are suggesting is that the presence of disorder can lead to very subtle effects on the vibrational and electronic properties of multi-chromophoric systems. This is probably not particularly critical in biological complexes, where the amount of disordered conformations is limited by the protein scaffold, keeping chromophores at right and relatively fixed distances and relative orientations. This issue become instead crucial in artificial systems, where the degree of disorder is surely less controlled.

Chapter 6

Conclusions

Ultrafast optical spectroscopy is a fascinating and rapidly evolving discipline. It is a landmark evidence of how cutting-edge technology in light manipulation can lead the progress of a research field unveiling new scenarios in our understanding of the world. It can be expected that new generations of laser sources and capable pulse-shapers will raise the bar even further, providing the tools to thin the fog obfuscating the role of quantum phenomena in Nature, possibly inspiring future technologies embedding quantum coherence and entanglement.

In this thesis, I have endeavored to present an effective and concise picture of my research, conducted during my three years PhD project. Coming from a theoretical chemistry formation, I have embraced the role of spectroscopist, branching my efforts between optical-hardware, data-analysis tools and the study of model systems. Most of my results were exploited by other components of the research group, highlighting the synergy at the basis of fruitful teamwork. All of these declinations of my research have been integral to my education and

growth as a scientist.

Recent experimental evidences of long-lived quantum electronic coherences in biological systems have stimulated a lot of interest in the scientific community. The field is source of strong debate and we are far from achieving clear statements. In this process, spectroscopy, and in particular multidimensional optical techniques, stands in the research and rationalization of evidences. Necessary requirements to achieve this aim are the development of increasingly capable instrumental setups able to guarantee reliable data and the research of advanced data-analysis tools able to expose and unravel the relevant piece of information.

During my project I worked on the construction of a compact and versatile 2D electronic spectroscopy (2DES) setup. Several aspects of the instrumental implementation needed to be finely tuned in order to assure the proper operation of the setup and the high quality of the data. The main challenge of a 2DES implementation is creating and delivering the appropriate pulse sequence with variable and phase-stable time delays. To this aim, I developed new sophisticated calibration routines able to guarantee an accurate timing of the pulses. A pulse-shaper stage, made by an acousto-optic programmable dispersive filter and a prism compressor, was fully integrated allowing for great flexibility in pulse compression and leading to ultrashort pulses — in the best cases shorter than 10 fs. As a direct consequence, high time resolution and signal-to-noise ratio were attained. Experiment routines were implemented to assure concerted execution of the functions of every piece of the equipment. These include a double modulation lock-in acquisition scheme able to suppress spurious signals, and an autonomous and programmable routine of experiment design able to accomplish independently several pulse schemes.

The exploration and the development of data-analysis tools able to reveal the dynamics of the quantum coherences excited during 2DES experiments, are critical but deficient subjects in literature. In this dissertation several strate-

gies have been presented to fill these gaps. Time-frequency decomposition techniques, borrowed from the signal-processing field, have been adapted and applied to the analysis of 2DES oscillating signals [65]. While the Fourier-analysis techniques available so far analyze the signals in the frequency domain, the time-frequency transforms proposed in this thesis can instead provide joint frequency and time resolution, unveiling the dynamics of the relevant beating components. Since time-frequency analysis is a mature field that compromises of several approaches, adapted in the last decades to be efficient in different technical areas, an optimization and selection procedure has been developed in order to objectively pick out the most performing transform. It was concluded that Smoothed-pseudo-Wigner-Ville distribution is the most efficient time-frequency approach for the investigation of damped oscillation in typical 2DES signals.

In addition, I proposed a global analysis method based on the variable projection algorithm, which is able to reproduce simultaneously coherence and population dynamics of rephasing and non-rephasing contributions [93]. This approach has several advantages if compared to the currently available methods for the analysis of 2DES spectra. The first remarkable feature is the simultaneous access to both the non-oscillating and oscillating dynamics in a unique step of analysis, while most of the previously proposed methods need separated and sequential treatments of the decaying part and of the beating part of the signal. Moreover the global character of the method provides unmatched robust and quantitative evaluation of damping times of coherences and relative associated spectra. Test measures at room temperature on a standard dye were used to validate the procedure.

A model multi-chromophoric system, based on a methacrylic linear oligomer with Zinc-tetraphenylporphyrins on side-chains, has been investigated. Two differently constructed polymers, with or without a spacer between the chromophore and the backbone, were considered; the monomeric systems were

also studied as a control. Linear absorption spectroscopy shows significant differences only in the Soret bands, which were simulated using an effective Hamiltonian with nearest neighbor interactions between the chromophores. Small coupling constants of about tens of cm^{-1} classify the systems in the weak-coupling regime where the intramolecular vibrational structure is mostly retained. Fully atomistic molecular dynamics simulations suggest very disordered conformational properties and confirm the high flexibility of these systems. In 2DES experiments on the Soret band, the high disorder prevented the observation of any coherent signature of purely electronic nature, shifting our focus on the vibrational coherence dissimilarity between the samples. Two vibrational modes coupled to the optical transition presented drastically different properties. A long lasting intramolecular mode is essentially unchanged in every sample. A strongly damped intermolecular vibration, involving clustered solvent molecules, was found to be correlated to the salvation order around the Zinc atom. Molecular dynamics simulations were exploited to calculate the radial distribution function of the solvent and evaluate order properties. In particular we found that the dephasing times in different samples are the results of a complex interplay between (i) excitonic coupling, (ii) width of the disorder distribution, (iii) frequency of the vibrational mode and (iv) its possible delocalization over clustered solvent molecules. These are the first evidences trying to quantify the important role of the environment in modulating ultrafast coherent dynamics of complex systems.

In my three years PhD project I had the opportunity to work in a very active field where promising stimuli underlie exciting future developments. Pulse shaping based implementation of 2DES in pump-probe geometry is gaining a lot of attention due to the great simplification in the optical setup and the elevate phase stability it can guarantee. The crucial step is increasing signal-to-noise ratio, which is low because of the non-background-free detection. Mixed BOXCARS and pump-probe geometry setups have been already proposed to

solve this problem [136]; evolution of these first examples of implementation will allow the development of new generation of simple and compact 2DES spectrometers that will facilitate the introduction of the first commercial versions. Improved versions of the proposed data-analysis approaches are currently under research, the aim is to unleash the full 2DES spectra potential to unravel the complete dynamics of complex systems. The first step of this process is the implementation of a global analysis method allowing the use of complex kinetics schemes. Moreover, the study of model systems will allow in the next years to understand more of the role of quantum coherence in energy transport processes. Using different variations of the systems for the systematic evaluation of the influence of solvent and environment on the coherent response will be crucial in the research progress.

List of Abbreviations

2DES	Two-dimensional electronic spectroscopy
2Q	Double-quantum signal
AOPDF	Acousto-optic programmable dispersive filter
CAS	Coherence associated spectra
CCD	Carge-coupled device
CW	Choi-Williams distribution
CWT	Continuous wavelet transform
DAS	Decay associated spectra
DOE	Diffractive optic element
DQC	Double quantum coherence
ESA	Excited state absorption
FROG	Frequency-resolved optical gating
FT	Fourier transform
GSB	Ground state bleaching

HR	Huang-Rhys factor
LO	Local oscillator
MD	Molecular dynamics
NR	Non-rephasing signal
PWV	Pseudo-Wigner-Ville distribution
R	Rephasing signal
RF	Rotating frame
RWA	Rotating wave approximation
SCW	Smoothed Choi-Williams distribution
SE	Stimulated emission
SI	Spectral interference
SPWV	Smoothed pseudo-Wigner-Ville distribution
STFT	Short time Fourier transform
TL	Transform-limited
WP	Wedge pair
WV	Wigner-Ville distribution

Bibliography

[1] K. Southwell. Quantum coherence. *Nature*, 453:1003, 2008.

[2] R. Blatt and D. Wineland. Entangled states of trapped atomic ions. *Nature*, 453:1008–1015, 2008.

[3] J. I. Cirac and P. Zoller. Quantum computations with cold trapped ions. *Physical Review Letters*, 74(20):4091–4094, 1995.

[4] G. D. Scholes. Quantum-coherent electronic energy transfer: Did nature think of it first? *Journal of Physical Chemistry Letters*, 1:2–8, 2010.

[5] G. D. Scholes, G. R. Fleming, A. Olaya-Castro, and R. van Grondelle. Lessons from nature about solar light harvesting. *Nature Chemistry*, 3(10):763–774, 2011.

[6] A. Chenu and G. D. Scholes. Coherence in energy transfer and photosynthesis. *Annual Review of Physical Chemistry*, 66:69–96, 2015.

[7] S. F. Huelga and M. B. Plenio. Vibrations, quanta and biology. *Contemporary Physics*, 54(4):181–207, 2013.

[8] P. Ball. Physics of life: The dawn of quantum biology. *Nature*, 474:272–274, 2011.

[9] D. M. Jonas. Two-dimensional femtosecond spectroscopy. *Annual Review of Physical Chemistry*, 54:425–463, 2003.

[10] S. Mukamel. *Principles of Nonlinear Optical Spectroscopy*. Oxford University Press, 1999.

[11] G. S. Engel, T. R. Calhoun, E. L. Read, T.-K. Ahn, T. Mancal, Y.-C. Cheng, R. E. Blankenship, and G. R. Fleming. Evidence for wavelike energy transfer through quantum coherence in photosynthetic systems. *Nature*, 446:782–786, 2007.

[12] E. Collini, C. Y. Wong, K. E. Wilk, P. M. G. Curmi, P. Brumer, and G. D. Scholes. Coherently wired light-harvesting in photosynthetic marine algae at ambient temperature. *Nature*, 463:644–647, 2010.

[13] F. D. Fuller, J. Pan, A. Gelzinis, V. Butkus, S. S. Senlik, D. E. Wilcox, C. F. Yocum, L. Valkunas, D. Abramavicius, and J. P. Ogilvie. Vibronic coherence in oxygenic photosynthesis. *Nature Chemistry*, 6:706–711, 2014.

[14] E. Romero, R. Augulis, V. I. Novoderezhkin, M. Ferretti, J. Thieme, D. Zigmantas, and R. van Grondelle. Quantum coherence in photosynthesis for efficient solar-energy conversion. *Nature Physics*, 10:676–682, 2014.

[15] J. Kempe. Quantum random walks: An introductory overview. *Contemporary Physics*, 44(4):307–327, 2003.

[16] E. Collini. Spectroscopic signatures of quantum-coherent energy transfer. *Chemical Society Reviews*, 42:4932–4947, 2013.

[17] J. Lim, D. Palecek, F. Caycedo-Soler, C. N. Lincoln, J. Prior, H. V. Berlepsch, S. F. Huelga, M. B. Plenio, D. Zigmantas, and J. Hauer. Vibronic origin of long-lived coherence in an artificial molecular light harvester. *Nature Communications*, 6(7755):1–7, 2015.

[18] S. M. Falke, C. A. Rozzi, D. Brida, M. Maiuri, M. Amato, E. Sommer, A. De Sio, A. Rubio, G. Cerullo, E. Molinari, and C. Lienau. Coherent ultrafast charge transfer in an organic photovoltaic blend. *Science*, 344(6187):1001–1005, 2014.

[19] A. A. Bakulin, S. E. Morgan, T. B. Kehoe, M. W. B. Wilson, A. W. Chin, D. Zigmantas, D. Egorova, and A. Rao. Real-time observation of multiexcitonic states in ultrafast singlet fission using coherent 2D electronic spectroscopy. *Nature Chemistry*, 8:16–23, 2016.

[20] A. De Sio, F. Troiani, M. Maiuri, J. Réhault, E. Sommer, J. Lim, S. F. Huelga, M. B. Plenio, C. A. Rozzi, G. Cerullo, E. Molinari, and C. Lienau. Tracking the coherent generation of polaron pairs in conjugated polymers. *Nature Communications*, 7(13742):1–8, 2016.

[21] C. A. Rozzi, S. M. Falke, N. Spallanzani, A. Rubio, E. Molinari, D. Brida, M. Maiuri, G. Cerullo, H. Schramm, J. Christoffers, and C. Lienau. Quantum coherence controls the charge separation in a prototypical artificial light harvesting system. *Nature Communications*, 4(1602):1–7, 2013.

[22] M. Cho. *Two-Dimensional Optical Spectroscopy*. CRC Press, 2009.

[23] F. D. Fuller and J. P. Ogilvie. Experimental implementations of two-dimensional fourier transform electronic spectroscopy. *Annual Review of Physical Chemistry*, 66:667–90, 2015.

[24] L. Valkunas, D. Abramavicius, and T. Mančal. *Molecular Excitation Dynamics and Relaxation*. Wiley-VCH, 2013.

[25] R. W. Boyd. *Nonlinear Optics*. Elsevier, third edition, 2008.

[26] J. R. Caram, A. F. Fidler, and G. S. Engel. Excited and ground state vibrational dynamics revealed by two-dimensional electronic spectroscopy. *Journal of Chemical Physics*, 137(024507):1–10, 2012.

[27] V. Butkus, L. Valkunas, and D. Abramavicius. Molecular vibrations-induced quantum beats in two-dimensional electronic spectroscopy. *The Journal of Chemical Physics*, 137(044513):1–9, 2012.

[28] V. Butkus, D. Zigmantas, L. Valkunas, and D. Abramavicius. Vibrational vs. electronic coherences in 2D spectrum of molecular systems. *Chemical Physics Letters*, 545:40–43, 2012.

[29] D. B. Turner, K. E. Wilk, P. M. G. Curmi, and G. D. Scholes. Comparison of electronic and vibrational coherence measured by two-dimensional electronic spectroscopy. *Journal of Physical Chemistry Letters*, 2:1904–1911, 2011.

[30] V. Butkus, D. Zigmantas, D. Abramavicius, and L. Valkunas. Distinctive character of electronic and vibrational coherences in disordered molecular aggregates. *Chemical Physics Letters*, 587:93–98, 2013.

[31] V. Perlík, C. Lincoln, F. Šanda, and J. Hauer. Distinguishing electronic and vibronic coherence in 2D spectra by their temperature dependence. *Journal of Physical Chemistry Letters*, 5:404–407, 2014.

[32] F. V. A. Camargo, L. Grimmelsmann, L. Anderson, S. R. Meech, and I. A. Heisler. Resolving vibrational from electronic coherences in two-dimensional electronic spectroscopy: the role of the laser spectrum. *Physical Review Letters*, 118(033001):1–6, 2017.

[33] F. Milota, V. I. Prokhorenko, T. Mancal, H. von Berlepsch, O. Bixner, H. F. Kauffmann, and J. Hauer. Vibronic and vibrational coherences in two-dimensional electronic spectra of supramolecular j-aggregates. *The Journal of Physical Chemistry A*, 117:6007–14, 2013.

[34] V. Butkus, L. Valkunas, and D. Abramavicius. Vibronic phenomena and exciton-vibrational interference in two-dimensional spectra of molecular aggregates. *The Journal of Chemical Physics*, 140(034306):1–15, 2014.

[35] E. Bašinskaite, V. Butkus, D. Abramavicius, and L. Valkunas. Vibronic models for nonlinear spectroscopy simulations. *Photosynthesis Research*, 121:95–106, 2014.

[36] S. T. Cundiff. Optical three dimensional coherent spectroscopy. *Physical Chemistry Chemical Physics*, 16:8193–200, 2014.

[37] J. A. Myers, K. L. M. Lewis, P. F. Tekavec, and J. P. Ogilvie. Two-color two-dimensional Fourier transform electronic spectroscopy with a pulse-shaper. *Optics Express*, 16(22):17420–17428, 2008.

[38] P. F. Tekavec, J. A. Myers, K. L. M. Lewis, and J. P. Ogilvie. Two-dimensional electronic spectroscopy with a continuum probe. *Optics Letters*, 34(9):1390–1392, 2009.

[39] P. F. Tian, D. Keusters, Y. Suzaki, and W. S. Warren. Femtosecond phase-coherent two-dimensional spectroscopy. *Science*, 300:1553–1555, 2003.

[40] I. A. Heisler, R. Moca, F. V. A. Camargo, and S. R. Meech. Two-dimensional electronic spectroscopy based on conventional optics and fast dual chopper data acquisition. *Review of Scientific Instruments*, 85(063103):1–10, 2014.

[41] M. D. Levenson and G. L. Eesley. Polarization selective optical heterodyne detection for dramatically improved sensitivity in laser spectroscopy. *Applied Physics*, 19:1–17, 1979.

[42] L. Lepetit, G. Chériaux, and M. Joffre. Linear techniques of phase measurement by femtosecond spectral interferometry for applications in

spectroscopy. *Journal of the Optical Society of America B*, 12(12):2467–2474, 1995.

[43] A. Nemeth, J. Sperling, J. Hauer, H. F. Kauffmann, and F. Milota. Compact phase-stable design for single- and double-quantum two-dimensional electronic spectroscopy. *Optics Letters*, 34(21):3301–3303, 2009.

[44] D. Milam, M. J. Weber, and A. J. Glass. Nonlinear refractive index of fluoride crystals. *Applied Physics Letters*, 31(12):822–825, 1977.

[45] R. Augulis and D. Zigmantas. Two-dimensional electronic spectroscopy with double modulation lock-in detection: enhancement of sensitivity and noise resistance. *Optics Express*, 19(14):13126–13133, 2011.

[46] K. W. DeLong, R. Trebino, and D. J. Kane. Comparison of ultrashort-pulse frequency-resolved-optical-gating traces for three common beam geometries. *Journal of the Optical Society of America B*, 11(9):1595–1608, 1994.

[47] W. Dietel, J. J. Fontaine, and J.-C. Diels. Intracavity pulse compression with glass: a new method of generating pulses shorter than 60 fsec. *Optics Letters*, 8(1):4–6, 1983.

[48] R. L. Fork, O. E. Martinez, and J. P. Gordon. Negative dispersion using pairs of prisms. *Optics Letters*, 9(5):150, 1984.

[49] D. J. Kane and R. Trebino. Characterization of arbitrary femtosecond pulses using frequency-resolved optical gating. *IEEE Journal of Quantum Electronics*, 29(2):571–579, 1993.

[50] T. Tsang, M. A. Krumbügel, K. W. Delong, D. N. Fittinghoff, and R. Trebino. Frequency-resolved optical-gating measurements of ultrashort pulses using surface third-harmonic generation. *Optics Letters*, 21(17):1381–1383, 1996.

[51] S. L. Marple. Computing the discrete-time “analytic” signal via FFT. *IEEE Transactions on Signal Processing*, 47(9):2600–2603, 1999.

[52] J. Mooney and P. Kambhampati. Get the basics right: Jacobian conversion of wavelength and energy scales for quantitative analysis of emission spectra. *The Journal of Physical Chemistry Letters*, 4(19):3316–3318, 2013.

[53] S.-H. Shim and M. T. Zanni. How to turn your pump-probe instrument into a multidimensional spectrometer: 2D IR and Vis spectroscopies via pulse shaping. *Physical Chemistry Chemical Physics*, 11(5):748–761, 2009.

[54] T. Brixner, T. Manal, I. V. Stiopkin, and G. R. Fleming. Phase-stabilized two-dimensional electronic spectroscopy. *Journal of Chemical Physics*, 121(9):4221–4236, 2004.

[55] I. H. M. Van Stokkum, D. S. Larsen, and R. van Grondelle. Global and target analysis of time-resolved spectra. *Biochimica et Biophysica Acta - Bioenergetics*, 1657:82–104, 2004.

[56] J. Dostál, J. Pšenčík, and D. Zigmantas. In situ mapping of the energy flow through the entire photosynthetic apparatus. *Nature Chemistry*, 8:705–710, 2016.

[57] F. V. A. Camargo, H. L. Anderson, S. R. Meech, and I. A. Heisler. Time-resolved twisting dynamics in a porphyrin dimer characterized by two-dimensional electronic spectroscopy. *The Journal of Physical Chemistry B*, 119:14660–14667, 2015.

[58] D. B. Turner, K. W. Stone, K. Gundogdu, and K. A. Nelson. Three-dimensional electronic spectroscopy of excitons in GaAs quantum wells. *Journal of Chemical Physics*, 131(144510):1–8, 2009.

[59] H. Li, A. D. Bristow, M. E. Siemens, G. Moody, and S. T. Cundiff. Unraveling quantum pathways using optical 3D Fourier-transform spectroscopy. *Nature Communications*, 4(1390):1–9, 2013.

[60] J. O. Tollerud, S. T. Cundiff, and J. A. Davis. Revealing and characterizing dark excitons through coherent multidimensional spectroscopy. *Physical Review Letters*, 117(097401):1–6, 2016.

[61] J. Tang and J. R. Norris. LPZ spectral analysis using linear prediction and the z-transform. *The Journal of Chemical Physics*, 84(9):5210–5211, 1986.

[62] G. Panitchayangkoon, D. V. Voronine, D. Abramavicius, J. R. Caram, N. H. C. Lewis, S. Mukamel, and G. S. Engel. Direct evidence of quantum transport in photosynthetic light-harvesting complexes. *Proceedings of the National Academy of Sciences of the United States of America*, 108(52):20908–20912, 2011.

[63] J. R. Caram and G. S. Engel. Extracting dynamics of excitonic coherences in congested spectra of photosynthetic light harvesting antenna complexes. *Faraday Discussions*, 153:93–104, 2011.

[64] J. Prior, E. Castro, A. W. Chin, J. Almeida, S. F. Huelga, and M. B. Plenio. Wavelet analysis of molecular dynamics: Efficient extraction of time-frequency information in ultrafast optical processes. *The Journal of Chemical Physics*, 139:224103, 2013.

[65] A. Volpato and E. Collini. Time-frequency methods for coherent spectroscopy. *Optics Express*, 23(15):20040–20050, 2015.

[66] X. Wu and T. Liu. Spectral decomposition of seismic data with reassigned smoothed pseudo Wigner-Ville distribution. *Journal of Applied Geophysics*, 68(3):386–393, 2009.

[67] E. P. De Souza Neto, M. Custaud, J. Frutoso, L. Somody, C. Gharib, and J. O. Fortrat. Smoothed pseudo Wigner-Ville distribution as an alternative to Fourier transform in rats. *Autonomic Neuroscience: Basic and Clinical*, 87:258–267, 2001.

[68] J. L. Tan and A. Z. B. Sha'ameri. Signal analysis and classification of digital communication signals using adaptive smooth-windowed Wigner-Ville distribution. In *Proceedings of IEEE Conference on Telecommunication Technologies*, pages 260–266, 2008.

[69] M. J. J. Vrakking, D. M. Villeneuve, and A. Stolow. Observation of fractional revivals of a molecular wave packet. *Physical Review A*, 54(1):R37–R40, 1996.

[70] T. Fuji, T. Saito, and T. Kobayashi. Dynamical observation of Duschinsky rotation by sub-5-fs real-time spectroscopy. *Chemica Physics Letters*, 332:324–330, 2000.

[71] D. Hasegawa, K. Nakata, E. Tokunaga, K. Okamura, J. Du, and T. Kobayashi. Vibrational energy flow between modes by dynamic mode coupling in THIATS J-aggregates. *The Journal of Physical Chemistry A*, 117:11441–11448, 2013.

[72] T. Kobayashi and A. Yabushita. Transition-state spectroscopy using ultrashort laser pulses. *The Chemical Record*, 11(2):99–116, 2011.

[73] A. Yabushita and T. Kobayashi. Primary conformation change in bacteriorhodopsin on photoexcitation. *Biophysical Journal*, 96(4):1447–1461, 2009.

[74] L. Cohen. *Time-Frequency Analysis: Theory and Applications*. Prentice-Hall, 1995.

[75] C. H. Page. Instantaneous power spectra. *Journal of Applied Physics*, 23(1):103–106, 1952.

[76] A. W. Rihaczek. Signal energy distribution in time and frequency. *IEEE Transactions on Information Theory*, 14(3):369–374, 1968.

[77] L. Cohen. Time-frequency distributions - A review. *Proceedings of the IEEE*, 77(7):941–981, 1989.

[78] Y. Zhao, L. E. Atlas, and R. J. Marks. The use of cone shaped kernels for generalized time-frequency representation of nonstationary signals. *IEEE Transactions on Acoustics, Speech, and Signal Processing*, 38(7):1084–1091, 1990.

[79] D. Gabor. Theory of communication. Part 1: The analysis of information. *Journal of the Institution of Electrical Engineers - Part III: Radio and Communication Engineering*, 93(26):429–441, 1946.

[80] V. C. Chen and H. Ling. *Time-Frequency Transforms for radar imaging And Signal Analysis*. Artech House Boston London, 2002.

[81] R. D. Hippenstiel and P. M. de Oliveira. Time-varying spectral estimation using the instantaneous power spectrum (IPS). *IEEE Transactions on Acoustics, Speech, and Signal Processing*, 38(10):1752–1759, 1990.

[82] H. Margenau and R. Hill. Correlation between measurements in quantum theory. *Progress of Theroretical Physiscs*, 26(5):722–738, 1961.

[83] E. Wigner. On the quantum correction for thermodynamic equilibrium. *Physical Review*, 40(5):749–759, 1932.

[84] J. Ville. Théorie et applications de la notion de signal analytique. *Cable et Transmissions*, 2A:61–74, 1958.

[85] L. Cohen. Generalized phase-space distribution functions. *Journal of Mathematical Physics*, 7(5):781–786, 1966.

[86] F. Hlawatsch, T. G. Manickam, R. L. Urbanke, and W. Jones. Smoothed pseudo-Wigner distribution, Choi-Williams distribution, and cone-kernel representation: Ambiguity-domain analysis and experimental comparison. *Signal Processing*, 43(2):149–168, 1995.

[87] H.-I. Choi and W. J. Williams. Improved time-frequency representation of multicomponent signals using exponential kernels. *IEEE Transactions on Acoustics, Speech, and Signal Processing*, 37(6):862–871, 1989.

[88] M. Cho. Coherent two-dimensional optical spectroscopy. *Chemical Reviews*, 108(4):1331–1418, 2008.

[89] S. Qian and D. Chen. Joint time-frequency analysis. *IEEE Signal Processing Magazine*, 16(2):52–67, 1999.

[90] D. Wu and J. M. Morris. Time-frequency representations using a radial Butterworth kernel. *International Symposium on Time-Frequency and Time-Scale Analysis*, pages 60–63, 1994.

[91] J. Almeida, J. Prior, and M. B. Plenio. Computation of two-dimensional spectra assisted by compressed sampling. *Journal of Physical Chemistry Letters*, 3(18):2692–2696, 2012.

[92] D. Garcia. Robust smoothing of gridded data in one and higher dimensions with missing values. *Computational Statistics and Data Analysis*, 54(4):1167–1178, 2010.

[93] A. Volpato, L. Bolzonello, E. Meneghin, and E. Collini. Global analysis of coherence and population dynamics in 2D electronic spectroscopy. *Optics Express*, 24(21):24773–24785, 2016.

[94] M. R. Osborne. Some special nonlinear least squares problems. *SIAM Journal on Numerical Analysis*, 12(4):571–592, 1975.

[95] D. Kundu. A modified prony algorithm for sum of damped or undamped exponential signals. *Sankhyā: The Indian Journal of Statistics*, 56(B-3):524–544, 1994.

[96] M. R. Osborne and G. K. Smyth. A modified prony algorithm for exponential function fitting. *SIAM Journal on Scientific Computing*, 16(1):119–138, 1995.

[97] C. Ruckebusch, M. Sliwa, P. Pernot, A. de Juan, and R. Tauler. Comprehensive data analysis of femtosecond transient absorption spectra: A review. *Journal of Photochemistry and Photobiology C: Photochemistry Reviews*, 13(1):1–27, 2012.

[98] G. H. Golub and V. Pereyra. The differentiation of pseudo-inverses and nonlinear least squares roblems whose variables separate. *SIAM Journal on Numerical Analysis*, 10(2):413–432, 1973.

[99] G. Golub and V. Pereyra. Separable nonlinear least squares: the variable projection method and its applications. *Inverse Problems*, 19(2):R1–R26, 2003.

[100] D. P. O'Leary and B. W. Rust. Variable projection for nonlinear least squares problems. *Computational Optimization and Applications*, 54(3):579–593, 2013.

[101] K. M. Mullen, M. Vengris, and I. H. M. van Stokkum. Algorithms for separable nonlinear least squares with application to modelling time-resolved spectra. *Journal of Global Optimization*, 38(2):201–213, 2007.

[102] K. M. Mullen and I. H. M. van Stokkum. The variable projection algorithm in time-resolved spectroscopy, microscopy and mass spectrometry applications. *Numerical Algorithms*, 51:319–340, 2009.

[103] G. H. Golub and C. F. V. Loan. *Matrix Computations*. The John Hopkins University Press, 2012.

[104] E. E. Ostroumov, R. M. Mulvaney, J. M. Anna, R. J. Cogdell, and G. D. Scholes. Energy transfer pathways in light-harvesting complexes of purple bacteria as revealed by global kinetic analysis of two-dimensional transient spectra. *The Journal of Physical Chemistry B*, 117:11349–11362, 2013.

[105] T. R. Senty, S. K. Cushing, C. Wang, C. Matranga, and A. D. Bristow. Inverting transient absorption data to determine transfer rates in quantum dot-TiO2 heterostructures. *The Journal of Physical Chemistry C*, 119:6337–6343, 2015.

[106] R. W. Hendler and R. I. Shrager. Deconvolutions based on singular value decomposition and the pseudoinverse: a guide for beginners. *Journal of Biochemical and Biophysical Methods*, 28:1–33, 1994.

[107] E. R. Henry and J. Hofrichter. Singular Value Decomposition: Application to Analysis of Experimental Data. *Methods in Enzymology*, 210(1973):129–192, 1985.

[108] H. J. Motulsky and A. Christopoulos. *Fitting models to biological data using linear and nonlinear regression*. GraphPad Software, Inc., San Diego, 2003.

[109] H. Ohtani, T. Kobayashi, T. Ohno, S. Kato, T. Tanno, and A. Yamadae. Nanosecond spectroscopy on the mechanism of the reduction of

methylviologen 4431 sensitized by metallophthalocyanine. *The Journal of Physical Chemistry*, 88:4431–4435, 1984.

[110] J. Savolainen, D. van der Linden, N. Dijkhuizen, and J. L. Herek. Characterizing the functional dynamics of zinc phthalocyanine from femtoseconds to nanoseconds. *Journal of Photochemistry and Photobiology A: Chemistry*, 196:99–105, 2008.

[111] F. V. A. Camargo, H. L. Anderson, S. R. Meech, and I. A. Heisler. Full characterization of vibrational coherence in a porphyrin chromophore by two-dimensional electronic spectroscopy. *The Journal of Physical Chemistry A*, 119:95–101, 2015.

[112] R. Singh, G. Moody, M. E. Siemens, H. Li, and S. T. Cundiff. Quantifying spectral diffusion by the direct measurement of the correlation function for excitons in semiconductor quantum wells. *Journal of the Optical Society of America B*, 33(7):C137–143, 2016.

[113] D. B. Turner, R. Dinshaw, K.-K. Lee, M. S. Belsley, K. E. Wilk, P. M. G. Curmi, and G. D. Scholes. Quantitative investigations of quantum coherence for a light-harvesting protein at conditions simulating photosynthesis. *Physical Chemistry Chemical Physics*, 14:4857–4874, 2012.

[114] K. A. Fransted, J. R. Caram, D. Hayes, and G. S. Engel. Two-dimensional electronic spectroscopy of bacteriochlorophyll a in solution: Elucidating the coherence dynamics of the Fenna-Matthews-Olson complex using its chromophore as a control. *The Journal of Chemical Physics*, 137(125101):1–9, 2012.

[115] D. Hayes, G. B. Griffin, and G. S. Engel. Response to Comment on "Engineering coherence among excited states in synthetic heterodimer systems". *Science*, 340:1431–1434, 2013.

[116] A. Halpin, P. J. M. Johnson, R. Tempelaar, R. S. Murphy, J. Knoester, T. L. C. Jansen, and R. J. D. Miller. Two-dimensional spectroscopy of a molecular dimer unveils the effects of vibronic coupling on exciton coherences. *Nature Chemistry*, 6:196–201, 2014.

[117] A. G. Marshall and F. R. Verdun. *Fourier Transforms in NMR, Optical and Mass Spectrometry*. Elsevier, 1990.

[118] L. Angiolini, T. Benelli, and L. Giorgini. Novel optically active methacrylic polymers containing side-chain porphyrin moieties for chiral recognition. *Polymer*, 52:2747–2756, 2011.

[119] L. Angiolini, T. Benelli, and L. Giorgini. Polymethacrylic zinc porphyrin: A new approach to chiral recognition. *Reactive & Functional Polymers*, 71:204–209, 2011.

[120] B. R. Green and W. W. Parson. *Light-Harvesting Antennas in Photosynthesis*. Springer Netherlands, 2003.

[121] M. Senge, A. Ryan, K. Letchford, S. MacGowan, and T. Mielke. Chlorophylls, symmetry, chirality, and photosynthesis. *Symmetry*, 6:781–843, 2014.

[122] M. Gouterman, G. H. Wagnière, and L. C. Snyder. Spectra of porphyrins. Part II. Four orbital model. *Journal of Molecular Spectroscopy*, 11:108–127, 1963.

[123] M. Gouterman. Spectra of porphyrins. *Journal of Molecular Spectroscopy*, 6:138–163, 1961.

[124] K. Huang and A. Rhys. Theory of light absorption and non-radiative transitions in F-centres. *Proceedings of the Royal Society of London. Series A. Mathematical and Physical Sciences*, 204:406–423, 1950.

[125] F. C. Spano, J. Clark, C. Silva, and R. H. Friend. Determining exciton coherence from the photoluminescence spectral line shape in poly(3-hexylthiophene) thin films. *The Journal of Chemical Physics*, 130(074904):1–16, 2009.

[126] F. C. Spano. The spectral signatures of frenkel polarons in H- And J-aggregates. *Accounts of Chemical Research*, 43(3):429–439, 2010.

[127] A. D. MacKerell, D. Bashford, M. Bellott, R. L. Dunbrack, J. D. Evanseck, M. J. Field, S. Fischer, J. Gao, H. Guo, S. Ha, D. Joseph-McCarthy, L. Kuchnir, K. Kuczera, F. T. Lau, C. Mattos, S. Michnick, T. Ngo, D. T. Nguyen, B. Prodhom, W. E. Reiher, B. Roux, M. Schlenkrich, J. C. Smith, R. Stote, J. Straub, M. Watanabe, J. Wiórkiewicz-Kuczera, D. Yin, and M. Karplus. All-atom empirical potential for molecular modeling and dynamics studies of proteins. *The Journal of Physical Chemistry B*, 102:3586–616, 1998.

[128] A. Soldera and N. Metatla. Study of the glass transition temperatures of stereoregular PMMAs using different force fields. *Internet Electronic Journal of Molecular Design*, 4:721–736, 2005.

[129] I. Vorobyov, V. M. Anisimov, S. Greene, R. M. Venable, A. Moser, R. W. Pastor, and A. D. MacKerell. Additive and classical drude polarizable force fields for linear and cyclic ethers. *Journal of Chemical Theory and Computation*, 3:1120–1133, 2007.

[130] D. A. Case, T. E. Cheatham, T. Darden, H. Gohlke, R. Luo, K. M. Merz Jr., A. Onufriev, C. Simmerling, B. Wang, and R. J. Woods. The Amber biomolecular simulation programs. *Journal of Computational Chemistry*, 26(16):1668–1688, 2005.

[131] J. C. Phillips, R. Braun, W. E. I. Wang, J. Gumbart, E. Tajkhorshid, E. Villa, C. Chipot, R. D. Skeel, K. Schulten, and L. Kale. Scalable molecular

dynamics with NAMD. *Journal of Computational Chemistry*, 26(16):1781–1802, 2005.

[132] F. Koch, M. Kullmann, U. Selig, P. Nuernberger, D. C. G. Götz, G. Bringmann, and T. Brixner. Coherent two-dimensional electronic spectroscopy in the Soret band of a chiral porphyrin dimer. *New Journal of Physics*, 15(025006):1–12, 2013.

[133] D. Abramavicius, V. Butkus, J. Bujokas, and L. Valkunas. Manipulation of two-dimensional spectra of excitonically coupled molecules by narrow-bandwidth laser pulses. *Chemical Physics*, 372(1-3):22–32, 2010.

[134] V. Perlík, J. Hauer, and F. Sanda. Finite pulse effects in single and double quantum spectroscopies. *Journal of the Optical Society of America B*, 34(2):430–439, 2017.

[135] K. L. Dillman, K. R. Shelly, and W. F. Beck. Vibrational coherence in polar solutions of ZnII tetrakis(N-methylpyridyl)porphyrin with soret-band excitation: Rapidly damped intermolecular modes with clustered solvent molecules and slowly damped intramolecular modes from the porphyrin macrocycle. *The Journal of Physical Chemistry B*, 113:6127–6139, 2009.

[136] F. D. Fuller, D. E. Wilcox, and J. P. Ogilvie. Pulse shaping based two-dimensional electronic spectroscopy in a background free geometry. *Optics Express*, 22:1018–1027, 2014.